

## ABSTRACT

Title of dissertation:      MICROWAVE STUDY OF THE PROPERTIES OF  
UNCONVENTIONAL SUPERCONDUCTING SYSTEMS

Seokjin Bae  
Doctor of Philosophy, 2020

Dissertation directed by: Professor Steven M. Anlage  
Department of Physics

Microwave techniques have been widely used to characterize properties of conventional superconducting systems. Examples include characterizing the magnetic penetration depth of bulk crystals and thin films, residual resistance of superconducting radio-frequency cavity systems for use in particle accelerators, and resonance properties of superconducting microwave electronic circuit components such as coplanar waveguides and Josephson junction devices.

In recent decades, new types of superconducting systems have appeared and massive characterization efforts have been made through low frequency techniques such as transport resistivity measurement, quantum oscillations in electrical resistance and magnetic susceptibility, scanning tunneling microscopy, optical frequency techniques, X-ray, angle-resolved photoemission spectroscopy, and Raman spectroscopy. On the other hand, microwave characterization of these new systems has been less frequent. As the diversity of an ecosystem helps the system to be more robust, the diversity of scientific measurements provides a more thorough understanding of a physical

system because of the complimentary advantages of each measurement. The advantages of the microwave technique are first, it is non-destructive since the measurement does not require galvanic contact between the probe and the sample. Second, it has a good signal-to-noise ratio because it employs sensitive high frequency instruments and techniques. Third, the microwaves only marginally perturb the system under investigation since the photon energy of the probing signal is typically much lower than the maximum superconducting energy gap, which is not the case for optical techniques.

In this thesis, unconventional superconducting systems, such as superconductors with non-*s*-wave pairing symmetry and superconductors with non-trivial topology, are investigated by means of microwave techniques. The thesis consists of two parts. In Part 1, I will discuss a newly developed microwave superconducting gap spectroscopy system. Using a combination of resonant microwave transmission technique and laser scanning microscopy, I demonstrated that the new technique can directly image the pairing symmetry of superconductors with unconventional pairing symmetries. During the demonstration with an example *d*-wave superconductor, a signature of Andreev bound states was also found. A phenomenological model to explain the observed properties of the Andreev bound states is also discussed. Lastly, an effort to broaden the adaptability of the new technique to samples of more general morphology is discussed.

In Part 2, I describe a microwave surface impedance technique and its application to the characterization of topological superconducting systems. A thickness dependent surface reactance study of an artificial topological superconductor  $\text{SmB}_6/\text{YB}_6$  (topological insulator / superconductor bilayer) was used to determine the character-

istic lengths of the system (normal coherence length, penetration depth, and thickness of the topological surface state), and revealed robust bulk insulating properties of  $\text{SmB}_6$  thin films. A surface resistance and reactance study on the candidate intrinsic topological superconductor  $\text{UTe}_2$  revealed the existence of residual normal fluid and a chiral spin-triplet pairing state, which together point out the possible existence of an itinerant Majorana normal fluid on the surface of chiral superconductors.

MICROWAVE STUDY OF THE PROPERTIES OF UNCONVENTIONAL  
SUPERCONDUCTING SYSTEMS

by

Seokjin Bae

Dissertation submitted to the Faculty of the Graduate School of the  
University of Maryland, College Park in partial fulfillment  
of the requirements for the degree of  
Doctor of Philosophy  
2020

Advisory Committee:

Professor Steven M. Anlage, Chair/Advisor

Professor Frederick C. Wellstood

Professor Ichiro Takeuchi

Professor Nicholas P. Butch

Professor Johnpierre Paglione

© Copyright by  
Seokjin Bae  
2020

## Acknowledgments

When I started my Ph. D. program, I had an experiment-phobia. Back in my undergrad experimental courses, occasionally some measurement devices went out of order when I operated them. Despite this, Dr. Anlage accepted me as his student even though I had no background in experimental physics. He has guided me on how to study physics experimentally, and patiently waited for me to develop skills. I still remember the time I broke a vacuum pump in my first month in the lab. He encouraged me, saying "Mistakes happen in experiments, but it is fine as long as you learn a lesson from it and make progress". He has always been respectful to his students and their opinions and treated us as his colleagues. He always tried his best to help us to solve the research problem together by sacrificing his time. If it had not been for his unconditional support and guidance, I would not pass through the many hurdles in getting a Ph. D.. It was my honor and pleasure to work with him.

I would also like to appreciate other committee members: Dr. Takeuchi, Dr. Paglione, Dr. Butch, and Dr. Wellstood. As I worked together with them in various projects, Their guidance not only broadened my sight on condensed matter physics, but also helped to improve my research skills. I truly learned a lot especially on how to put my research in a greater context, how to display figures to efficiently deliver my claim, and how to check rigor of a claim in a step-by-step manner. Even though he is not in the committee, I would like to also thank Dr. Ciovati for his help on annealing our niobium top plate of the disk dielectric resonator. His help enabled us to obtain a very high quality factor resonator.

I would also like to thank post-docs and research scientists: Seunghun, Hyunsoo, Yun-Sok, and Alexander for their invaluable help. When I first met Seunghun, I was in a sort of slump and depression. Seunghun provided me not only top-quality samples but also shared his precious know-how on research while sacrificing his time. His insight and passion motivated me, and discussion with him helped me to re-realize the fact that "Physics is Phun!". Finally, I could get out of my a year-long depression. Hyunsoo was a master of ultra-low temperature experiment. He helped and taught me to avoid numerous pitfalls in realizing a sub 100 mK measurement system. Yunsook was the person I could trust the most when it comes to the topological systems. He always tried to express the abstract concept of topology in an experimentalist language, which helped me to understand the concept more intuitively. Alexander is a hard-core optics expert. He provided me tons of useful advice when I and Yüewen built a Laser scanning microscope system for the dilution fridge.

I would like to thank my labmates: Yüewen, Bakhrom, Shukai, Jingnan, Lei, Tamin, Bo, and Min. We helped each other out in solving research obstacles and supported each other emotionally. I cannot forget the conversations we had when we assembled the heavy vacuum cans of the dilution fridge. I would also like to thank my friends who I met at UMD for supporting each other during hard times.

Finally, I would like to thank my family for their unconditional love and support. I feel sorry for them as I stay abroad for my study and not taking care of them enough. However, they have always supported my dream and loved me unconditionally. The word "Thank you" cannot express my gratitude enough.

---

# Table of Contents

---

<b>Table of Contents</b>	<b>4</b>
<b>List of Tables</b>	<b>7</b>
<b>List of Figures</b>	<b>8</b>
<b>List of Abbreviations</b>	<b>12</b>
<b>Chapter 1 Introduction</b>	<b>1</b>
1.1 Superconductivity . . . . .	1
1.2 Unconventional superconductivity . . . . .	2
1.2.1 Superconductivity with various pairing states . . . . .	2
1.3 Topological superconductivity . . . . .	4
1.3.1 Gapped topological systems . . . . .	4
1.3.2 Intrinsic topological superconductor . . . . .	7
1.3.3 Artificial topological superconductor . . . . .	8
1.4 Microwave study of superconducting systems: past, present, and outlook	9
<b>Chapter 2 Laser Scanning Microscopy Photoresponse Measurement</b>	<b>12</b>
2.1 Working principle . . . . .	12
2.2 Measurement setup . . . . .	17
2.2.1 Microwave devices setup, signal flow, and acquisition of PR . .	17
2.2.2 Cryogenics . . . . .	19
2.2.3 4f laser scanning system . . . . .	20
<b>Chapter 3 Gap Nodal Spectroscopy through Anisotropic Nonlinear Meissner Effect - Bulk response</b>	<b>23</b>
3.1 Gap spectroscopy: survey . . . . .	24
3.2 Anisotropic nonlinear Meissner effect . . . . .	26
3.3 First demonstration of LSM-PR as a Gap spectroscope: spiral resonator	31
<b>Chapter 4 Gap Nodal Spectroscopy through Anisotropic Nonlinear Meissner Effect - Surface response</b>	<b>34</b>
4.1 Rotation of the PR pattern - new PR origin . . . . .	34
4.2 Paramagnetic Meissner effect from surface Andreev Bound states . . .	37
4.2.1 Formation of surface Andreev bound states . . . . .	37
4.2.2 Energy level splitting of ABS due to the Doppler shift . . . . .	40
4.2.3 Consequence of the energy level splitting: paramagnetic Meissner effect . . . . .	41

4.3	Theoretical model for Andreev bound State PR . . . . .	43
4.3.1	Calculation of the surface and bulk current density . . . . .	45
4.3.2	PR estimation model . . . . .	50
4.3.3	Comparison of the model calculation and experimental data . . . . .	55
<b>Chapter 5 Gap Nodal Spectroscopy through Anisotropic Nonlinear Meissner Effect - Improvement</b>		<b>59</b>
5.1	An issue with the spiral resonator . . . . .	59
5.2	Second generation resonator: Dielectric resonator . . . . .	60
5.2.1	Resonator design and simulation . . . . .	60
5.2.2	Estimation of systematic uncertainty in anisotropy of PR due to the effect of the resonator geometry . . . . .	65
5.3	Experimental results with dielectric resonator . . . . .	67
5.3.1	LSM-PR from a conventional $s$ -wave superconductor . . . . .	67
5.3.2	LSM-PR from a $d_{x^2-y^2}$ -wave superconductor . . . . .	71
5.3.3	Future direction: LSM-PR with DR on single crystal samples . . . . .	74
<b>Chapter 6 Microwave Impedance Spectroscopy</b>		<b>79</b>
6.1	Microwave complex conductivity . . . . .	79
6.1.1	Drude model of conductivity . . . . .	80
6.1.2	Two fluid model . . . . .	82
6.1.3	Connection between complex conductivity and surface impedance . . . . .	85
6.2	Microwave surface impedance measurement . . . . .	87
6.2.1	Transmission measurement setup and procedure . . . . .	87
6.2.2	Determination of resonance properties $f_0$ and $Q$ . . . . .	91
6.2.3	Converting resonance properties ( $f_0$ and $Q$ ) into surface impedance ( $Z_s$ ) . . . . .	95
6.2.4	Nonlocal limit . . . . .	96
6.3	Types of resonators . . . . .	97
6.3.1	Disk Dielectric resonator . . . . .	97
6.3.2	Hollow rutile cylindrical dielectric resonator . . . . .	101
6.3.3	Upgrade on the hollow cylindrical dielectric resonator . . . . .	106
<b>Chapter 7 Microwave Meissner Screening study of an Artificial Topological Superconductor - <math>\text{SmB}_6/\text{YB}_6</math></b>		<b>113</b>
7.1	Motivation for a microwave study of TI/SC systems . . . . .	114
7.2	Experiment . . . . .	117
7.2.1	Sample preparation . . . . .	117
7.2.2	Effective penetration depth measurement . . . . .	118
7.3	Model . . . . .	121
7.3.1	Meissner screening model of the bilayer system . . . . .	121
7.3.2	Spatial and temperature dependence of the Meissner screening . . . . .	124
7.4	Results . . . . .	126
7.4.1	$\text{YB}_6$ Single layer . . . . .	126
7.4.2	$\text{SmB}_6/\text{YB}_6$ bilayer . . . . .	127

7.4.3	Validity of the extracted characteristic lengths of the SmB <sub>6</sub> /YB <sub>6</sub> bilayers . . . . .	129
7.5	Implication of the results . . . . .	130
7.5.1	Robust bulk insulation and thickness of the surface states . . . . .	130
7.5.2	Design parameters for a vortex Majorana device . . . . .	133
7.6	Summary . . . . .	135
<b>Chapter 8 Microwave Conductivity study of an Intrinsic Topological Superconductor - UTe<sub>2</sub></b>		<b>136</b>
8.1	Possibility of topological superconductivity in UTe <sub>2</sub> . . . . .	137
8.1.1	Types of intrinsic topological superconductors . . . . .	137
8.1.2	Possibility of Weyl superconductivity in UTe <sub>2</sub> . . . . .	138
8.2	Experiment . . . . .	141
8.2.1	UTe <sub>2</sub> sample growth and preparation . . . . .	141
8.2.2	Microwave impedance measurement in the disk DR . . . . .	142
8.3	Results . . . . .	144
8.3.1	Microwave surface impedance and complex conductivity . . . . .	144
8.3.2	Real part of $\tilde{\sigma}$ analysis . . . . .	146
8.3.3	Imaginary part $\tilde{\sigma}$ analysis . . . . .	147
8.4	Discussion of the origin of residual normal fluid . . . . .	153
8.4.1	Extrinsic origins . . . . .	153
8.4.2	Intrinsic origins . . . . .	154
8.5	Issues and future plans . . . . .	155
8.5.1	Quantitative estimation of the scattering life time . . . . .	155
8.5.2	Microwave impedance measurement in the first generation hollow DR . . . . .	156
8.6	Summary . . . . .	158
<b>Chapter 9 Conclusion</b>		<b>159</b>
<b>Chapter A Further details on the electromagnetic screening model</b>		<b>161</b>
A.1	Boundary conditions . . . . .	161
A.2	Field solutions . . . . .	162
<b>Bibliography</b>		<b>164</b>
<b>Curriculum vitae</b>		<b>192</b>

---

## List of Tables

---

Table 3.1	Summary of some advantages and disadvantages of several representative superconducting gap spectroscopy techniques (not an exhaustive list). . . . .	26
Table 7.1	Summary of the extracted characteristic lengths from the electrodynamic screening model for TI/SC bilayers for different SmB <sub>6</sub> layer thickness . . . . .	128
Table 7.2	Characteristic lengths ( $\xi_N$ and $t_{TSS}$ ) of the SmB <sub>6</sub> /YB <sub>6</sub> bilayers and derived property (Fermi velocity $v_F$ ) for SmB <sub>6</sub> obtained from the microwave Meissner screening study compared to those from previous studies . . . . .	130
Table 8.1	Low temperature theoretical asymptotes of the normalized superfluid density $\rho_s(T)$ for the various spin-triplet pairing states . . .	151

---

## List of Figures

---

Fig. 1.1	Schematic illustration of the gapless metallic boundary state of a topological insulator (TI). . . . .	6
Fig. 2.1	Principle of photoresponse generation . . . . .	15
Fig. 2.2	An example microwave transmission of a $\text{YBa}_2\text{Cu}_3\text{O}_{7-\delta}$ (YBCO) coplaner waveguide (CPW) resonator . . . . .	16
Fig. 2.3	Block diagram and procedure of LSM-PR measurement . . . . .	18
Fig. 2.4	Schematic view of optical path of the laser beam in the 4f scanning system . . . . .	20
Fig. 3.1	The relation between pairing symmetry of the Cooper pair wavefunction and gap structure in momentum space for the $s$ -wave, $p_x$ -wave, and $d_{x^2-y^2}$ -wave superconductor. . . . .	24
Fig. 3.2	Temperature dependence of the nonlinear Meissner coefficient $b_\Theta(T)$ when the direction of the current is parallel to the gap nodal direction and anti-nodal direction for the case of $d_{x^2-y^2}$ -wave superconductor, $p_y$ -wave superconductor, isotropic $s$ -wave superconductor, and anisotropic $s$ -wave superconductor. . . . .	29
Fig. 3.3	Schematic view of a circulating current induced by a perpendicular magnetic field $B$ . . . . .	30
Fig. 3.4	Schematic view of a spiral resonator, transmission measurement setup for the spiral resonator, and an example frequency profile of the transmission through a niobium spiral resonator. . . . .	32
Fig. 3.5	PR images from a YBCO spiral on LAO substrate at 81.9 K and 4.4 K. . . . .	33
Fig. 4.1	PR image from the YBCO/LAO spiral at 4.4 K and 3.9 K. . . . .	36
Fig. 4.2	Schematic illustration of the Andreev reflection (AR) at the interface between normal and superconducting region, illustration of (110) physical boundary of a $d_{x^2-y^2}$ -wave superconductor and an order parameter suppressed normal region (N), and an expected density of states for a $d_{x^2-y^2}$ superconductor with (110) boundaries. . . . .	38
Fig. 4.3	Illustration of the energy level splitting between quasiparticles moving in the same direction and the opposite direction to the screening superfluid motion under the external magnetic field. . . . .	41

Fig. 4.4	Surface density of states split into counter-moving states and co-moving states due to the Doppler shift in the presence of a supercurrent flow, and temperature dependence of the penetration depth of YBCO thin films with different angles between the boundary direction and a-axis of the lattice. . . . .	43
Fig. 4.5	Crystal structure of YBCO and top view of the twin boundary of YBCO . . . . .	44
Fig. 4.6	Diagram showing the geometry setup of the sample system. . . .	47
Fig. 4.7	Anisotropy ratio in the bulk Meissner current density . . . . .	48
Fig. 4.8	Temperature dependence of the current densities at the surface and the bulk when $v_s \parallel$ gap node ( $\chi = \pi/4$ ) and superfluid momentum $q = p_F v_s / \Delta_0 = 0.1$ . . . . .	50
Fig. 4.9	The calculated temperature dependence of the Antinodal and nodal PR (magnitude) from the model calculation . . . . .	54
Fig. 4.10	Input microwave power ( $P_{RF}$ ) and angular ( $\chi$ ) dependence of total (surface+bulk) PR. . . . .	56
Fig. 5.1	Optical microscope image of a spiral sample made from a $Ba_{1-x}K_xFe_2As_2$ thin films, the PR image taken from the $Ba_{1-x}K_xFe_2As_2$ spiral, optical microscope image from the PCCO spiral, and PR image from the PCCO spiral. . . . .	61
Fig. 5.2	Schematic cross-section diagram of the dielectric resonator setup with a sample . . . . .	62
Fig. 5.3	Numerical simulation (HFSS) setup geometry of the DR, microwave magnetic field density plot inside the dielectric disk, and surface current density plot on the sample. . . . .	64
Fig. 5.4	HFSS simulated setup asymmetries to test the robustness of the uniformity of the angular dependence of the current density. . .	67
Fig. 5.5	A PR image taken with a sapphire dielectric disk placed on a Nb thin film sample and corresponding reflectivity image. . . . .	68
Fig. 5.6	PR image from a 40 nm thick unpatterned YBCO thin film. . . . .	72
Fig. 5.7	Photo and PR image of rutile disk (3 mm diameter) and the $CeCoIn_5$ crystal. Photo and PR image of $KFe_2As_2$ crystal. . . . .	76
Fig. 5.8	The proposed waveguide setup for examining pairing symmetry of single crystal samples with LSM-PR. . . . .	78
Fig. 6.1	Schematic view of the signal path of the microwave transmission measurement . . . . .	89
Fig. 6.2	Typical $S_{21}$ measurement near a resonance peak and temperature dependence of the resonant frequency $f_0(T)$ . . . . .	90
Fig. 6.3	Example plot of $ S_{21}(f) $ data in linear scale (black) near the peak and corresponding fit curves (yellow) . . . . .	92
Fig. 6.4	Calculated surface current density on the bottom surface of the rutile disk DR (top surface of the sample) normalized by its maximum value . . . . .	100

Fig. 6.5	Cross section view of the first generation hollow DR design . . .	104
Fig. 6.6	Resonant frequency $f_0(T)$ study of the first generation hollow DR without a sample . . . . .	106
Fig. 6.7	HFSS simulation design of the second generation of the hollow DR	107
Fig. 6.8	Integrated surface magnetic field over the surface of each component of the resonator in terms of the height and radius of the cavity . . . . .	109
Fig. 6.9	The second generation, large-cavity hollow DR design with hot finger technique . . . . .	111
Fig. 7.1	Comparison table of DC, microwave, and THz techniques as characterization tools for the TI/SC system . . . . .	116
Fig. 7.2	A schematic of the bilayer consisting of an $\text{SmB}_6$ film and a $\text{YB}_6$ film. Temperature dependence of the effective penetration depth of the $\text{SmB}_6/\text{YB}_6$ bilayers for various $\text{SmB}_6$ layer thickness, and that of $\text{Cu}/\text{Nb}$ (conventional metal / superconductor) bilayers for various $\text{Cu}$ layer thickness. . . . .	119
Fig. 7.3	Schematic spatial profile of the order parameter and the local penetration depth through the normal layer (N) / superconductor (S) bilayer sample for the case of the absence/presence of an insulating bulk. . . . .	123
Fig. 7.4	$\Delta\lambda_{eff}(T)$ vs. $T/T_c$ data and fits for $\text{SmB}_6/\text{YB}_6$ bilayers at low temperature, $T/T_c < 0.3$ . . . . .	128
Fig. 7.5	Schematic view of the proposed position dependence of the surface states wavefunction and induced order parameter in the $\text{SmB}_6/\text{YB}_6$ bilayer . . . . .	131
Fig. 7.6	Illustrations of the surface state wavefunctions in a TI/SC bilayer and band structure near the Dirac point for each limit is plotted from the ARPES measurement on $\text{Bi}_2\text{Se}_3/\text{NbSe}_2$ , a representative TI/SC bilayer for various limits of the TI layer thickness . . . . .	134
Fig. 8.1	Bulk and surface Brillouin zone of a Weyl superconductor . . . .	138
Fig. 8.2	Polar Kerr rotation and Specific heat measurement on $\text{UTe}_2$ . . .	140
Fig. 8.3	Photo and input microwave power $P_{in}$ dependence of the resonant frequency $f_0(T)$ of a $\text{UTe}_2$ crystal measured in a disk DR . .	143
Fig. 8.4	The measured temperature dependence of the surface impedance $Z_s$ of a $\text{UTe}_2$ sample, and comparison to that of topologically trivial superconductors . . . . .	145
Fig. 8.5	Complex conductivity of a $\text{UTe}_2$ sample and comparison to that of topologically trivial superconductors . . . . .	147
Fig. 8.6	Effective penetration depth of $\text{UTe}_2$ sample . . . . .	148
Fig. 8.7	Low temperature behavior of the normalized superfluid density $\rho_s(T)$ in $\text{UTe}_2$ with best fits for various triplet pairing states . . .	152
Fig. 8.8	Examination of possible extrinsic origins of residual normal fluid	154

Fig. 8.9 Measured surface impedance from  $UTe_2$  sample in the first generation hollow DR . . . . . 157

## List of Abbreviations

ABS	Andreev bound state
AR	Andreev reflection
AC	Alternating current
aNLME	Anisotropic nonlinear Meissner effect
ARPES	Angle-resolved photoemission spectroscopy
ARSH	Angle-resolved specific heat measurement
BCS	Bardeen-Cooper-Schrieffer
BdG	Bogoliubov-de-Gennes
BSCCO	$\text{Bi}_2\text{Sr}_2\text{CaCu}_2\text{O}_{8+\delta}$
CDW	Charge density wave
CPW	Coplaner waveguide
CP	Cold plate
dBm	Power ratio in decibels (dB) of the measured power
DC	Direct current
DOS	Density of states
DR	Dielectric resonator
GHz	Gigahertz, $10^9$ Hz
HFSS	High frequency structure simulator
ITL	Infinity corrected tube lens
LAO	$\text{LaAlO}_3$
LSM	Laser scanning microscope
LSM-PR	Laser scanning microscope photoresponse
MZM	Majorana zero mode
MXC	Mixing chamber plate
NLME	Nonlinear Meissner effect
NMR	Nuclear magnetic resonance
PEC	perfect electric conductor
PME	Paramagnetic Meissner effect
PR	Photoresponse
SC	Superconductor
SEM	Scanning electron microscopy
SQUID	Superconducting quantum interference device
STM	Scanning tunneling microscopy
TDO	Tunnel diode oscillator
TI	Topological insulator
TRS	Time-reversal symmetry
TSC	Topological superconductor
TSS	Topological surface state
VNA	Vector network analyzer
YBCO	$\text{YBa}_2\text{Cu}_3\text{O}_{7-x}$
ZBCP	Zero bias conductance peak

# CHAPTER 1

---

## Introduction

---

### 1.1 Superconductivity

Superconductivity is a phenomenon in which the electrical resistivity of a material goes to zero upon cooling down below a critical temperature  $T_c$ . A superconductor (SC) can be distinguished from a perfect electrical conductor through the Meissner effect, which is the spontaneous exclusion of a static magnetic field. The superconducting transition is a second order phase transition, and an energy gap develops in the electron excitation spectrum below  $T_c$ . Superconductivity was first found in mercury (Hg) in 1911, and was soon followed by the discovery of many other superconductors. At that moment, most of the superconductors that were found were metallic elements such as niobium and aluminum, and their  $T_c$  was below 30 K.

The first microscopic theory that actually explained superconductivity was constructed by Bardeen, Cooper, and Schrieffer (BCS) in 1957 [1]. The BCS theory showed that two electrons can form a bound pair (Cooper pair) and exhibit zero electrical resistivity, the Meissner effect, and a jump in specific heat at  $T_c$  when an

attractive potential between the electrons is introduced. For the metallic elemental superconductors, the electron-phonon interaction was identified as the source of the attractive potential. These weak electron-phonon coupling mediated superconductors have an isotropic,  $s$ -wave pairing state wavefunction with no orbital angular momentum. Hence, their superconducting energy gap  $\Delta$  in momentum space is also isotropic, and this type of superconductor is often denoted as a conventional superconductor. Also note that conventional superconductors are non-magnetic and vulnerable to the presence of magnetic impurities.

## 1.2 Unconventional superconductivity

### 1.2.1 Superconductivity with various pairing states

Later in the 1970s and 80s, new classes of superconductors were found. One class is the heavy Fermion superconductors [2, 3] whose Cooper pairs involve  $d$  and  $f$  orbital electrons with large effective mass. The other class is the copper oxide superconductors (Cuprates) with high transition temperature above 80 K [4, 5]. Unlike conventional superconductors, both of these new superconductors cannot be explained by the electron-phonon interaction. In fact, their actual superconducting pairing mechanism is still under debate. Also, these new classes of superconductors were found to coexist with magnetic order [6] and exhibit strong Coulomb interaction from the localized  $d$  and  $f$  orbital electrons.

A more striking difference arises in the pairing state. Many of the Cuprates and heavy Fermion superconductors possess  $p$ - or  $d$ -wave pairing state with non-zero orbital angular momentum and, whose gap function is highly anisotropic. For example, several types of measurement concluded that  $\text{YBa}_2\text{Cu}_3\text{O}_{7-\delta}$  (YBCO) and  $\text{Bi}_2\text{Sr}_2\text{CaCu}_2\text{O}_{8+\delta}$  (BSCCO), representative Cuprates, have a  $d_{x^2-y^2}$ -wave pairing state, which yields a 4-fold symmetric gap structure with 4 line nodes [7–9]. For the case of heavy Fermion superconductors, evidence shows that  $\text{CeCoIn}_5$  has a  $d_{x^2-y^2}$ -wave pairing state [10, 11], and  $\text{UGe}_3$  has a  $p$ -wave pairing state which yields a 2-fold symmetric gap with two point nodes [12].

The various pairing states and their gap nodal structures are of importance in understanding the properties of a material. The various pairing states result in distinguishable behaviors of penetration depth, thermal conductivity, specific heat, and spin relaxation rate of nuclear magnetic resonance (NMR) with respect to temperature and magnetic field [13–15]. Therefore, these newly emerging superconductors with exotic pairing states require them to be classified as a separate category; "Unconventional superconductors". Until now, when a new type of superconductor is discovered, the first property to be investigated is the pairing state in order to understand the pairing mechanism and various material properties. In Chap. 3, we will introduce our effort to develop new types of pairing state spectroscopy utilizing a microwave measurement technique.<sup>1</sup>

---

<sup>1</sup>For the readers who are not familiar with finite frequency techniques, the frequency range of the microwave signal is 0.3 ~ 300 GHz (photon energy in the  $\mu\text{eV}$  range), and that of THz signals is 0.1 ~ 10 THz (photon energy in the meV range). Above the THz range is the optical range (infrared, visible light, ultraviolet, etc.).

## 1.3 Topological superconductivity

The concept of non-trivial band topology in the bulk of a solid, and its corresponding boundary states, have brought completely new insights into our ways of understanding condensed matter systems. The field of superconductivity has not been an exception. In this section, I will first introduce gapped topological systems in general. Then, several types of superconducting systems with non-trivial topology will be introduced, and these are subjects of this thesis (Chap. 7 and 8).

### 1.3.1 Gapped topological systems

Topology is one way to "categorize" a physical system.<sup>2</sup> If a Hamiltonian (or wavefunction equivalently) of one system cannot be connected to that of the other system by adiabatic deformation without changing a globally defined quantity, those two systems are considered as "topologically distinct", and that globally defined quantity is called "topological invariant" [16, 17]. Examples of non-adiabatic deformations are band inversion or change in symmetry of the Hamiltonian (or wavefunction). Examples of topological invariants are the Chern number of a 2D Quantum Hall system or  $Z_2$  invariant of a 3D topological insulator [16].

Naturally, gapped systems are good candidates to possess non-trivial topology. For example, if a gapped Hamiltonian has a certain set of symmetries which are not

---

<sup>2</sup>Actually, every physical system is topological. Systems are either topologically "trivial" or "non-trivial". But for the convenience, one refers to topologically non-trivial systems as "topological systems".

present in the atomic limit (i.e., vacuum)<sup>3</sup>, the gap hinders the Hamiltonian of the system from being adiabatically connected to the topologically trivial Hamiltonian of the atomic limit. The non-trivial topology in this case is protected by the gap and is therefore robust. The types of symmetries of the bulk gap and corresponding topological invariants are well summarized by the seminal work of Schnyder et al [18]. The same story is true for gapped systems with band inversion.

One of the most interesting features of the gapped topological systems is its gapless boundary state. The existence of a boundary state is required by nothing but the continuity condition of the wavefunctions. Imagine a vacuum which can be considered as atoms that are infinitely far from each other. There should be only atomic orbital energy levels in the vacuum. Now, if we bring atoms together to form a solid, these atomic orbitals start to hybridize and form energy bands. At the same time, various other interactions between atoms can be involved. Some of the interactions, for example spin-orbit coupling, may invert the energy order of the bands from different atomic orbital origins (See Fig. 1.1). Now, imagine an electron which is trying to move out from that solid. The Hamiltonian which dictates the electron wavefunction starts from that of the gapped inverted bands to that of the gapped atomic levels without inversion. For the wavefunction of the electron to satisfy the continuity condition, the inverted band gap must be closed (un-twisted) at the boundary. This condition enforces the existence of gapless metallic boundary states of the gapped topological systems. Again, the same story is true for the symmetry imposed gapped system.

---

<sup>3</sup>One can consider moving from a solid to a vacuum as separating the close-packed atoms to the individual atoms that are infinitely far apart.

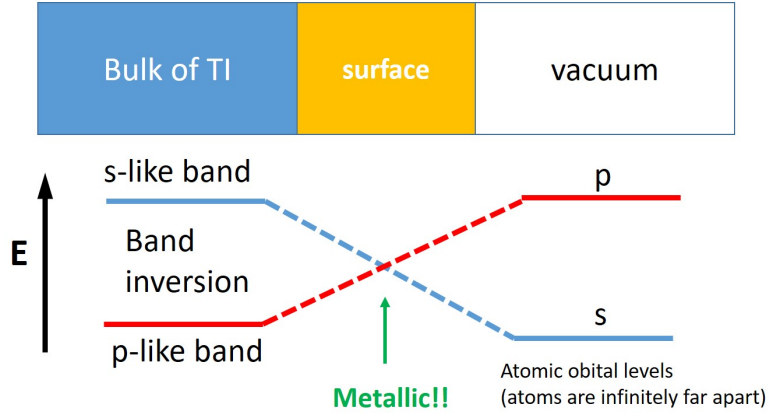


Fig. 1.1 Schematic illustration of the gapless metallic boundary state of a topological insulator (TI).

A representative example of the gapped system is an insulator. An insulator with non-trivial topological invariant (due to symmetries or band inversion) is denoted as a topological insulator (TI). Interestingly, the gapless boundary state of this system is predicted to have a linear dispersion with helical spin-momentum locking [19] (The direction of a spin is not free but determined by the direction of a momentum). These predicted exotic boundary states, which are denoted as topological surface states (TSS), have been a huge motivation for the condensed matter community to find realizations of TI. Bi-based compounds such as  $\text{Bi}_{1-x}\text{Sn}_x$ ,  $\text{Bi}_2\text{Te}_3$  and  $\text{Bi}_2\text{Se}_3$  were first confirmed as being TI with evidence of a bulk gap and gapless helical surface states [20–22]. Soon, the topological Kondo insulator  $\text{SmB}_6$  was added as an excellent example of this species [23, 24]. There may be numerous other examples but those shall be omitted to focus on the main points of this thesis.

### 1.3.2 Intrinsic topological superconductor

Superconductors are another excellent example of a gapped system. Although its normal state is not insulating, an energy gap opens below  $T_c$  in the electron excitation spectrum. The Hamiltonian which describes the gapped states of the superconductor is called the Bogoliubov-de-Gennes (BdG) Hamiltonian. If this BdG Hamiltonian has certain symmetries, it can also be topologically non-trivial. Again, Ref. [17, 18] serve as an excellent "brochure" for the symmetry conditions on the BdG Hamiltonian which can make the system topological. These types of superconductors are called topological superconductors (TSC) or intrinsic TSC, in contrast to an artificial TSC which will be introduced in Sec. 1.3.3. A TSC can also harbor gapless boundary states just as their insulating counterparts (TI) do. However, more excitement and interest has been given to the boundary states of TSC. Due to the particle-hole symmetry of the BdG Hamiltonian, the gapless zero-energy boundary state of a TSC is an excellent platform to realize Majorana zero modes. The Majorana zero mode (MZM) is a state whose Hermitian conjugate (anti-state) is itself, and has been proposed to be a building block for topological quantum computation. So far,  $\text{Sr}_2\text{RuO}_4$  has been proposed to be an intrinsic TSC, but this is still under debate [25]. Very recently, a newly found spin-triplet superconductor  $\text{UTe}_2$  is also proposed as a candidate intrinsic TSC [26, 27], and Chap. 8 will cover the evidence of intrinsic TSC in this material from my microwave measurements.

### 1.3.3 Artificial topological superconductor

Another way to realize topological superconductivity, and host MZMs, is by creating the proximity effect between the TSS of a TI and an adjacent  $s$ -wave superconductor in a TI/SC heterostructure. Theoretically predicted by L. Fu and C. Kane [28], the induced superconductivity in the TSS results in a Hamiltonian that is effectively equivalent to that of the 2D spinless chiral  $p$ -wave superconductor, which is an example of an intrinsic TSS [29]. In this superconducting system, one can produce a boundary to the topologically trivial normal state by creating a magnetic vortex, and an MZM is predicted to be hosted at the vortex core [28]. The proposed signatures of TSC and MZM have been experimentally verified by scanning tunneling microscopy (STM) measurements on  $\text{Bi}_2\text{Te}_3/\text{NbSe}_2$  thin film bilayers,  $\text{Cu}_x\text{Bi}_2\text{Se}_3$  and  $\text{FeTe}_{1-x}\text{Se}_x$  single crystals [30–32].<sup>4</sup>

---

<sup>4</sup> $\text{Cu}_x\text{Bi}_2\text{Se}_3$  and  $\text{FeTe}_{1-x}\text{Se}_x$  are not a TI/SC heterostructure so many of papers categorize them as an intrinsic TSC. However, rather than having non-trivial topological invariants in their superconducting state, their topological superconductivity is achieved by a different mechanism. In the normal state, their bulk has non-trivial topology and hence they possess TSS. Upon cooling and control of doping, the bulk enters a topologically trivial superconducting state. From the proximity effect, the superconductivity is "induced" in the topological surface state. This is the same mechanism used to create artificial TSCs. Therefore, here they are categorized as artificial TSCs.

## 1.4 Microwave study of superconducting systems: past, present, and outlook

Microwave studies have served as a useful tool in investigating the properties of superconducting systems. The probing signal in microwave techniques is in the GHz frequency range, giving only marginal perturbation to the system (microwave photon energy ( $\sim \mu\text{eV}$ )  $\ll$  typical SC gap size ( $\sim \text{meV}$ )). Also, it can investigate the temperature dependence of the properties of superconductors even after the DC transport resistance drops to zero below  $T_c$ .

The main usage of microwave techniques has been for measurement of the surface impedance  $Z_s$  of a superconducting system. For engineering purposes, the  $Z_s$  measurement of the superconducting circuit elements, such as coplanar waveguide, helps to characterize them for use as telecommunication devices (filters and detectors, etc.) [33]. For basic science research of superconductivity, it provides information on the low energy excitations from the temperature dependence of the penetration depth, from which one can obtain a hint for the pairing symmetry.

Usage of the microwave techniques for engineering purposes has boomed recently as most of the qubit designs (e.g., transmon) adopt microwave techniques on superconductors for qubit readout and manipulation. However, the use of microwave spectroscopy for science studies; characterizing unconventional superconductors, has dwindled. One reason for the dwindling use of microwave techniques is that there has been massive development in optical techniques such as angle-resolved photoe-

mission spectroscopy (ARPES) which directly measures electronic band structure [7]. Also there has been development in DC imaging techniques such as STM which directly measures the gap size and information on microscopic order such as charge density waves (CDW) [34]. As a result, these techniques have been popular among the unconventional superconductor research community. Another reason for the dwindling use is that most of the superconducting systems shows nearly zero residual surface resistance and hence, researchers in the unconventional superconductor community are only interested in measuring the reactance part of the surface impedance of unconventional superconductors. The surface reactance, from which the penetration depth is calculated, can be easily measured by the low frequency tunnel diode oscillator (TDO) technique [35]. Moreover, a TDO setup is cheaper to build compared to the setup for the microwave surface impedance measurement.

This competitive environment has narrowed down the role of microwave techniques in fundamental research on superconductivity, and only a few groups are left in the world. It is required for the microwave community either to make a technical invention which allows measurement of information related to microscopies and electronic structure, or to find information which complements that obtained by DC or optical techniques.

In this regard, Chap. 2 will introduce the working principle and measurement setup of a newly developed microwave technique which resolves the above disadvantages. The new technique, a Laser scanning microscopy photoresponse measurement, combines the microwave transmission measurement with the scanning laser thermal perturbation technique. This new technique allows one to image the superconducting

gap nodal structure of various pairing states in momentum space (Chap. 3, 4, 5), and to image microscopic defects and weak links in real space (Chap. 3).

On top of that, Chap. 6, 7, 8 will introduce a new usage of the microwave surface impedance measurement on topological superconducting systems. Optical techniques have the disadvantage of strongly perturbing the TSC due to its photon energy being larger than the typical gap size. DC techniques suffer from the disadvantage that the probing signal (DC current) cannot penetrate the insulating bulk to reach the proximitized TSS in the artificial TSC. The microwave surface impedance technique complements those disadvantages by utilizing low enough photon energy and employing a penetrating probing signal. For intrinsic TSCs, Chap. 8 will discuss how the surface resistance information, whose importance has not been recognized until now, helps to establish evidence of the surface Majorana normal fluid of the intrinsic TSC. For the artificial TSCs, Chap. 7 will discuss how the microwave measurement on the TI/SC thin-film bilayers accesses and reveals the properties of the proximitized TSSs which are buried by an insulating bulk that blocks access by DC techniques.

## CHAPTER 2

---

### Laser Scanning Microscopy Photoresponse

#### Measurement

---

- Recommended readings for this chapter: [36–38]

#### 2.1 Working principle

Laser scanning microscopy photoresponse (LSM-PR) measurement is a combination of a microwave transmission measurement and scanning laser microscopy. The microwave transmission monitors the global response of the sample of interest, and the scanning laser beam acts as a local perturbation. Through this combination, the LSM-PR technique has served as a micron-resolution, non-contact (and hence non-destructive), fast imaging tool for the local properties of superconducting microwave devices [36, 37]. Especially with its sensitivity to the local current density, the technique has been successfully utilized to image current distributions due to microscopic defects or weak links [38, 39] and grain boundaries [40].

The principle of how an LSM-PR measurement of a superconducting device works is as follows. First, a microwave resonator which involves a superconducting sample or device is prepared. The sample can be prepared either in a self-resonant structure (i.e., spiral or coplaner waveguide), or be placed adjacent to a resonance-facilitating structure such as a microwave cavity or dielectric disk. A microwave signal is injected to this resonant structure and transmission  $P = |S_{21}|^2$  is measured near a resonance. Here,  $|S_{21}|$  is a component of the scattering matrix which describes the voltage ratio  $V_2/V_1$  between the input  $V_1$  and output  $V_2$  port of the resonator.

Depending on the dimensions of the resonant structure, the microwave transmission shows resonant modes at certain frequencies. The frequency profile of the transmission around these resonances can be described by a Lorentzian curve, with a resonant frequency  $f_0$  and quality factor  $Q$  [41],

$$P(f) = P_{in}|S_{21}(f)|^2 = \frac{P_{in}}{(1 - f_0/f)^2 + (1/2Q)^2}, \quad (2.1)$$

where  $P_{in}$  is input microwave power to the resonator. The resonance properties  $f_0$  and  $Q$  are determined by the reactance  $X_s$  and resistance  $R_s$  of the resonator. The detailed relation between the resonance properties and surface impedance can be found in Sec. 6.2.3.

Now, while the resonator transmission is being measured, a scanning laser beam can be focused on a local point of the superconducting sample in the resonator. Qualitatively, this focused laser beam provides a local temperature increase  $\delta T(x, y)$ , which yields thermally excited quasi-particles and a decrease of local superfluid density  $n_s(x, y)$ .

This decrease  $\delta n_s(x, y)$  results in an increase in the local magnetic penetration depth  $\delta \lambda(x, y)$  and resistivity  $\delta \rho(x, y)$  of the sample.  $\delta \lambda(x, y)$  results in an increase in the surface reactance of the sample  $\delta X_s$ , and hence a decrease in the resonant frequency  $\delta f_0$ .  $\delta \rho(x, y)$  results in an increase in the surface resistance of the sample  $\delta R_s$ , and hence a decrease in the quality factor  $\delta Q$ . Note that  $\delta f_0$  and  $\delta Q$  are weighted by the amount of local current density  $\vec{j}$  flowing at the laser spot [36] ( $\delta f_0 \sim |\vec{j}|^2 \delta \lambda$ ,  $\delta(1/Q) \sim |\vec{j}|^2 \delta \rho$ ). This chain relation is visually summarized in Fig. 2.1(a). As a result, under laser illumination of the sample, the transmission resonance shifts to lower frequency and the bandwidth becomes larger (Fig. 2.1(b)). Then, at a certain fixed frequency, one can measure a change in the microwave transmission between when the laser is on and off. This quantity is what is called photoresponse (PR).

The contribution to PR from the shift in the resonant frequency  $f_0$  is denoted as the reactive (or also called inductive) PR ( $PR_X$ ) and the contribution to PR from the change in the quality factor  $Q$  is denoted as the resistive PR ( $PR_R$ ). Note that the shift of  $f_0$  gives a transmission change of the opposite sign between the left frequency  $f_L = f_0 - \Delta f$  and the right frequency  $f_R = f_0 + \Delta f$  as seen from Fig. 2.2. Therefore,  $PR_X$  is antisymmetric about  $f_0$ . In contrast, the change of  $Q$  (and hence broadening of the peak) gives a transmission change of the same sign between  $f_L$  and  $f_R$ . Thus,  $PR_R$  is symmetric with respect to  $f_0$ . This difference in the frequency dependence allows one to decompose the measured PR into  $PR_X$  and  $PR_R$  [42],

$$PR_X(f) = |PR(f_L) - PR(f_R)|/2 \quad (2.2)$$

$$PR_R(f) = |PR(f_L) + PR(f_R)|/2. \quad (2.3)$$

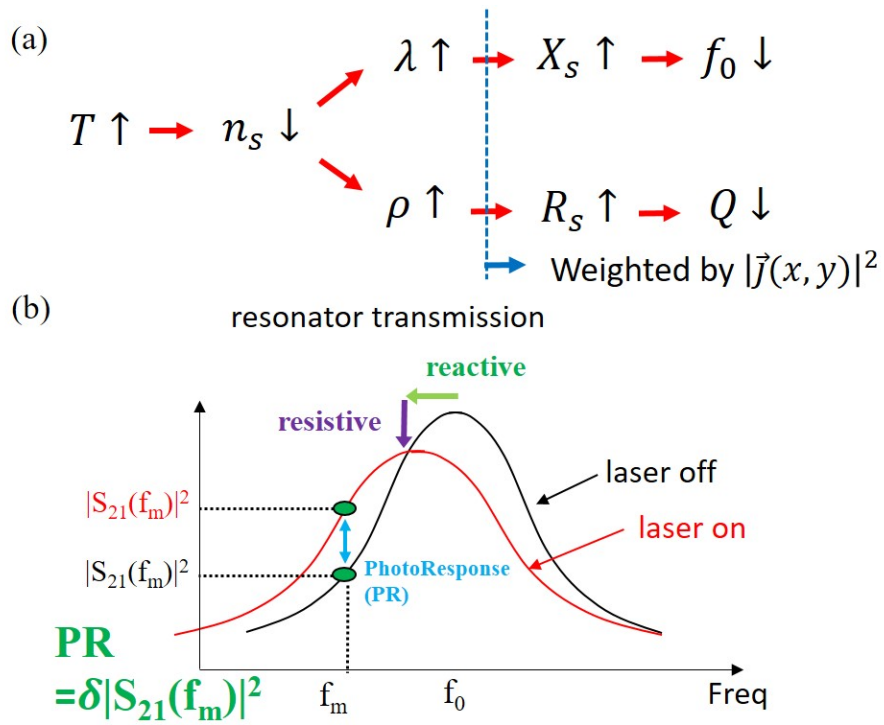


Fig. 2.1 (a) A schematic diagram which shows how a change in the local temperature  $T$  due to the laser illumination results in a change in the resonance properties  $f_0, Q$ . Note that changes in the  $X_s, R_s, f_0$ , and  $Q$  are weighted by the amount of local microwave current density  $|j(x, y)|^2$  at the laser spot. (b) Schematic microwave transmission in frequency domain  $|S_{21}(f)|^2$  around the resonance when the laser is on (red) and off (black). The increase in the local temperature  $\delta T$  decreases  $f_0$  which shifts the peak to the left, and decreases  $Q$  which broadens the peak bandwidth. Here,  $f_m$ , the optimal measurement frequency for PR, is chosen where PR shows its maximum as a function of frequency.

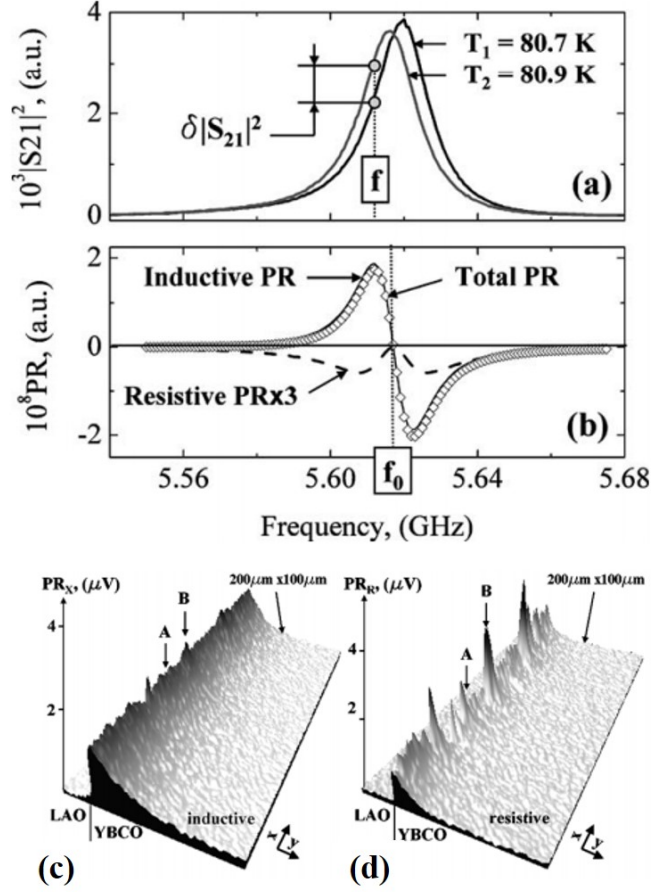


Fig. 2.2 (a) An example microwave transmission of a  $\text{YBa}_2\text{Cu}_3\text{O}_{7-\delta}$  (YBCO) coplaner waveguide (CPW) resonator on  $\text{LaAlO}_3$  (LAO) substrate at a temperature  $T_1 = 80.7$  K, and slightly higher temperature  $T_2 = 80.9$  K. (b) Decomposition of PR measured at  $T_1$  into reactive (inductive) and resistive components. Real space images of (c)  $PR_X(x, y)$  and (d)  $PR_R(x, y)$  along the patterned edge of a YBCO CPW, showing distinctly different spatial distributions. Reprinted figure with permission from Ref. [42].

The spatial maps of  $PR_X(x, y)$  and  $PR_R(x, y)$  provide an idea of the inductance and dissipation distribution along the sample (Fig. 2.2(c-d)).

To be more quantitative,  $PR_X$  and  $PR_R$  can be expressed in terms of  $\delta f_0$  and  $\delta Q$  as [36, 37],

$$PR_X(f, \mathbf{x}, \mathbf{y}) = P_{in} \frac{\partial |S_{21}|^2}{\partial f} \delta f_0 \propto -P_{in} \frac{\partial |S_{21}|^2}{\partial f} \delta f_0 \frac{\mu_0 \lambda^2 j_{RF}^2(\mathbf{x}, \mathbf{y})}{2W} g(\lambda) A \delta \lambda(\mathbf{x}, \mathbf{y}) \quad (2.4)$$

$$PR_R(f, \mathbf{x}, \mathbf{y}) = P_{in} \frac{\partial |S_{21}|^2}{\partial (1/2Q)} \delta (1/2Q) \propto -j_{RF}^2(\mathbf{x}, \mathbf{y}) \delta R_s(\mathbf{x}, \mathbf{y}). \quad (2.5)$$

Here,  $W$  is the sum of the field and kinetic stored energy of the resonator,  $j_{RF}(\mathbf{x}, \mathbf{y})$  is the local microwave current density induced on the sample,  $g(\lambda)$  is a prefactor determined by the resonator geometry, and  $A$  is the area heated by the laser. As one may notice, while other quantities are global,  $j_{RF}(\mathbf{x}, \mathbf{y})$ ,  $\delta \lambda(\mathbf{x}, \mathbf{y}) = \frac{\partial \lambda(\mathbf{x}, \mathbf{y})}{\partial T} \delta T$ , and  $\delta R_s(\mathbf{x}, \mathbf{y}) = \frac{\partial R_s(\mathbf{x}, \mathbf{y})}{\partial T} \delta T$  are local in nature. Therefore, investigating spatially resolved PR( $\mathbf{x}, \mathbf{y}$ ) images under various conditions can provide useful information on the microwave current, inductance, and resistance distributions of the superconducting structures under study. The detailed measurement setup to obtain PR images is described in the next section.

## 2.2 Measurement setup

### 2.2.1 Microwave devices setup, signal flow, and acquisition of PR

The flow of the microwave signals (blue line) in the LSM-PR measurement setup is shown in Fig.2.3. For the transmission measurement, a microwave signal from the signal generator is injected into a resonator containing a superconducting sample. Be-

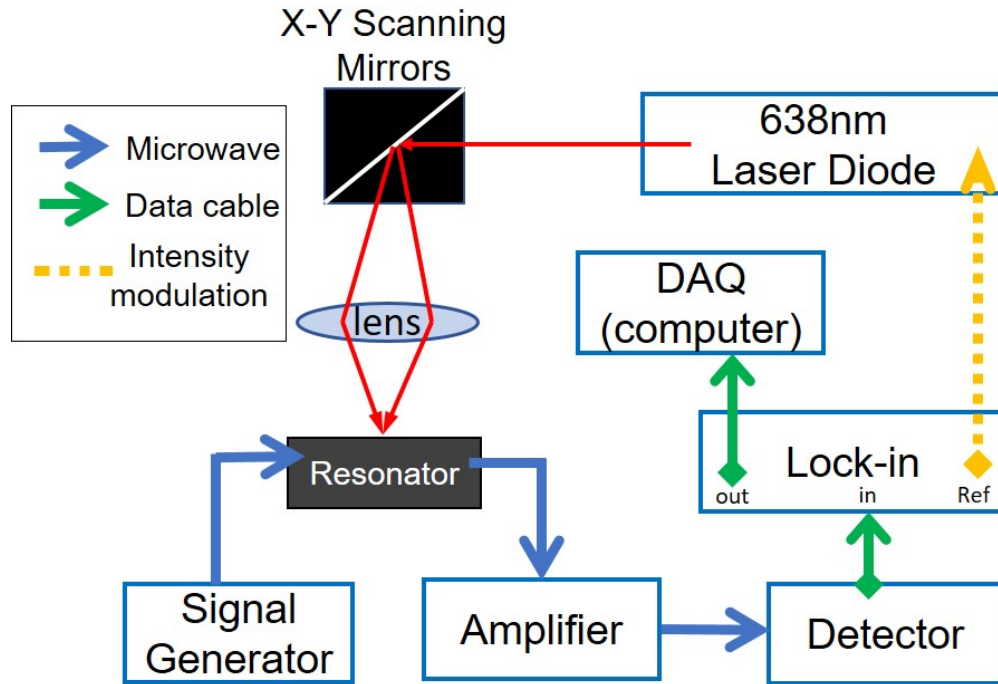


Fig. 2.3 (a) Block diagram and procedure of LSM-PR measurement. The path for each type of signal is described in the box inset.

low  $T_c$  and for specific resonant modes, a resonant screening current is induced on the surface of the sample and generates a response field. The transmitted microwave signal involves this response field. The transmitted signal then goes through an amplifier and arrives at a microwave detector which converts the amplitude (transmission) of the signal into a voltage signal (green line). This voltage signal is read by the lock-in amplifier and is sent to the data acquisition kit (NI-DAQ) that is connected to the recording computer.

While the above transmission measurement is going on, a focused scanning laser beam (red line) illuminates a small part of the sample and the laser intensity is modulated periodically in time by a modulation voltage wave input from the reference

output of the lock-in amplifier (yellow line). The illumination induces a local temperature modulation  $\delta T$  that is periodic in time.  $\delta T$  brings about a modulation in the microwave transmission as described in Fig. 2.1. This modulation is monitored by the lock-in amplifier and recorded as a PR signal. As noted above, the lock-in amplifier has an internal modulation source which modulates the laser intensity (Fig.2.3), so that the lock-in only accepts transmission modulation whose modulation frequency ( $f_{mod}$ ) agrees with lock-in's  $f_{mod}$ . This design helps to increase the signal-to-noise ratio of the measured PR signal. Once PR from the local position of the sample is acquired, the laser beam spot moves its position by changing the angle of the XY scanning mirrors and PR is measured from the new location. Once this scanning is done, one obtains a 2D image of PR(x,y).

For the reader's information, the devices used to construct the microwave and PR signal path are the Agilent E8257C signal generator, LNF-LNC6-20C cryogenic amplifier (mounted at 4 K stage), HP 8473C microwave detector, and SRS865 lock-in amplifier.

### 2.2.2 Cryogenics

The resonator and sample requires an ultra low temperature environment for the measurement of both low- $T_c$  and high- $T_c$  samples. Thus, the resonator is mounted on the mixing chamber of a BlueFors XLD-400 optical cryostat and its position is aligned with a cryostat window, as seen in Fig. 2.4. The temperature of the cold finger, where the resonator resides, ranges down to 40 mK with the window open before laser il-

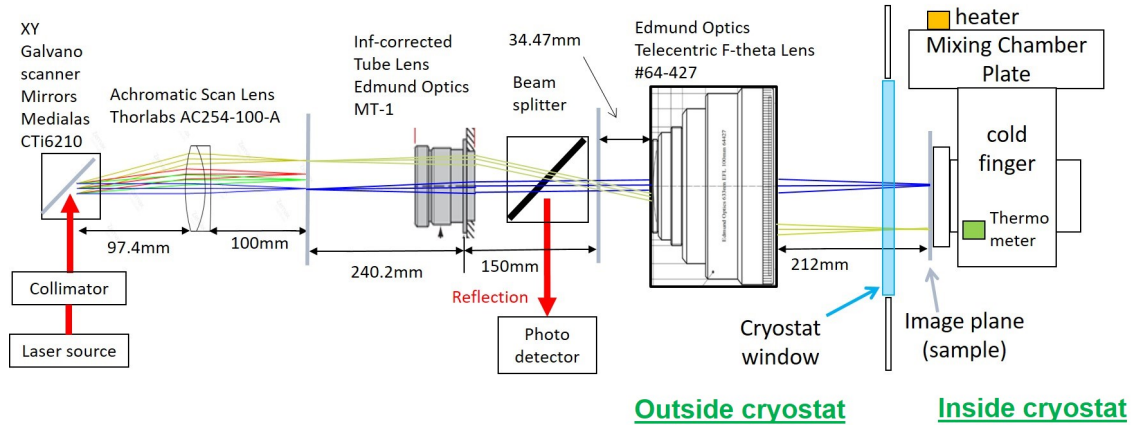


Fig. 2.4 Schematic view of optical path of the laser beam in the 4f scanning system. The grey vertical lines are focal planes. Drawing not to scale.

lumination. With  $\sim 0.2$  mW laser illumination, the temperature of the cold finger typically settles to 200 mK. The optical window of the cryostat facilitates scanned laser illumination for the spatially-resolved thermal perturbation of the sample while in the resonator.

### 2.2.3 4f laser scanning system

To obtain a 2D PR image from the current, inductance, and resistance distribution of the sample surface, a 4f laser scanning system is used. As depicted in Fig.2.4, the 638 nm laser beam from the laser source (Omicron LuxX+ 638) is collimated to a 2 mm diameter  $1/e^2$  Gaussian beam, and incident on two closely-spaced galvanometric mirrors (XY scanner). The deflection angle of the mirrors, which ranges through  $\pm 10^\circ$ , is controlled by voltage applied to their motors. The deflected scanning beam first passes through an achromatic scan lens, and then is directed into an infinity cor-

rected tube lens (ITL) (Edmunds Optics MT-1) with long focal length (200 mm) so that the transmitted beam is collimated again with almost two times smaller divergence. The collimated beam is then incident on the entrance pupil of the telecentric f-theta lens (Edmunds Optics 64-427). The telecentric f-theta lens directs the beams with different incident angle into orthogonally focused XY scanning beams with parallel translation paths in the image plane. The position of the spot (parallel translation of the beam) on the image plane is linearly proportional to the scan angle. This ensures the beams with different translated path share a flat (not curved) image plane, yielding a low distortion of the beam spot size. This ensures the beam intensity on the sample surface remains constant while scanning. The cryostat has optical windows for visible light which let the beams from the f-theta lens illuminate the sample. The working distance (212 mm) of the f-theta lens is long enough to have an image plane on the sample holder (or resonator) inside the cryostat.

After the beam applies a thermal perturbation to the sample to generate PR, the reflected beam pass through the telecentric f-theta lens which makes the beam follow the original incident path until it encounters a beam splitter (Edmund Optics #54-823) located in between the ITL and f-theta lens. The reflected beam is then guided to a photo-detector (Edmund Optics #53-373) which is connected to a second lock-in amplifier that is referenced to the light modulation. The obtained reflectivity image contains optical microscope information of the sample surface so that one can align the PR image to a real-space image of the sample. In addition, it can relate any artifacts in the PR image arising from optical interference patterns (such as Newton rings) or mechanical defects like a scratch on the sample surface. An example usage

of the reflective image is demonstrated in Fig. 5.5(a,b)

# CHAPTER 3

---

## Gap Nodal Spectroscopy through Anisotropic

## Nonlinear Meissner Effect - Bulk response

---

- This Chapter expands upon material previously published as Ref. [38].
- Recommended readings for this chapter: [14, 38, 43–47]

In this chapter, I will discuss how the LSM-PR technique can be utilized to image the gap nodal structure of unconventional superconductors via the anisotropic nonlinear Meissner effect (aNLME). The chapter will start by discussing the importance of the gap nodal structure and surveying existing gap spectroscopies. Then aNLME will be introduced and I will explain how PR measurements with the aNLME can image the gap nodal structure.

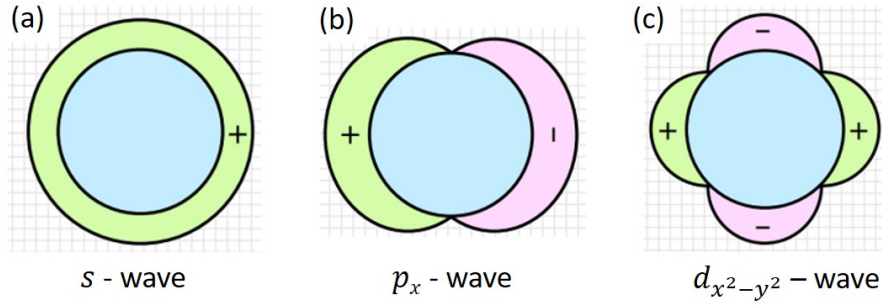


Fig. 3.1 The relation between pairing symmetry of the Cooper pair wavefunction and gap structure in momentum space for the (a)  $s$ -wave, (b)  $p_x$ -wave, and (c)  $d_{x^2-y^2}$ -wave superconductor.

### 3.1 Gap spectroscopy: survey

Among the several quantities that characterize superconductors, the superconducting gap function in momentum space is one of the most important parameters which governs the phenomenon. The symmetry of this gap function is directly related to the symmetry of the wavefunction of the superconducting electron pairs (Fig. 3.1) [48]. Many unconventional superconductors have nodes in their superconducting gap function  $\Delta(\vec{k})$  which are robust and arise from the symmetry of the pairing wavefunction. Thus, determining this gap nodal structure can give a significant clue about the pairing mechanism for the material.

Because of this importance, there have been numerous measurement methods developed to map out the gap structure on the Fermi surface [14]. For example, Raman scattering [8], angle-resolved photoemission spectroscopy (ARPES) [7], angle-resolved specific heat measurement (ARSH) [49–51], and superconducting quantum interference device (SQUID) interferometry [9] are commonly used. However, each

method has advantages and disadvantages (see Table 3.1) and it is best to use multiple methods to develop a consistent and complete picture of gap symmetry. ARPES and SQUID interferometry are sensitive to near-surface properties so they require very clean surfaces or high-quality tunnel barriers, respectively. Many materials present surfaces that are not characteristic of the bulk, or do not make high quality tunnel junctions, and this drawback limits them to study a relatively small number of materials. Meanwhile, ARSH and to some extent Raman scattering measure bulk response so they are free from the near-surface sensitive issue. However, they directly investigate quasiparticle response whose anisotropy is generally weaker than that of the superfluid response. In addition, ARSH depends on the presence of magnetic vortices. Also, to interpret the data from these methods, detailed information about the Fermi surface is required. To augment and partially overcome the limitations of these techniques, a new gap nodal spectroscopy method using the anisotropic nonlinear Meissner effect (aNLME) was proposed theoretically by Yip, Sauls, and Xu [43, 52], Dahm and Scalapino [44, 53], and recently manifested in the experiment of Zhuravel et al. [47, 54]. This new gap nodal spectroscopy using the aNLME gives an image of the gap nodal structure from both the bulk superfluid response and the surface Andreev bound state response, for appropriate surfaces [47, 54].

Technique	Advantages	Disadvantages
ARPES[7]	Directly image band structure and gap $\Delta(\vec{k})$	Requires very pristine surfaces, finite energy resolution
SQUID[9]	Sensitive to the sign change of the gap $\Delta(\vec{k})$	Requires high-quality tunnel junctions
ARSH[50]	Relatively simple thermodynamic measurement	Depends on the presence of magnetic vortices Interpretation is dependent on knowledge of Fermi surface details
Raman[8]	Able to choose specific symmetries under test by choosing polarization orientations	Requires detailed theoretical calculations of response functions for each polarization orientation to interpret data
aNLME[45, 47, 54, 55]	Directly image gap nodal structure in real-space, not sensitive to near-surface quality	Requires high-Q resonance with circulating currents over a single-domain sample.

Table 3.1 Summary of some advantages and disadvantages of several representative superconducting gap spectroscopy techniques (not an exhaustive list).

## 3.2 Anisotropic nonlinear Meissner effect

The principle of how the NLME brings out the gap nodal structure is as follows. When an external magnetic field is applied to a superconductor, it generates a supercurrent to expel the field, a hallmark of superconductivity known as the Meissner effect. The kinetic energy invested in this screening current diminishes the difference in free energy between the superconducting and normal states. This means that more superconducting electrons are excited to the normal state at a finite temperature, which leads a decrease in the superfluid density  $n_s(T, \vec{j})$ . As a result, the magnetic penetration depth  $\lambda(T, \vec{j}) \sim 1/\sqrt{n_s(T, \vec{j})}$  increases correspondingly. This effect of the

current density  $\vec{j}$  on  $n_s$  and  $\lambda$  can be expressed in a series expansion. In the regime where the screening current density is small compared to the zero temperature critical current density ( $j/j_c(0) \ll 1$ ), higher order terms have marginal contribution and only the linear and the first non-zero nonlinear terms matter [53].

$$n_s(T, \vec{j}) \cong n_s(T) \left( 1 - b_\Theta(T) \left( \frac{\vec{j}}{j_c(0)} \right)^2 \right) \quad (3.1)$$

$$\lambda^2(T, \vec{j}) \cong \lambda^2(T) \left( 1 + b_\Theta(T) \left( \frac{\vec{j}}{j_c(0)} \right)^2 \right), \quad (3.2)$$

where  $b_\Theta(T)$  is the coefficient of the first non-zero nonlinear term, the so-called non-linear Meissner coefficient.  $\Theta$  represents the direction of the superfluid velocity relative to a reference direction of the gap in k-space (usually the gap antinode direction is set to  $\Theta = 0$ ), and  $\vec{j}$  is the vector current density. Note that the anisotropy of  $b_\Theta(T)$  in k-space is directly determined (calculated) by the nodal structure of the gap function  $\Delta(\vec{k})$ . For example, if the gap function has four nodes and anti-nodes, which is the case of a  $d_{x^2-y^2}$ -wave superconductor,  $b_\Theta(T)$  is also 4-fold symmetric [53]. Vice versa, if one can image the anisotropy of the  $b_\Theta(T)$  in k-space, one can deduce the gap nodal structure.

Experimentally, a thermal perturbation method is suitable to image the anisotropy in  $b_\Theta$ . For the case of gap nodal superconductors such as the  $d$ - or  $p$ -wave cases,  $b_\Theta(T)$  shows a large anisotropic temperature dependence at low temperature  $T/T_c < 0.2$  between situations when the direction of the current is parallel to the gap nodal and anti-nodal direction (Fig.3.2(a),(b)). On the other hand, for the case of an  $s$ -wave or slightly anisotropic  $s$ -wave superconductor, the temperature dependence of  $b_\Theta(T)$

is isotropic and weak for  $T/T_c < 0.2$  (Fig.3.2(c)) (Note that, however, a strongly anisotropic  $s$ -wave superconductor will reveal anisotropic  $b_\Theta(T)$  at low temperature (Fig.3.2(d))). Under a local thermal perturbation which modulates the temperature at a point on the sample, the sharp temperature derivative of  $b_\Theta(T)$  governs the sample nonlinear response at  $T/T_c < 0.2$ . As a result of heating, the modulation in the local superfluid density  $\delta n_s(T, \vec{j})$  ( $\delta \lambda(T, \vec{j})$  equivalently) inherits the anisotropy in  $db_\Theta/dT$  [44, 47], hence creating anisotropy in the electromagnetic response of the superconductor.

The electromagnetic response under a local thermal thermal perturbation is precisely the subject of the LSM-PR measurement. As explained in Chap. 2, LSM-PR measures modulation in the microwave transmission (electromagnetic response) from the superconducting sample under thermal perturbation given by a laser beam. To simply summarize the discussion on the electromagnetic response under a local thermal perturbation so far,

$$\text{PR}(T, \vec{j}) \sim |\vec{j}|^2 \delta \lambda(T, \vec{j}) \sim |\vec{j}|^2 db_\Theta(T)/dT. \quad (3.3)$$

The last piece to finish the puzzle is how the anisotropy of PR in momentum space  $\text{PR}(\vec{j})$  will be measured. The answer is incorporated in the resonator design. What we need to test anisotropy is the response from all possible momentum directions while constraining the magnitude of the momentum to be the same. If one designs a resonator in a way that a uniform (constraining the magnitude) circulating (surveying all momentum directions) current is induced on the surface of the sample, at each

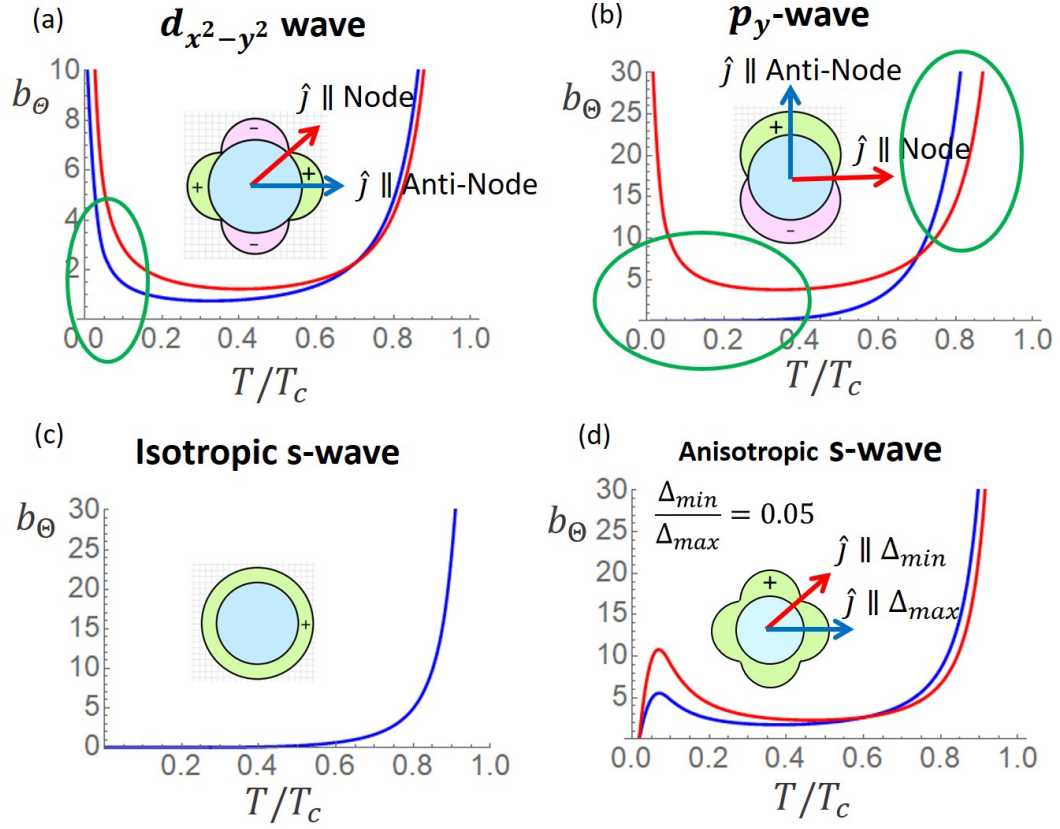


Fig. 3.2 Temperature dependence of the nonlinear Meissner coefficient  $b_{\Theta}(T)$  when the direction of the current is parallel to the gap nodal direction (red) and anti-nodal direction (blue) for the case of (a)  $d_{x^2-y^2}$ -wave superconductor, (b)  $p_y$ -wave superconductor, (c) isotropic  $s$ -wave superconductor, and (d) anisotropic  $s$ -wave superconductor. For the  $s$ -wave case, since there is no gap nodal direction, only one curve is plotted. For the case of the anisotropic  $s$ -wave case, the red line represents the gap minimum direction and the blue line represents the gap maximum direction. The green ovals in (a), (b) denote the temperature regime where the anisotropy in  $b_{\Theta}$  is large. Reprinted with permission from Ref. [38].

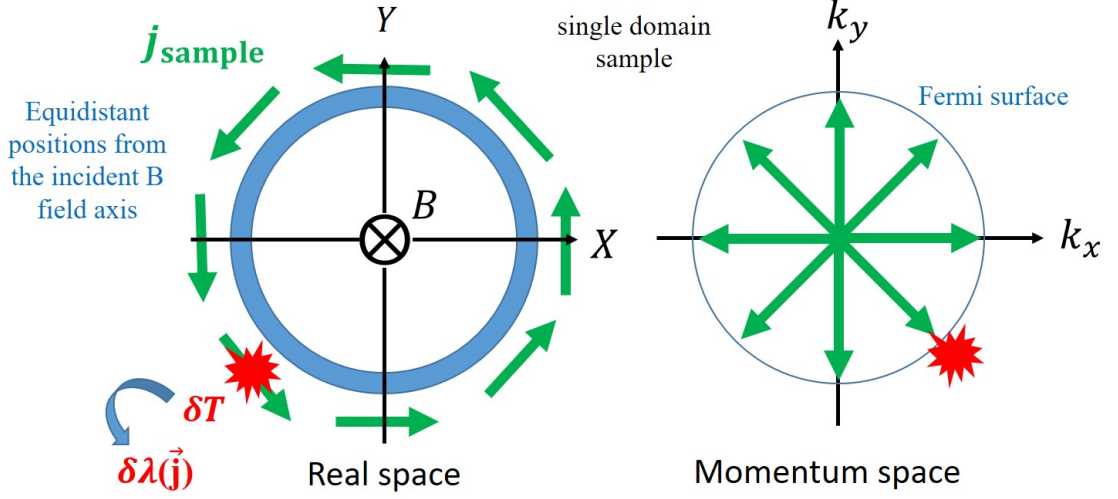


Fig. 3.3 (Left) Schematic view of a circulating current induced by a perpendicular magnetic field  $B$  displayed in real-space (green) induced on the single-domain sample. (Right) Direction of the circulating current displayed in momentum space. A scanning laser beam which provides thermal perturbation  $\delta T$  at a point is displayed in red. The local temperature change  $\delta T$  yields the local change in the penetration depth  $\delta\lambda(\vec{j})$ , resulting in a modulation in the microwave transmission  $PR(\vec{j})$ .

position along the circle, the direction of the current is tangential. The tangential current at each position represents each direction in momentum space, making a one-to-one mapping between real space and momentum-space (Fig. 3.3). Note that the sample should be a single domain (the crystallographic direction should be preserved throughout the area of scanning) for this one-to-one mapping to be valid.

Once the one-to-one mapping is achieved, the focused local laser beam can scan through the positions along the circle. By comparing the magnitude of the  $PR(\vec{j})$  around the full angular range, one can obtain the anisotropy of the electromagnetic response, which is directly related to that of  $b_{\Theta}$ , the gap function, and the pairing symmetry can be finally determined.

### 3.3 First demonstration of LSM-PR as a Gap spectroscope: spiral resonator

The first generation resonator design to satisfy the requirement (uniform circulating current) is a spiral resonator. It starts from a sample in a thin-film form. The thin-film sample is then patterned into a spiral shape through a photo-lithography procedure. For the best performing spiral design, the width of the 40-turn spiral strip is  $10\ \mu\text{m}$  with the same  $10\ \mu\text{m}$  spacing between the spiral strips. The inner diameter of the spiral is 4.4 mm and the outer diameter is 6 mm. The thickness of the thin films was determined in a way that it ensures coherent lattice orientation throughout the film, which was 300 nm for  $\text{YBa}_2\text{Cu}_3\text{O}_{7-x}$  (YBCO) films that are used in our study. The schematic view of the spiral resonator is shown in Fig. 3.4(a).

The spiral strips, if one unfolds and stretches it, are nothing but a long stripline resonator. Hence, it should be self-resonant with standing wave resonances whose resonant frequency is determined by the length of the strip. Fig. 3.4(b) shows a transmission measurement setup which involves the spiral resonator, microwave excitation loop, and pick-up loop. Once the frequency profile of the transmission through the spiral resonator is measured as seen in Fig. 3.4(c) (an example from the niobium spiral), those standing wave resonances are clearly seen. Note that the even harmonics shows lower peak transmission. This is because the field outside the spiral from the currents with opposite directions of the even-order harmonic modes tend to cancel each other.

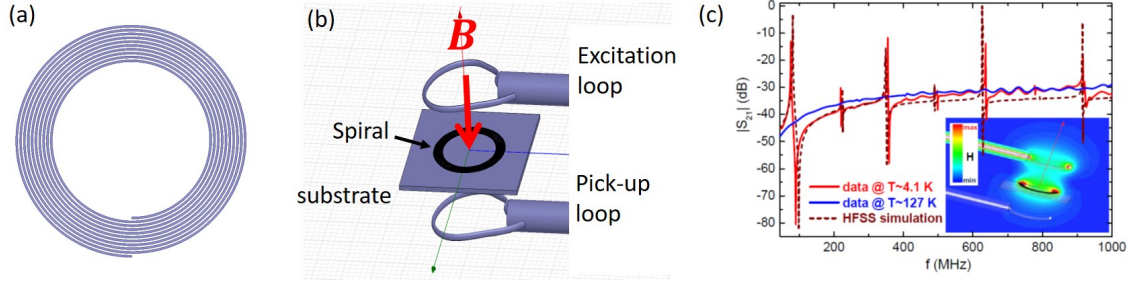


Fig. 3.4 (a) Schematic view of a spiral resonator (Not to scale). The purple part is the spiral strip. (b) Transmission measurement setup for the spiral resonator. The red arrow indicates the direction of the incident of magnetic field from the excitation loop. (c) An example frequency profile of the transmission through a niobium spiral resonator. The fundamental standing wave mode and its harmonics are clearly seen for temperature below  $T_c \approx 9$  K. (c) is reprinted with permission from Ref. [46].

The demonstration of LSM-PR with the spiral resonator as a gap spectroscopy is shown in Fig. 3.5 [47]. The spiral resonator is made with 300 nm thick epitaxial in-plane oriented YBCO thin film grown on  $\text{LaAlO}_3$  (LAO) substrate. The  $T_c$  of the YBCO thin film is  $\approx 91$  K. YBCO is a well-established example of a  $d_{x^2-y^2}$ -wave superconductor. Therefore, as Fig. 3.2(a) shows, one expects mostly isotropic PR image in the high temperature region  $T > 0.7T_c$  and sharp anisotropy in PR images in the low temperature region  $T < 0.1T_c$ . Indeed, the PR data taken at 81.9 K is isotropic as seen in Fig. 3.5(a). Note that the three ring patterns along the radial direction are present because the data was taken from the 3rd harmonic mode ( $f_0 \approx 375$  MHz). In contrast, the PR image taken at 4.4 K is clearly anisotropic and shows a 4-fold symmetric pattern which is expected from the angular dependence of the gap function and  $b_\theta$  of a  $d_{x^2-y^2}$ -wave superconductor.

These results demonstrate the performance of the LSM-PR with the spiral resonator as a gap spectroscopy. In the following Chap. 4, we will discuss new types

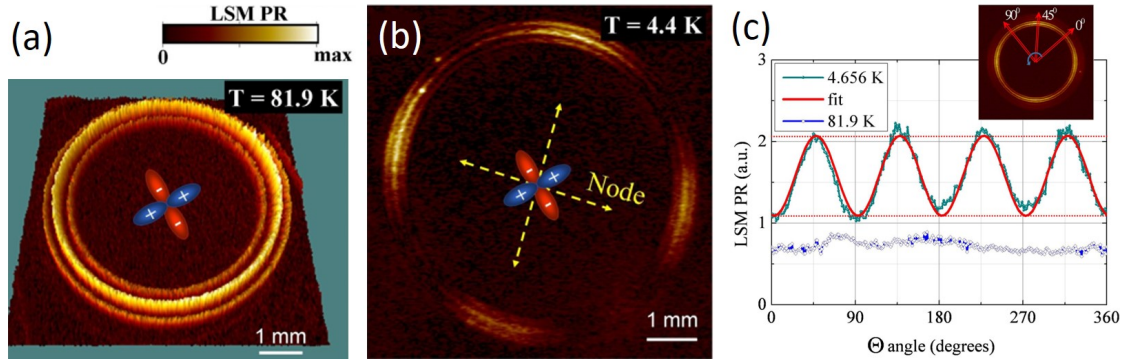


Fig. 3.5 PR images from a YBCO spiral on LAO substrate at (a) 81.9 K, which is  $T > 0.7T_c$  and (b) 4.4 K, which is  $T < 0.1T_c$ . The blue and red ellipses represent the gap antinodal directions with opposite sign, and yellow dashed arrows represent the gap nodal directions. (c) Angular dependence plot ( $PR(\Theta)$ ) of the PR image in the inset. Here, the  $\Theta = 0$  direction is aligned to the gap antinodal direction. Reprinted with permission from Ref. [47].

of PR image pattern which originates from the surface response in this  $d_{x^2-y^2}$ -wave superconductor that emerges at lower measurement temperature. The new features in PR at lower temperature shows that LSM-PR technique is sensitive not only to the bulk response and but also the surface response. In Chap. 5, a shortcoming of the spiral resonator will be discussed, and the second generation resonator design which overcomes the shortcoming will be introduced and demonstrated.

# CHAPTER 4

---

## Gap Nodal Spectroscopy through Anisotropic

## Nonlinear Meissner Effect - Surface response

---

- This Chapter expands upon material previously published as Ref. [54].
- Recommended readings for this chapter: [54, 56–61]

### 4.1 Rotation of the PR pattern - new PR origin

As seen from the previous chapter, LSM-PR measurements on the YBCO spiral, whose anisotropy originates from the nonlinear Meissner effect, shows a clear 4-fold symmetric image (Fig. 4.1(a)) [47], confirming the  $d_{x^2-y^2}$ -wave pairing symmetry of YBCO. The image shows larger PR when the current density  $\vec{j}$  is parallel to the gap nodal direction compared to the antinodal direction ( $PR_N > PR_{AN}$ ). This is consistent with intuition because one expects more quasi-particle creation under external thermal perturbation where the gap is small (i.e., a gap nodal direction).

However, as the system is further cooled down, a phenomenon which goes against this intuition occurs. The PR image at 3.9 K (Fig. 4.1(b)) [47] shows a 45° rotated pattern, such that now  $PR_{AN}$  is larger than  $PR_N$ . This appearance of the rotated PR pattern implies a new origin of PR, which is qualitatively different from the typical bulk diamagnetic nonlinear Meissner effect. The new PR pattern also implies the new mechanism dominates the response of the sample below a certain "cross-over" temperature  $T_{cr}^{PR}$ . For the YBCO spiral on a different substrate (sapphire) where PR is studied continuously as a function of temperature, this cross-over behavior is more clear (Fig. 4.1(c)).

This cross-over behavior might look puzzling. However, it turned out that a similar cross-over behavior was observed in the temperature dependence of the magnetic penetration depth of YBCO crystals [59, 62], where the behavior at the lower temperature was attributed to the response from the surface Andreev bound states (ABS) which are predicted to exist in a  $d_{x^2-y^2}$ -wave superconductor [56]. With theoretical modeling for the PR estimation from the ABS, the cross-over behavior in the temperature dependence, input microwave power  $P_{RF}$  dependence [54], and angular ( $\Theta$ ) dependence are explained in the following sections, supporting the interpretation that rotation of the PR pattern upon cooling down is due to ABS response.

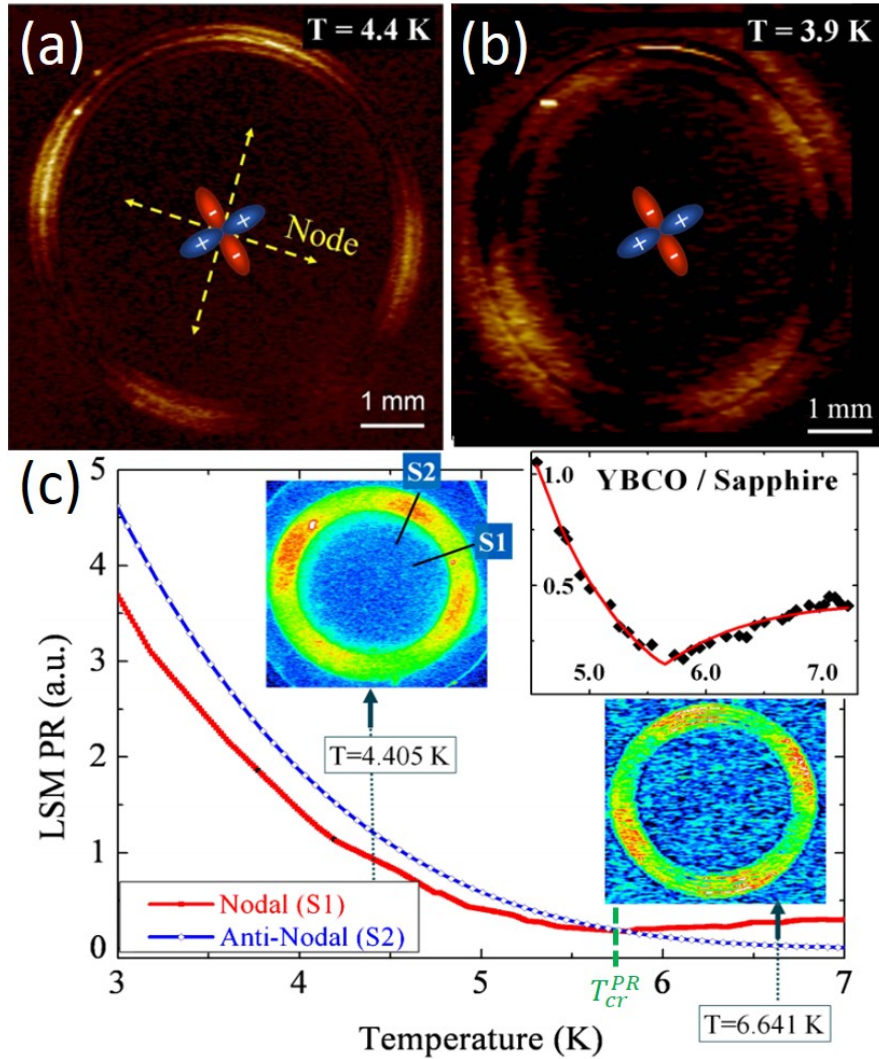


Fig. 4.1 (a) PR image from the YBCO/LAO spiral at 4.4 K and (b) 3.9 K [47]. The LSM PR pattern rotates  $45^\circ$  at 3.9 K. (c) Temperature dependence of the PR from a YBCO/sapphire spiral, along the gap nodal ( $PR_N$ ) and antinodal ( $PR_{AN}$ ) directions. The inset PR images shows PR images below and above the cross-over temperature  $T_{cr}^{PR}$ . Inset is a close-up plot of  $PR_N(T)$  near  $T_{cr}^{PR}$  from the YBCO/Sapphire spiral. Reprinted from Ref. [47].

## 4.2 Paramagnetic Meissner effect from surface Andreev Bound states

### 4.2.1 Formation of surface Andreev bound states

At the boundary of a  $d_{x^2-y^2}$ -wave superconductor, the superconducting order parameter is suppressed approximately for a distance given by the coherence length  $\xi$  (roughly the size of a Cooper pair) [63, 64]. This is due to a sign change of the pair potential between the incident and reflected Cooper pair at the boundary. This normal state region (N region) has two boundaries. One is the physical boundary of the material and the other is the interface between the normal region and the fully superconducting region (SC region). At the interface of the N and SC region, the normal electrons whose energy is smaller than the superconducting gap ( $E < \Delta$ ) cannot penetrate into the SC region because there are no allowed quasiparticle states within the energy gap in the SC region. Instead, the normal electron penetrates into the SC region by forming a Cooper pair by "borrowing" an electron with opposite-signed energy and momentum,<sup>1</sup> which leaves a hole with opposite energy and momentum to be reflected in the normal region, as depicted in Fig. 4.2(a).

The reflected hole now propagates to the physical boundary of the superconductor, is reflected, comes back to the interface, reflected as an original electron with another Andreev reflection, and eventually comes back to its starting point (Fig. 4.2(b)). If the phase accumulated during one cycle of this closed path travel is an integer multi-

---

<sup>1</sup>The zero of energy is the Fermi energy here.

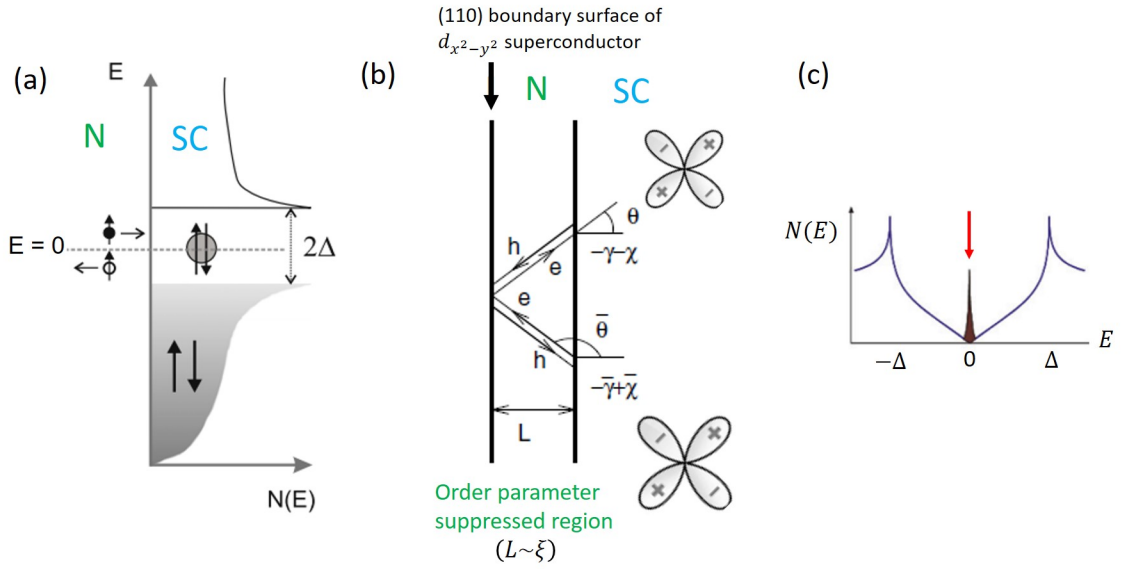


Fig. 4.2 (a) Schematic illustration of the Andreev reflection (AR) at the interface between normal and superconducting region [65]. A normal electron (black circle) finds its pair electron with opposite energy and momentum, forms a Cooper pair, and penetrates into the superconducting region, which leaves a reflected hole (empty black circle). (b) Illustration of (110) physical boundary of a  $d_{x^2-y^2}$ -wave superconductor and an order parameter suppressed normal region (N) [58]. A fully superconducting region (SC) is adjacent to it. The normal carriers (electrons and holes) are traveling a closed path consisting of two ARs and one reflection at the physical boundary. The bulk order parameters that carriers see at each AR are also drawn. (c) An expected density of states for a  $d_{x^2-y^2}$  superconductor with (110) boundaries. The peak at  $E = 0$  (red arrow) is due to the surface bound state due to Andreev reflections.

ple of  $2\pi$ , the electron forms a bound state (i.e., it satisfies the Bohr-Sommerfeld quantization condition). This bound state due to Andreev reflection is called an Andreev bound state (ABS). The electron (and hole) acquires phase from electron Andreev reflection ( $-\gamma - \chi$ ) and hole Andreev reflection ( $-\bar{\gamma} + \bar{\chi}$ ), as well as the round trip propagation between the physical boundary and interface ( $\beta(E) \approx 4LE/\hbar v_F \cos \theta$ ). Here,  $\gamma = \arccos[E/\Delta]$  ( $\bar{\gamma} = \arccos[-E/\Delta]$ ) is the reflection phase shift at the interface and  $\chi$  ( $\bar{\chi}$ ) is the phase of the order parameter, which the incident electron (hole) sees.  $L \sim \xi$  is the thickness of the normal region, and  $\theta$  is an incident angle of electrons to the interface. The total accumulated phase during one cycle of travel becomes [58],

$$-(\gamma + \bar{\gamma}) - (\chi - \bar{\chi}) + \beta(E) = 2n\pi, \quad (4.1)$$

where  $n = 0, \pm 1, \pm 2, \dots$  to achieve constructive interference and a bound state. The order parameter of a  $d_{x^2-y^2}$ -wave superconductor is anisotropic and changes its sign every  $90^\circ$  on the Fermi surface (Fig. 4.2(b)). The relative phase difference of the order parameter for two Andreev reflections  $\chi - \bar{\chi}$  varies depending on the orientation of the boundary (and hence interface) relative to the orientation of the crystallographic axis. If the sample has a (110) boundary where the boundary makes a  $\pi/4$  angle (gap nodal direction) to the a-axis of the lattice (gap antinodal direction), the electron and hole see order parameters with an opposite sign during the two ARs ( $\chi - \bar{\chi} = \pi$ ) regardless of their incident angle  $\theta$ , as illustrated in Fig. 4.2(b). This condition  $\chi - \bar{\chi} = \pi$  yields quite an interesting consequence. Eq. (4.1) now becomes (again, after taking cosine

of both sides of the equation)

$$E/\Delta = \cos \frac{\beta(E) - (2n-1)\pi}{2} = \pm \sin \left( \frac{E}{\Delta} \frac{2L}{\xi \cos \theta} \right), \quad (4.2)$$

which has a solution at  $E=0$  for any value of  $\theta$ . Therefore, regardless of the incident angle of the electrons, the electrons form zero energy bound states, and hence it is expected to show a sharp peak in the density of states (DOS) at  $E = 0$  (Fig. 4.2(c)) on this exposed surface of a  $d_{x^2-y^2}$  superconductor.

#### 4.2.2 Energy level splitting of ABS due to the Doppler shift

The existence of the predicted surface zero energy Andreev bound state (ABS) at the (110) boundary of the  $d_{x^2-y^2}$ -wave superconductor [56] is indeed experimentally verified by a zero-bias conductance peak (ZBCP) in the point-contact spectroscopy measurement [57]. The existence of zero energy ABS results in an interesting response in terms of the applied magnetic field. When an external magnetic field is applied to the ABS, peak splitting occurs in the ZBCP due to the Doppler shift. The scheme of how the Doppler shift splits a ZBCP is shown in Fig. 4.3. First, the applied magnetic field induces a screening superfluid motion ( $v_s$ ) (Fig. 4.3(a)). For the quasiparticles generated by the depaired superfluid, some may move in the same direction as the superfluid and the others move in the opposite direction. The relative velocity of these co ( $v_{co}$ ) and counter ( $v_{ct}$ ) moving quasiparticles seen from the frame of the superfluid is  $\pm v_F$  (Fermi velocity) (Fig. 4.3(b)). In the lab frame, the net velocity of the co and

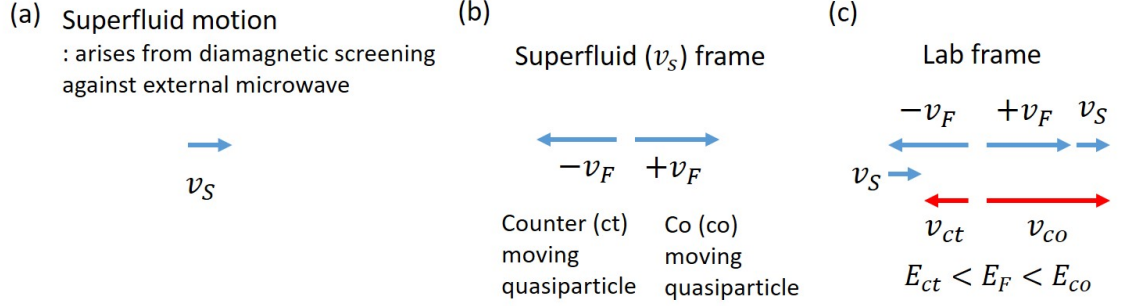


Fig. 4.3 Illustration of the energy level splitting between quasiparticles (normal carriers) moving in the same direction (co-moving) and the opposite direction (counter moving) to the screening superfluid motion under the external magnetic field. (a) shows the direction of the superfluid velocity  $v_s$ , (b) shows quasiparticle velocity  $v_F$  seen in the moving frame of the superfluid, and (c) shows quasiparticle velocity of counter-moving  $v_{ct} = v_s - v_F$  and co-moving  $v_{co} = v_s + v_F$  electrons in the lab frame, and a comparison of their corresponding kinetic energies.

counter moving quasiparticles are  $v_{co} = v_s + v_F$  and  $v_{ct} = v_s - v_F$  each, which is exactly analogous to the Doppler shift. Therefore, if one compares the speeds,  $|v_{ct}| < |v_F| < |v_{co}|$ , and this splits their kinetic energy in the following order:  $|E_{ct}| < |E_F| < |E_{co}|$  (Fig. 4.3(c)).

### 4.2.3 Consequence of the energy level splitting: paramagnetic Meissner effect

For the case of zero-energy ABS, this Doppler shift splits the ZBCP into counter-moving electron states below zero energy  $E_{ct} < 0$  and co-moving electron states above zero energy  $E_{co} > 0$ . At a high temperature where the thermal fluctuations are much larger than the energy splitting, both states are equally occupied. However, as the temperature goes down, the counter-moving states are preferentially occupied (Fig.

4.4(a)). If one remembers that superfluid flows in a direction which gives a diamagnetic response to the external field, one may notice that the co-moving quasiparticles also give a diamagnetic response, while the counter-moving quasiparticles give a paramagnetic response. This means that the paramagnetic response starts to dominate the response of the surface ABS as the temperature goes down and thermal fluctuations are suppressed.

Indeed, as briefly mentioned at the end of Sec. 4.1 several studies on the temperature dependence of the magnetic penetration depth in  $d_{x^2-y^2}$  superconductors showed a dominant diamagnetic response in the high temperature region (Fig. 4.4(b)). As the temperature decreases, the number of bulk quasiparticles decreases, the diamagnetic screening becomes stronger, and the penetration depth decreases. However, below a certain temperature where the thermal excitation is suppressed below the energy splitting of the ABS, the surface paramagnetic response starts to dominate, which leads to an increase of the penetration depth. Note that as Ref. [59, 62] showed, this paramagnetic surface response appears most clearly when the sample has an exposed (110) boundary which yields the  $\pi$ -phase difference in the order parameter between two Andreev reflections.

Now the question for the YBCO spiral resonator, which showed the cross-over behavior in its PR images, is whether it possesses (110) boundary surfaces. It turns out that during the epitaxial thin film growth, YBCO is very susceptible to develop twin boundaries along the (110) direction. A twin boundary is an interface between two domains whose lattice vector directions are swapped. As seen in Fig. 4.5(b-c), for the case of a YBCO thin film, the  $a$ -axis and  $b$ -axis of the lattice vector changes

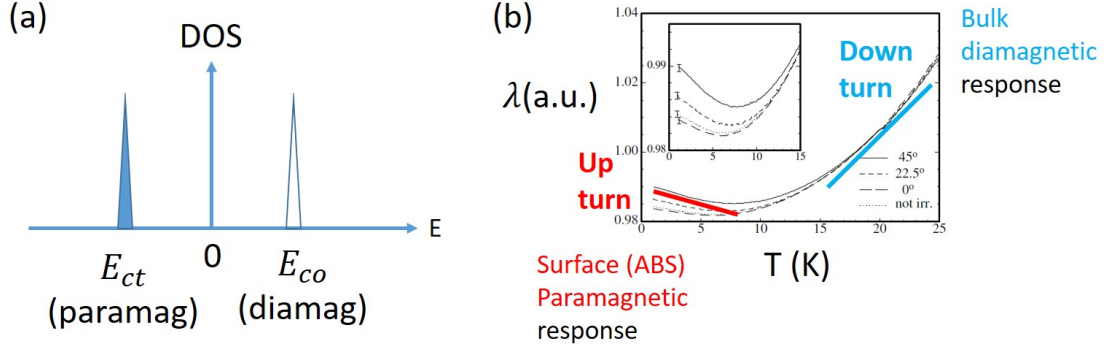


Fig. 4.4 (a) Surface density of states split into counter-moving states  $E_{ct} < 0$  and co-moving states  $E_{co} > 0$  due to the Doppler shift in the presence of a supercurrent flow. As  $T \rightarrow 0$ , only the  $E_{ct}$  states are occupied, producing a paramagnetic response. (b) Temperature dependence of the penetration depth of YBCO thin films with different angles between the boundary direction and a-axis of the lattice (Ref. [62]).

its orientation across the twin boundary, and hence the twin domain boundary gives a (110) termination at the boundary. This internal (110) domain boundary can host zero energy ABS and its paramagnetic Meissner effect (PME) even without physically cleaving the film in the (110) direction.

### 4.3 Theoretical model for Andreev bound State PR

Given the existence of (110) twin boundaries of the YBCO spirals which host surface ABS, a quasi-classical Green function approach is introduced to describe how a  $d_{x^2-y^2}$  superconductor sample with twin boundaries responds to external microwave magnetic field (basically calculating the induced current density of the sample). Then, from the calculated microwave field response of the sample (Sec. 4.3.1) and a theo-

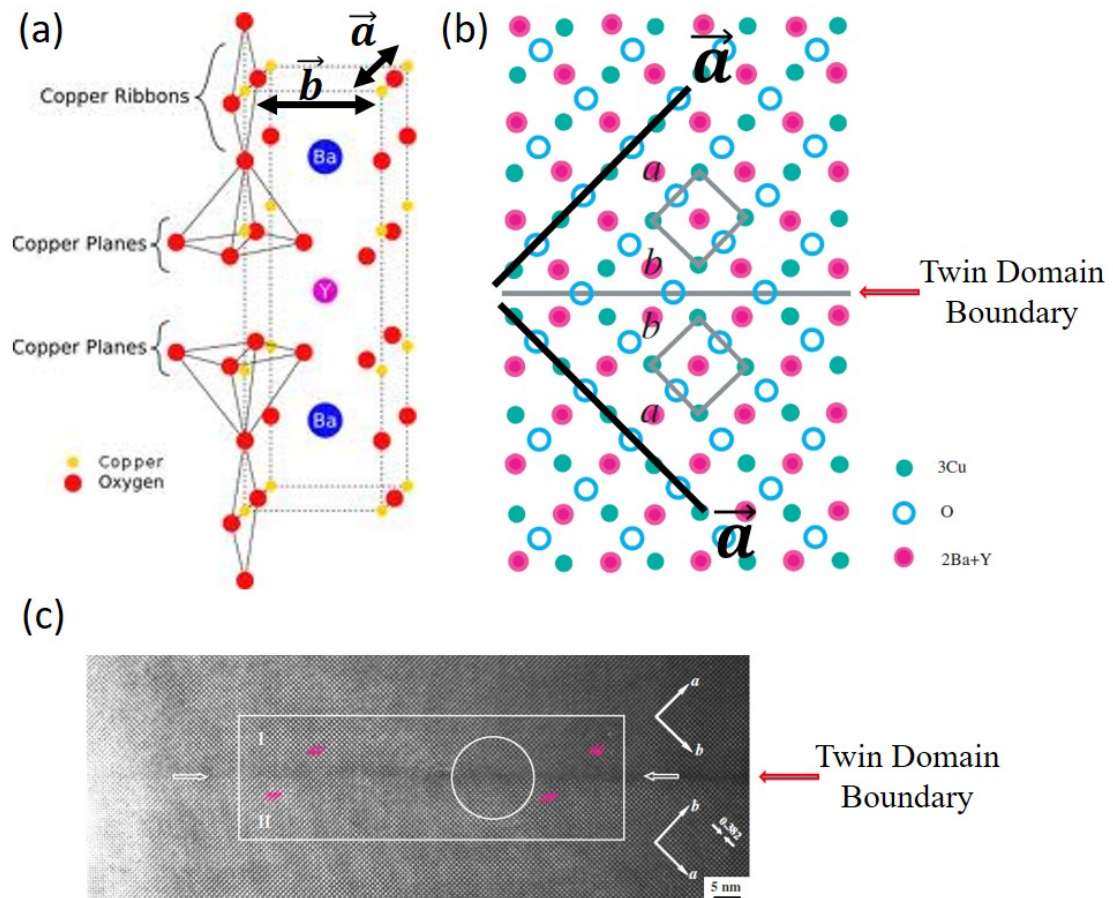


Fig. 4.5 (a) Crystal structure of YBCO. The Cu-O-Cu chain corresponds to the  $a$ -axis direction and the O-Ba-O chain direction is the  $b$ -axis direction. (b) Top view of the twin boundary of YBCO. Across the boundary, the  $a$  and  $b$ -axis directions are swapped. (c) Electron microscope image of a twin boundary of YBCO [66].

retical model of the PR (Sec. 4.3.2), the experimentally observed cross-over behavior in the temperature dependence of PR will be theoretically reproduced. Also, the anisotropy (angular dependence) and input microwave power ( $P_{RF}$ ) dependence of the photoresponse will be estimated and the results will be compared to experimental data (Sec. 4.3.3). The agreement between the estimation and the experimental result will further verify the claim that the new type of PR (Fig. 4.1(b-c)) below the cross-over temperature  $T_{cr}^{PR}$  originates from the paramagnetic Meissner effect from the surface ABS.

#### 4.3.1 Calculation of the surface and bulk current density

First, when an external microwave magnetic field is applied to such a sample, it induces current both in the bulk and on the boundary surfaces of the sample. The transport phenomena in a superconductor can be described by a quasi-classical Green function in Nambu space  $\hat{G}(r, \hat{v}_F, \omega) = \begin{pmatrix} g & f \\ f^\dagger & g^\dagger \end{pmatrix}$  which satisfies the Eilenberger equation [67–69].<sup>2</sup> Here,  $g$  and  $f$  are normal and anomalous components of the Green function  $\hat{G}$  of a given system. The induced current under the external magnetic field can be calculated from this Green function [60, 71, 72]. The resulting current density is given by

$$j(r) = -j_0 \frac{T}{T_c} \sum_{\tilde{\omega} > 0} \langle \hat{v}_F \text{Im}g(r, \hat{v}_F, \tilde{\omega}) \rangle_{v_F}, \quad (4.3)$$

---

<sup>2</sup>For those who want a more extensive introduction and details of the quasi-classical Green function formalism, please refer to a chapter in the well-written textbook Ref. [70], and anonymous lecture note (<https://openaccess.leidenuniv.nl/bitstream/handle/1887/14751/02.pdf?sequence=7>).

where  $j_0 = 4\pi e N(E_F) v_F T_c$ , and  $N(E_F)$  is the density of states at the Fermi energy,  $r$  is the distance from the boundary surface,  $\langle \dots \rangle_{v_F}$  represents averaging over the Fermi surface,  $\hat{v}_F = \vec{v}_F / v_F$  is the unit vector along the direction of the Fermi velocity, and  $\tilde{\omega} = \omega_n + i\vec{p}_F \cdot \vec{v}_s$  represents the Matsubara frequencies under the external magnetic field where  $\vec{v}_s$  is the superfluid velocity and  $\hbar\omega_n = \pi k_B T (2n + 1)$ . In the case when the boundary surface is aligned with the (110) crystallographic direction, which is true for a twin boundary in YBCO, the normal component of the Green function at the surface  $g(0)$  and the homogeneous bulk  $g(\infty)$  are obtained as [60]

$$g(0) = \frac{\tilde{\omega}(\Omega + \bar{\Omega})}{\Omega\bar{\Omega} + \tilde{\omega}^2 + \Delta\bar{\Delta}}, \quad (4.4)$$

$$g(\infty) = \frac{\tilde{\omega}}{\Omega}. \quad (4.5)$$

Here,  $\Delta = \Delta_0(T, \vec{v}_s) \cos 2(\theta - \chi)$  is the angle dependent order parameter where  $\Delta_0(T, \vec{v}_s)$  is the magnitude of the order parameter of a bulk  $d_{x^2-y^2}$  superconductor at temperature  $T$  and superfluid velocity  $\vec{v}_s$ , which can be obtained by solving the self-consistent gap equation. Here, as seen in Fig. 4.6,  $\theta$  is the angle between  $\vec{v}_F$  and the superfluid velocity  $\vec{v}_s$ .  $\chi$  is the angle between  $\vec{v}_s$  (tangential direction of a position on the spiral) and the a-axis direction of the YBCO film (or gap antinode direction equivalently).  $\chi$  can be mapped into the real-space angle  $\Theta$  of the spiral in Fig. 3.5(c).  $\Omega = \sqrt{\tilde{\omega}^2 + \Delta^2}$  is the quasi-particle energy spectrum. Note that barred quantities represent those after reflection from the surface boundary and unbarred quantities represent those before

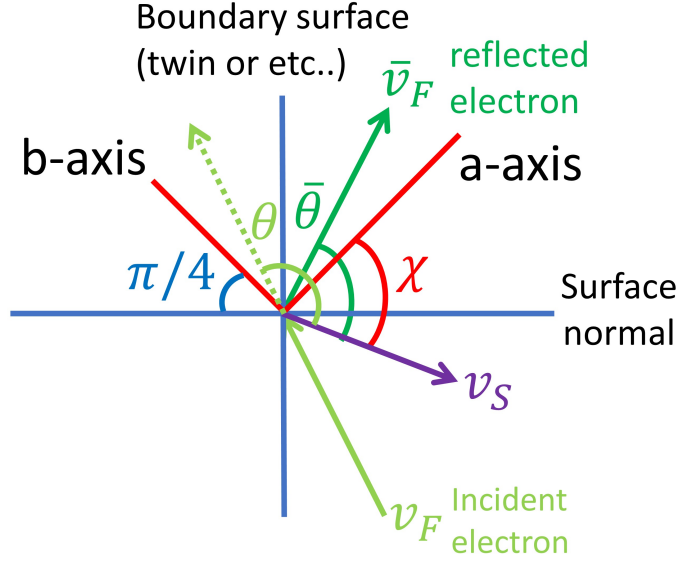


Fig. 4.6 Diagram showing the geometry setup of the sample system. The vertical blue line is the boundary surface, which is a twin boundary in the YBCO spiral sample. The red lines are the  $a$  and  $b$ -axis directions of the sample, which make a  $\pi/4$  angle to the boundary surface. The green arrows show the direction of an incident ( $\vec{v}_F$ ) and reflected ( $\vec{v}_F$ ) quasi particle from the Andreev bound state at the surface. The purple arrow is the direction of superfluid  $\vec{v}_s$  driven by the external microwave field.  $\theta$  (or  $\bar{\theta}$ ) is the angle between  $\vec{v}_F$  (or  $\vec{v}_F$ ) and  $\vec{v}_s$  (see green arcs).  $\chi$  is the angle between the  $a$ -axis direction and  $\vec{v}_s$ . Since  $\vec{v}_F$  and  $\vec{v}_F$  are mirror images of each other through the boundary surface,  $[(\theta - \chi) + (\bar{\theta} - \chi)]/2 = \pi/4$ . Note that as one moves around the spiral, the direction of  $\vec{v}_s$  changes but the direction of the twin surface and  $a, b$ -axis directions of the sample do not change.

reflection, which means  $(\theta - \chi) + (\bar{\theta} - \chi) = \pi/2$ . Therefore,

$$\bar{\Delta} = \Delta_0(T, \vec{v}_s) \cos 2(\pi/2 - (\theta - \chi)) = \Delta_0(T, \vec{v}_s) \cos(\pi - 2(\theta - \chi)) = -\Delta, \quad (4.6)$$

$$\bar{\Omega} = \sqrt{\tilde{\omega}^2 + \bar{\Delta}^2} = \sqrt{\tilde{\omega}^2 + (-\Delta)^2} = \Omega. \quad (4.7)$$

With the Green function presented above, the current density of the bulk Meissner state  $j_{bulk}$  and of the surface Andreev bound state  $j_{surf}$  for various experimental parameters can be calculated. For a validation of the presented numerical scheme,

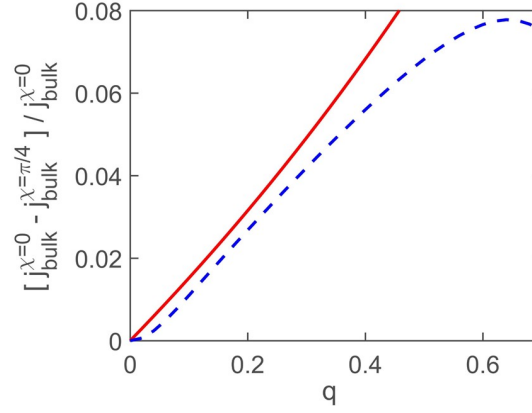


Fig. 4.7 Anisotropy ratio in the bulk Meissner current density, written as the relative value of  $j_{bulk}$  for the angles  $\chi = 0$  and  $\pi/4$ , as a function of superfluid momentum  $q = p_F v_s / \Delta_0$ . The solid line illustrates Eq. (4.8) which ignores superfluid momentum dependence of the order parameter  $\Delta_0 = \Delta(T, \vec{v}_s = 0)$ , while the dashed line is the result of the numerical calculations, which take into account the dependence of  $\Delta_0 = \Delta(T, \vec{v}_s)$ , demonstrated at low temperature,  $T/T_c = 0.05$ .

its result is compared to the famous Yip and Saul's result [52] where they derive a theoretical formula for the superfluid momentum  $q(= p_F v_s / \Delta_0)$  dependence of the anisotropy ratio of  $j_{bulk}$ , defined as the relative value of the  $j_{bulk}$  for the angles  $\chi = 0$  and  $\pi/4$ . It is given as,

$$\frac{j_{bulk}^{\chi=0} - j_{bulk}^{\chi=\pi/4}}{j_{bulk}^{\chi=0}} = q \frac{\sqrt{2} - 1}{2\sqrt{2} - q}. \quad (4.8)$$

This is demonstrated in Fig. 4.7 by the solid red line. The result from this theoretical formula Eq. (4.8) and the result from our numerical calculation is similar for small  $q < 0.3$  but starts to deviate from each other for large  $q$ . This is because the respective formulas in Ref. [52] are obtained in the first approximation on this parameter  $q$  while the result of our numerical calculation further takes into account the superfluid momentum dependence of the order parameter.

With this validation of our calculation, the temperature- $(T)$  and angular- $(\chi)$  dependence of  $j_{surf}$  and  $j_{bulk}$  is presented in Fig. 4.8. As shown in Fig. 4.8(a), both of the current components increase in magnitude as temperature decreases, but the slope of increase for the case of the current at the surface is much steeper than that of the bulk current, which implies that the surface response will play a much more important role in photoresponse at low temperature. Also, note that the sign of the surface current and bulk current is opposite, which implies that the surface current is a paramagnetic current in contrast to the bulk diamagnetic current. Also note that, as shown in Fig. 4.8(b), the anisotropy of the surface current is much larger than that of the bulk current.

With a proper weighting factor, the average current can be calculated. Assuming that the surface paramagnetic current flows within a depth on the order of the coherence length and the bulk diamagnetic Meissner current flows within a depth on the order of the penetration depth, and they add linearly, the average current density in the sample becomes

$$j_{ave} \cong \frac{1}{\lambda} \int_0^\lambda dx (j_{surf} e^{-x/\xi_0} + j_{bulk} e^{-x/\lambda}) \approx \frac{\xi_0}{\lambda} j_{surf} + 0.5 j_{bulk}. \quad (4.9)$$

Hence the contribution of the surface current relative to that of the bulk current is determined by  $\xi_0/\lambda$  as a weight factor. For the case of YBCO, which is a representative type-2 superconductor, this ratio is quite small ( $\xi_0 \sim 4$  nm,  $\lambda_0 \sim 160$  nm,  $\xi_0/\lambda_0 \sim 0.025$ ) so the sample gives a net diamagnetic response.

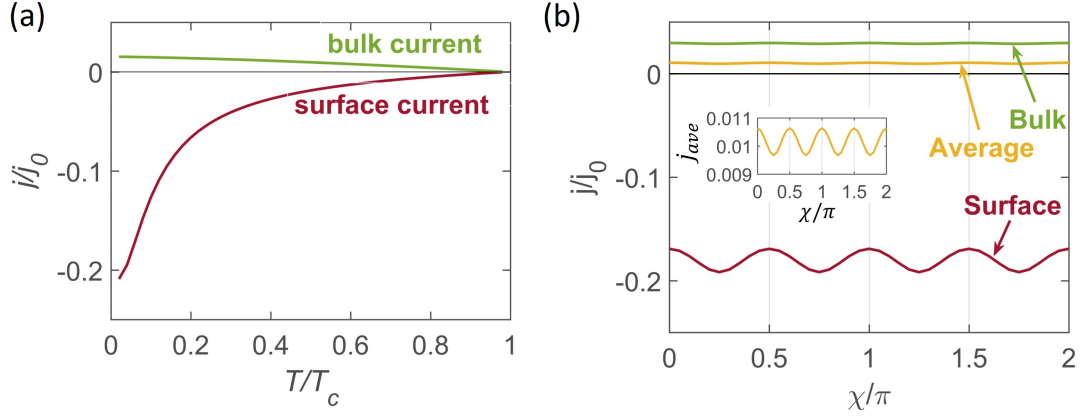


Fig. 4.8 (a) Temperature dependence of the current densities at the surface and the bulk when  $v_s \parallel$  gap node ( $\chi = \pi/4$ ) and superfluid momentum  $q = p_F v_s / \Delta_0 = 0.1$ . The sign of the surface current is the opposite to that of the bulk diamagnetic current which implies the surface current is paramagnetic. (b) The angular dependence of the current density at the surface, bulk, and their average when  $q = 0.2$  and  $T/T_c = 0.05$ . Inset is a close-up plot of average current density vs.  $\chi$ .

### 4.3.2 PR estimation model

With these calculation results for the microwave field response of the sample, a microscopic model can be introduced to estimate the temperature dependence, anisotropy (angular dependence), and input microwave power dependence of the photoresponse. In this model, we shall assume that the photoresponse is entirely inductive in character as a first step for comparison to data. Under the perturbation given by laser illumination, the sample response to the microwave field changes, and the inductive component of this photoresponse (PR) can be estimated as [36]

$$PR \sim \delta f_0 / f_0 \sim -\delta W / W, \quad (4.10)$$

where  $W$  is energy stored in both magnetic fields and kinetic energy of the superfluid. Note that the changes in the field outside the superconducting sample are marginal for small local perturbations on the sample. Therefore the contribution of the outside field on the change in stored energy  $\delta W$  can be ignored and we will focus on the stored energy inside the sample [36]. Also note that the resistive component of PR is not discussed here due to the dominance of the inductive component at low temperature. Also, we lack a quantitative model for the dependence of the dissipation in terms of various experimental parameters, although the qualitative behavior in the anisotropy should be the same as the inductive component. If the magnetic field imposed at the surface of the film is  $B_0$  and the bulk penetration depth is  $\lambda$ , the kinetic and magnetic field energy stored inside the sample in the wide thin film case ( $t$  is comparable to  $\lambda$  and  $st \gg \lambda^2$ ) can be calculated as [36, 73]

$$W = \int_A da \frac{B_0^2 \lambda^2}{\mu_0 t}, \quad (4.11)$$

where  $t \sim 300$  nm is the thickness of the sample,  $s \sim 10$   $\mu$ m is the width of the film (spiral arm),  $\mu_0$  is the permeability of free space, and  $A$  is area of the surface of the spiral with differential area  $da$ . This area integral will be ignored below since we are interested in the angular ( $\chi$ ) and superfluid momentum ( $q$ , or  $P_{RF}$  equivalently) dependence of the perturbation on the local stored energy, so it is sufficient to just discuss stored energy per unit area, which we denote as  $w = B_0^2 \lambda^2 / \mu_0 t$ .

However, when there is a twin domain boundary within the sample, it hosts a paramagnetic surface current ( $K_{surf} = |j_{surf} \xi_0|$ ) at that interface and the part of the

sample nearby the twin boundary experiences an enhanced magnetic field ( $B_{s_0} = B_0 + \mu_0 K_{surf}$ ). We introduce a paramagnetic weighting factor  $p$  which reflects the portion of the sample that experiences an enhanced field  $B_{s_0}$ . This parameter is different for each sample depending on its twin density (note that the  $T_{cr}^{PR}$  varies more than 2 K among different samples, showing a sample variation in the weighting factor  $p$ ). With this parameter introduced, the averaged magnetic field experienced by the sample, corresponding stored energy, and change in stored energy per unit area due to the external perturbation can be written as

$$B_{ave}^2 = (1-p)B_0^2 + pB_{s_0}^2, \quad (4.12)$$

$$w = B_{ave}^2 \lambda^2 / \mu_0 t, \quad (4.13)$$

$$\delta w = \frac{2pB_{s_0}\lambda^2}{t} \delta K_{surf} + \frac{2B_{ave}^2}{\mu_0 t} \lambda \delta \lambda. \quad (4.14)$$

The first term in Eq. (4.14) shows the contribution to nonlinear response from the surface current in an Andreev bound state (ABS) and the second term shows that from bulk current due to the nonlinear Meissner effect.

To estimate the photoresponse, one needs to know  $K_{surf}$  and  $j_{bulk}$  (which in turn gives an estimation for  $\lambda$ ). We have already derived expression for those quantities through Eqs. (4.3-4.7) for the sample geometry in Fig. 4.6. Once the surface ( $K_{surf}$ ) and bulk ( $j_{bulk}$ ) current densities are calculated from the Green function, one can expand them in terms of the superfluid momentum ( $q = p_F v_s / \Delta_0(0, 0)$ ) in the regime

of  $q \ll T/\Delta_0$  [74]

$$K_{surf}(T, q) = j_0 \xi_0 (\alpha_{surf} q - \beta_{surf} q^3 + \dots), \quad (4.15)$$

$$j_{bulk}(T, q) = j_0 (\alpha_{bulk} q - \beta_{bulk} q^3 + \dots), \quad (4.16)$$

$$\lambda^2(T, q) = \lambda^2(T) (1 + b_\chi (j/j_c)^2 + \dots), \quad (4.17)$$

where  $\beta_{surf}$  is the surface ABS nonlinear coefficient,  $b_\chi = \beta_{bulk}/\alpha_{bulk}^3$  is the bulk nonlinear Meissner coefficient [53, 61, 74], and  $j_c$  is the critical current density at  $T = 0$  K. Under illumination by a modulated scanning laser beam, these quantities are modulated ( $\delta K_{surf}, \delta \lambda$  in Eq. (4.14)). The previous experimental study [47] on the temperature dependence of the photoresponse and the theoretical study [61] on the nonlinear Meissner coefficient are consistent with a model which attributes PR to the modulation in the nonlinear terms in the above expansion (Eqs. (4.15-4.17)). This means  $\delta K_{surf} \sim -\delta \beta_{surf} q^3$ ,  $\delta(\lambda^2) \sim \lambda^2(T) \delta b_\chi (j/j_c)^2$ . Then  $\delta w$ , which accounts for PR, becomes

$$\delta w \sim -\frac{2pB_{s0}\lambda^2}{t} \delta \beta_{surf} q^3 + \frac{B_{ave}^2 \lambda^2}{\mu_0 t} \delta b_\chi (j/j_c)^2. \quad (4.18)$$

What insights does this model give to us? Here, the first term represents photoreponse from paramagnetic current in surface Andreev bound states and the second term represents that from diamagnetic Meissner current in the bulk. Therefore, their signs are opposite so they compete with each other. In terms of temperature dependence,  $\delta \beta_{surf}(T)$  which governs the temperature dependence of the surface re-

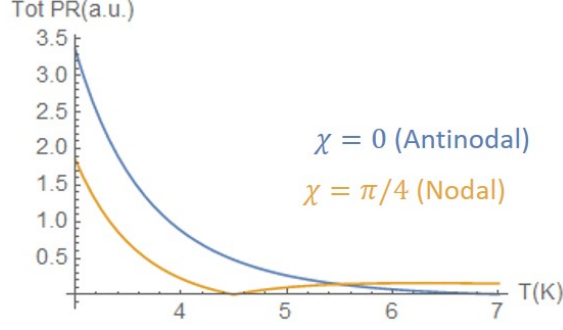


Fig. 4.9 The calculated temperature dependence of the Antinodal ( $\chi = 0$ ) and nodal ( $\chi = \pi/4$ ) PR (magnitude) from the model calculation (Eqs. (4.10),(4.18)).

sponse shows  $\sim 1/T^4$  behavior and  $\delta b_\chi(T)$  which governs that of the bulk response shows  $\sim 1/T^2$  behavior [61]. Hence at low temperature the surface response is expected to dominate, at high temperature the bulk response is expected to dominate, and in the intermediate temperature, PR should touch zero and experience a sign change. In terms of anisotropy, since  $|\beta_{surf}(\chi = 0)| > |\beta_{surf}(\chi = \pi/4)|$  and  $|\beta_{bulk}(\chi = 0)| < |\beta_{bulk}(\chi = \pi/4)|$ , it should be  $PR(\chi = 0) > PR(\chi = \pi/4)$  below the cross-over temperature  $T < T_{cr}^{PR}$  and  $PR(\chi = 0) < PR(\chi = \pi/4)$  for  $T > T_{cr}^{PR}$ .

Indeed, the above model calculation result (Eqs. (4.10),(4.18)) on the overall temperature dependence of the antinodal PR ( $\chi = 0$ ) and nodal PR ( $\chi = \pi/4$ ) for an example value of the paramagnetic weight factor  $p = 0.015$  and critical temperature  $T_c = 92$  K gives the expected cross-over behavior (magnitude of PR touches zero) as seen in Fig. 4.9. Also, the expected flip of the anisotropy in PR is clearly shown:  $PR(\chi = 0) > PR(\chi = \pi/4)$  below  $T_{cr}^{PR} \approx 5.5$  K, and  $PR(\chi = 0) < PR(\chi = \pi/4)$  above  $T_{cr}^{PR}$ .

The above predictions from the model calculation with surface ABS scenario

qualitatively agrees with the experimental observations of PR mentioned in Sec. 4.1 in terms of the temperature dependence (cross-over behavior - zero crossing of PR) and anisotropy (rotation of PR image). This agreement provides strong evidence that the features of the PR images at low temperature should originate from the paramagnetic surface ABS. In the following, it will be also shown that the input microwave power ( $P_{RF}$ ) dependence and the angular dependence ( $\chi$ ) can be quantitatively calculated, and they agree with experimental data, further supporting our claims about surface ABS PR.

### 4.3.3 Comparison of the model calculation and experimental data

With Eqs. (4.10),(4.18), the input microwavepower ( $P_{RF}$ ) dependence and the angular dependence ( $\chi$ ) of the photoresponse at representative  $P_{RF}$  is calculated and compared to those from experimental data [54] as shown in Fig. 4.10(a),(b). Here, the thickness of the film  $t$  is 300 nm. The zero current penetration depth  $\lambda(T)$  which contributes temperature dependence in Eq. (4.17) is obtained from  $\lambda^2(T)/\lambda_0^2 = n/n_s(T) = 1/\alpha_{bulk}$  [44] with  $\lambda_0 = 160$  nm [75]. Note that  $\alpha_{bulk}$  for the clean limit is used here. The nonlinear coefficients  $\beta_{surf}$ ,  $\beta_{bulk}$  (and hence  $b_\chi$ ) are obtained by calculating the third order derivatives of  $K_{surf}$ ,  $J_{bulk}$  with respect to  $q$ :

$$\beta_{bulk}(T, \chi) = -\frac{T}{2\pi T_c} \sum_{\omega_n > 0} \int_{-\pi/2}^{\pi/2} d\theta \frac{\Delta^2(4\omega_n^2 - \Delta^2)}{(\omega_n^2 + \Delta^2)^{7/2}} \Delta_0^3(0, 0) \cos^4 \theta \quad (4.19)$$

$$\beta_{surf}(T, \chi) = -\frac{T}{2\pi T_c} \sum_{\omega_n > 0} \int_{-\pi/2}^{\pi/2} d\theta \frac{\Delta^2(4\omega_n^4 + 5\omega_n^2\Delta^2 + 2\Delta^4)}{\omega_n^4(\omega_n^2 + \Delta^2)^{5/2}} \Delta_0^3(0, 0) \cos^4 \theta \quad (4.20)$$

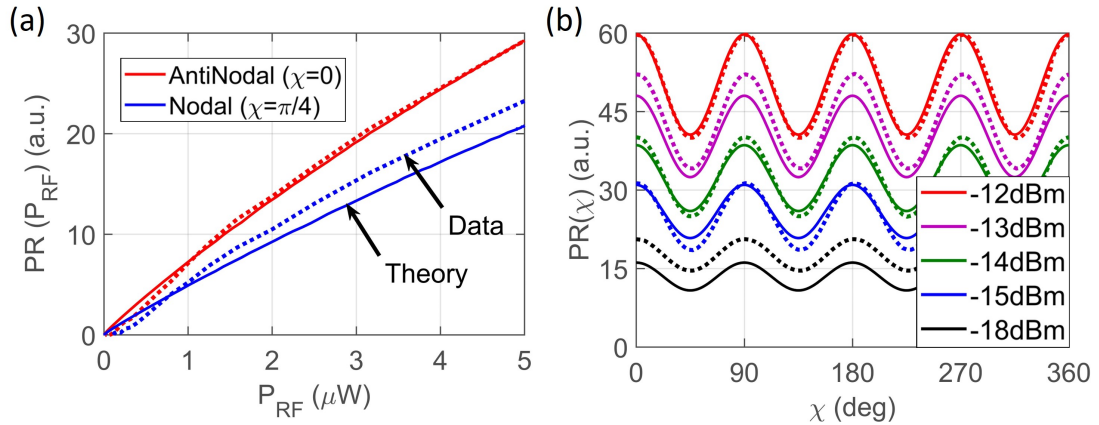


Fig. 4.10 (a) Input microwave power ( $P_{RF}$ ) dependence of total (surface+bulk) PR when  $v_s \parallel$  gap antinode ( $\chi = 0$ ) and  $v_s \parallel$  gap node ( $\chi = \pi/4$ ). The solid lines are the theoretical estimation with the paramagnetic weight factor  $p = 0.015$  at  $T = 0.025T_c$  and the dotted lines are the experimental data at  $T = 3$  K where both temperatures are in the surface response dominant regime. Here, theoretically estimated PR is calculated in arbitrary units. To focus on comparison of the  $P_{RF}$  dependence and anisotropy between the antinodal and nodal PR from the theory and experiment, PR from the theory is re-scaled so that the value of the theoretical and experimental PR in the gap antinodal direction at  $P_{RF} = 5 \mu W$  are the same. (b) The angular ( $\chi$ ) dependence plot of PR at various  $P_{RF}$  shows a 4-fold symmetric pattern which reflects the anisotropic ABS response of the sample. Solid lines are the theoretical estimation curves at  $T = 0.025T_c$  and dotted lines are fitted curves from the experimental data at  $T = 4.8$  K [54]. Again, the same normalization scheme as (a) is used here. PR from the theory is re-scaled so that PR at  $\chi = 0$ ,  $P_{RF} = -12$  dBm is set to be the same as the experimental value.

The modulation in  $\beta_{surf}(T), b_\chi(T)$  is estimated by  $\delta\beta_{surf} = \partial\beta_{surf}/\partial T \times \delta T$  and  $\delta b_\chi = \partial b_\chi/\partial T \times \delta T$ . Since  $\delta T$  is independent of  $P_{RF}$  and  $\chi$ , it is set to be a proportionality constant. For the spiral sample where the experimental data that appeared in this section is taken (a YBCO spiral on MgO substrate), the PR crossover temperature  $T_{cr}^{PR}$  where antinodal PR ( $\chi = 0$ ) becomes larger than nodal PR ( $\chi = \pi/4$ ) is  $\sim 5.6$  K. The  $P_{RF}$  and  $\chi$  dependence of PR are measured well below this temperature ( $T = 3$  K, 4.8 K) where the surface response dominates the total PR. For direct comparison between experiment and theory, PR is theoretically calculated with the choice of the paramagnetic weight factor  $p = 0.015$  in order to give similar  $T_{cr}^{PR} \approx 5.6$  K  $= 0.06T_c$  (for  $T_c = 92$  K) as the experimental value, and the  $P_{RF}$  and  $\chi$  dependence of PR is estimated at about half of the PR crossover temperature  $T = 0.025T_c \sim T_{cr}^{PR}/2$  which again ensures the surface PR dominating regime.

As seen from Fig. 4.10(a), in the theoretical estimation, PR increases as  $P_{RF}$  increases since larger external field drives larger superfluid momentum  $q$ . Also, antinodal ( $\chi = 0$ ) PR is larger than nodal ( $\chi = \pi/4$ ) PR, which is expected for the surface ABS response dominant regime. The anisotropy between antinodal and nodal PR remains about the same throughout the whole  $P_{RF}$  range where the PR is estimated. Note that these estimated behaviors of the  $P_{RF}$  dependence agree well with those of the experimental data plotted together in Fig. 4.10(a).

As presented in Fig. 4.10(b), the theoretical angular dependence of PR shows a 4-fold symmetric pattern which is a signature of the ABS anisotropy. Again, the theoretical and experimental angular dependence mostly agree with each other. The fact that the  $P_{RF}$  and angular dependence results from the presented theoretical estima-

tion are in good agreement with the experimental data confirms that the microscopic model is consistent with the measured photoresponse, and especially, is valid to predict the response from surface Andreev bound states under microwave excitation.

Throughout this section, the origin of the rotation in the PR images obtained from YBCO spirals at low temperature limit is discussed. The presence of the (110) twin boundaries of the YBCO epitaxial thin films which are predicted to host zero energy Andreev Bound state, the similar cross-over behavior in the temperature dependence of the PR from the ABS model calculation, and agreement on input microwave power dependence between ABS PR model and experimental data all suggest the origin of the rotation in the PR images should be due to a strong paramagnetic Meissner effect from the ABS in the low temperature limit.

# CHAPTER 5

---

## Gap Nodal Spectroscopy through Anisotropic

## Nonlinear Meissner Effect - Improvement

---

- This Chapter expands upon material previously published as Ref. [38].
- Recommended readings for this chapter: [38, 76–78]

### 5.1 An issue with the spiral resonator

The above results from LSM-PR measurement on spiral resonators demonstrated its capability as an effective gap spectroscope and has created a great deal of excitement. However, despite the advantages, it has one significant drawback. Patterning a spiral shape on a thin film sample requires an elaborate and potentially destructive lithographic procedure. During the procedure, it is not only easy to degrade the superconducting properties ( $T_c$ , for example) of the film but also easy to create defects (holes, cuts, or shorts, etc) on the spiral. These defects induce sharply peaked current

density distribution around them. This results in PR "hot spots" which dominate the entire PR image and make it difficult to deduce the gap symmetry from the image.

In fact, many of the newly emerged unconventional superconductors of interest are very vulnerable to this defect issue during the lithographic process due to their sensitivity to solvents, water, and the ambient atmosphere. This drawback is demonstrated in Fig. 5.1, which shows optical microscope images of defects in spirals from the iron-based superconductor  $\text{Ba}_{1-x}\text{K}_x\text{Fe}_2\text{As}_2$  and an electron-doped cuprate  $\text{Pr}_{2-x}\text{Ce}_x\text{Cu}_2\text{O}_4$  (PCCO) thin films, and their defect-hotspot dominated PR images.

## 5.2 Second generation resonator: Dielectric resonator

### 5.2.1 Resonator design and simulation

As seen from the previous Sec. 5.1, the limited availability of a stable lithography recipe was an obstacle for the LSM Gap spectroscopy based on the spiral resonator. Naturally, there have been demands for a new resonator design which does not require a patterning procedure so that a greater variety of superconductors can be examined. To satisfy the demands while maintaining all three requirements for the gap spectroscopy via LSM-PR measurement (a high Q resonance mode, uniform circulating current, and optical access for the laser beam), the dielectric resonator (DR) design with an aperture (see Fig. 5.2) is adopted. This DR is a modified version of the Hakki-Coleman type resonator [76, 77]. It consists of a top and bottom metallic

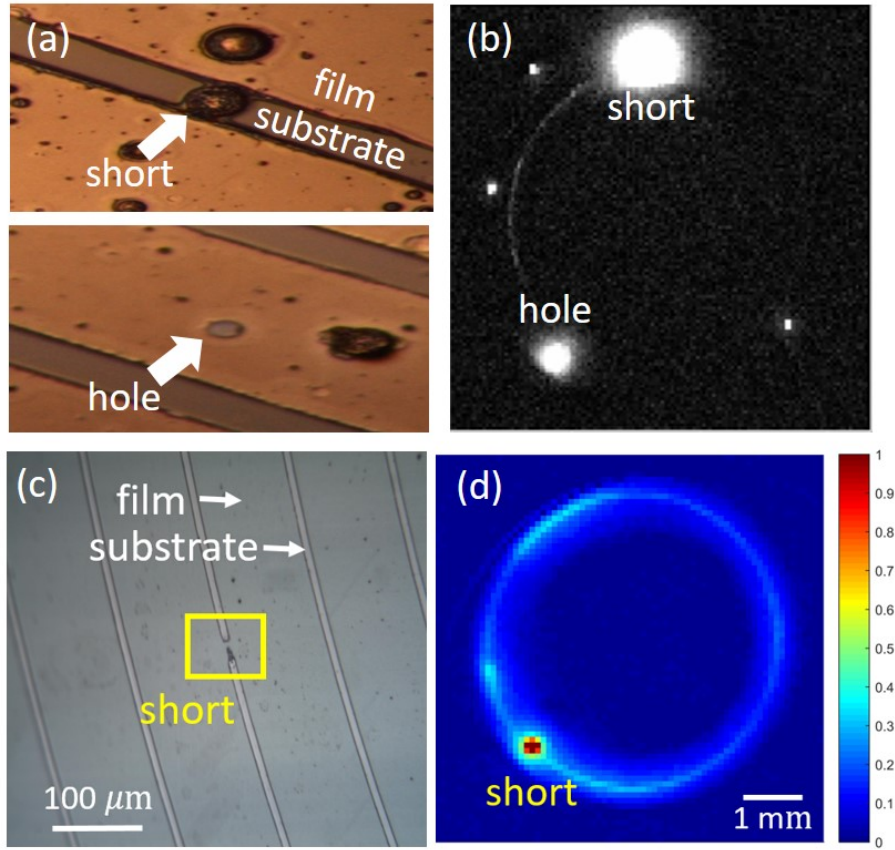


Fig. 5.1 (a) Optical microscope image of a spiral sample made from a  $\text{Ba}_{1-x}\text{K}_x\text{Fe}_2\text{As}_2$  thin films. A hole and shorted parts created during the lithographic procedure are clearly visible. (b) The PR image taken from the  $\text{Ba}_{1-x}\text{K}_x\text{Fe}_2\text{As}_2$  spiral. Brightness represents the magnitude of PR. The hole and shorted parts show bright PR which dominates the PR image. (c) Optical microscope image from the PCCO spiral. Again, a shorted part is visible. (d) PR image from the PCCO spiral. The sharp PR from the shorted part dominates the image. (c-d) are Reprinted with permission from Ref. [38].

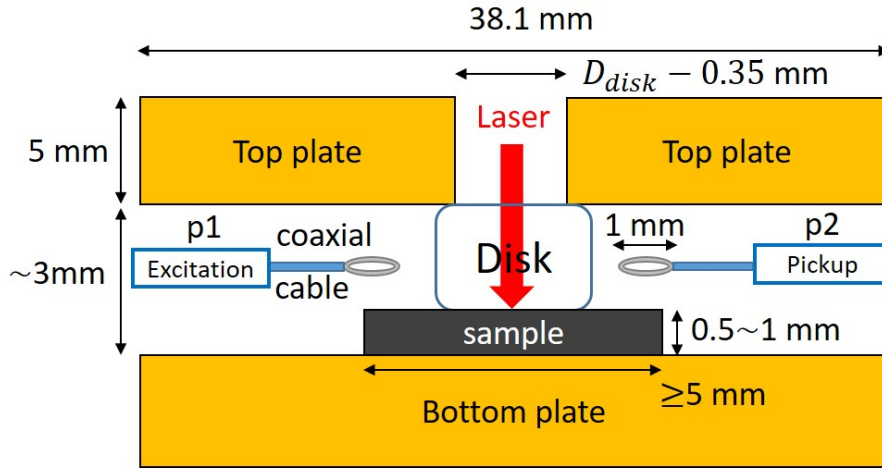


Fig. 5.2 Schematic cross-section diagram of the dielectric resonator (DR) setup with a sample (not to scale). The transparent dielectric disk is sandwiched between the top plate and the sample. The diameter of the dielectric disk  $D_{disk}$  is either 6.35 mm (sapphire disk) or 3 mm (rutile disk). The diameter of the aperture in the top plate is 0.35 mm smaller than  $D_{disk}$ . The resonator is coupled to microwave coaxial cables through magnetic loops.

plate (Cu or Nb) which confine the microwave fields inside the resonator-like a cavity. A cylindrical dielectric disk with high dielectric constant, which is placed on top of a superconducting sample, creates a resonance that induces strong microwave currents on the sample. The resonant frequency  $f_0$  is determined mainly by the dimension and the dielectric constant of the disk. The unpatterned sample is placed in contact with one face of the disk to modify the resonant properties of the DR.

The dielectric material must satisfy three requirements. First is a high dielectric constant  $\epsilon_r$ , that is isotropic in the plane of the sample to concentrate the microwave fields to a small part of the sample. The second requirement is a low loss tangent ( $\tan \delta$ ) at cryogenic temperatures to enable a high quality factor for a microwave resonance.<sup>1</sup> The third requirement is to be transparent at the wavelength of the laser

<sup>1</sup>Maximum quality factor  $< 1 / \text{loss tangent}$ . Low loss tangent means higher quality factor available.

used for thermal perturbation. Sapphire and rutile are the best choices satisfying these requirements. Sapphire has high dielectric constant ( $\epsilon_{a,b,c} \sim 10$  where  $a, b$  are the in-plane crystallographic axes and  $c$  is the out-of-plane axis) and very low loss tangent ( $\sim 10^{-10}$ ) at temperatures below 10 K [79–81]. Rutile has even higher dielectric constant ( $\epsilon_c > 250, \epsilon_{a,b} > 120$ ) and still low loss tangent ( $\sim 10^{-8}$ ) at temperatures below 10 K [78, 82]. Due to the difference in the dielectric constant, sapphire is suitable for a large or homogeneous sample ( $\sim 10 \times 10 \text{ mm}^2$ ) and rutile is suitable for a small sample ( $\sim 5 \times 5 \text{ mm}^2$ ). Both materials are transparent to visible light.

Among the resonant modes generated by the cylindrical dielectric resonator, the  $\text{TE}_{011}$  mode [83] ( $\approx 11 \text{ GHz}$  for the rutile,  $\approx 20 \text{ GHz}$  for the sapphire resonator) shows high quality factor (typically  $> 10^4$  at  $30 \text{ mK}$ )<sup>2</sup>, and provides the desired field configuration on the sample surface. The microwave magnetic field in this mode has a toroidal shape as shown from an high-frequency structure simulator (HFSS) simulation (Fig. 5.3(b)). In response to this field, the superconducting sample generates current which circles around the axial line of the cylindrical disk to screen out the field (Fig. 5.3(c)). Fig. 5.3(d) shows that this microwave current distribution is uniform in its angular distribution. Therefore, the modified DR satisfies all three requirements of the microwave resonator for LSM-PR measurement.

To verify the validity of the presented resonator design as a new gap spectro-  
scope, one must make sure that there is no resonator-geometry induced anisotropy

---

<sup>2</sup>Note that having an aperture of diameter  $D_{aper} = 6 \text{ mm}$  does not noticeably increase the radiation loss. The aperture can be considered as a cylindrical waveguide. The cut-off frequency (the lowest frequency with which a microwave can propagate through a waveguide) of this aperture is  $29.3 \text{ GHz}$ . The measurement frequency is  $20 \text{ GHz}$ . Therefore, the wave which passes through the aperture decays as if it passes through a tunnel barrier.

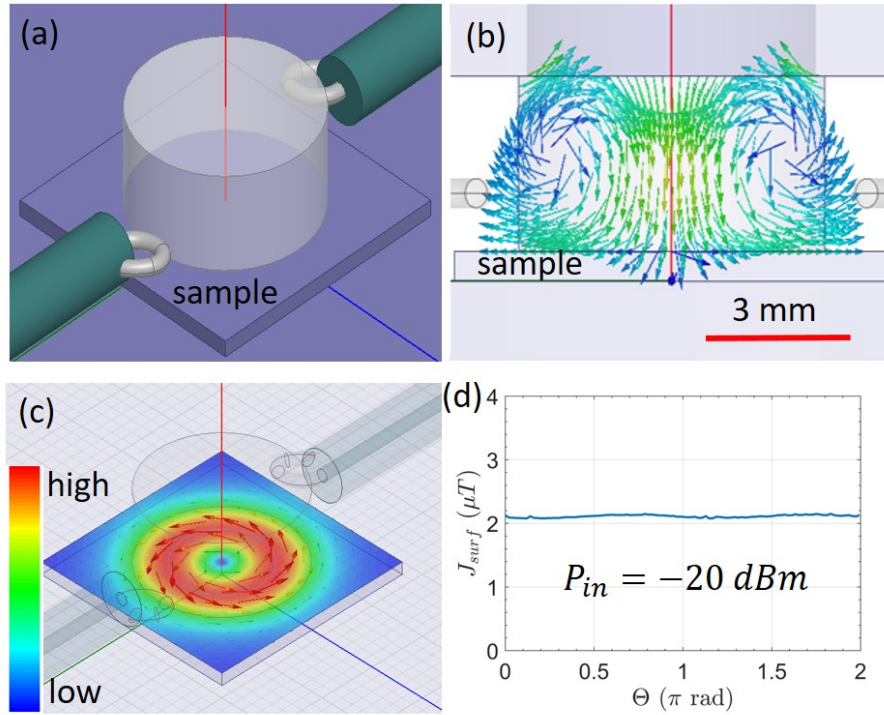


Fig. 5.3 (a) Numerical simulation (HFSS) setup geometry of the DR with a sapphire disk (top plate is hidden from view) to simulate the surface current of the sample and the field distribution of the resonator. Here, the sample is set to a perfect electric conductor (PEC) to mimic the surface current and field response of an ideal superconductor (i.e., no quasi-particles and dissipation) to the external microwave field.<sup>a</sup> (b) Microwave magnetic field density plot inside the dielectric disk in the  $TE_{011}$  resonance mode ( $f_0 \sim 20$  GHz). (c) Surface current density plot on the sample and (d) its angular dependence for an input RF power  $P_{in} = -20$  dBm. The angular ( $\Theta$ ) dependence of the induced current density is nearly constant.

<sup>a</sup>The PEC condition sets the electric field inside the object to zero. It does not screen out DC magnetic field inside the object. In contrast, a PEC object screens out the microwave magnetic field. This is because a microwave electromagnetic field is a time-varying electric field and magnetic field that induce one to the other. Therefore, canceling the electric field (and hence its time variation) inside the object leads to the exclusion of the time-varying magnetic field.

in the circulating current distribution. As seen from the expression to estimate the inductive and resistive PR in Eqs.(2.4),(2.5), the anisotropy of PR can arise from both sample-intrinsic ( $\delta\lambda$ ,  $\delta R_s$ ) and resonator-geometric ( $|\vec{j}|^2$ ) origins. The anisotropy in  $\delta\lambda$  and  $\delta R_s$  is introduced from the gap  $\Delta(\vec{k})$  which is encoded in  $b_\Theta$ . However, there can also be anisotropy in  $|\vec{j}|^2$  introduced by the possible asymmetries of the geometry of the resonator. To fully claim that measured PR anisotropy is equivalent to that of the gap function, it should be proven that the geometric anisotropy of the DR is negligible compared to the expected PR anisotropy for the case of a nodal gap superconductor. In the following discussions, we use a combination of simulation and experiment to prove the claim.

### 5.2.2 Estimation of systematic uncertainty in anisotropy of PR due to the effect of the resonator geometry

To validate the absence of geometric anisotropy, a current density  $\vec{j}$  on an isotropic sample (assumed perfect conductor) is simulated with HFSS. We want to examine the degree to which  $|\vec{j}_\Theta| = |\vec{j}(r_m, \Theta)|$  is a uniform function of angle  $\Theta$ , where  $r_m$  is the radius which gives the largest  $|\vec{j}(r, \Theta)|$  as a function of radius  $r$  (see the red circular region in Fig. 5.3(c)). In the simulation, Cu is used for the top and bottom plates, and a sapphire disk whose  $c$ -axis is aligned with the cylindrical axis of the disk is used for the dielectric material, with a diameter of 6.35 mm and a height of 3 mm. With these dimensions, the  $TE_{011}$  mode occurs at  $\sim 20$  GHz which is in a typical operating frequency for microwave transmission lines and devices. The lateral

dimension of the sample is  $9 \times 9 \text{ mm}^2$  to fully screen the field from the DR. As seen from Fig. 5.3(c),(d), the magnitude of the current density along the circle is uniform, and its angular dependence shows only a 2.8% anisotropy ratio, which is defined as  $(|\vec{j}_\Theta|_{max}^2 - |\vec{j}_\Theta|_{min}^2) / |\vec{j}_\Theta|_{min}^2$  around the circle. This small anisotropy occurs due to an effect of the coupling loops to the microwave field distribution which is small but breaks cylindrical symmetry. To further ensure the robustness of the uniformity of the current density, various kinds of possible geometric asymmetries are imposed on the resonator. As seen from Fig. 5.4, we consider displacements in one of the loop positions (shift in the x, z-direction), a tilt of the top plate, and a rectangular shaped sample with a  $45^\circ$  rotation. For each of these asymmetries, the simulations show the anisotropy ratio of 6.6%, 5.2%, 5.5%, and 7.3%, respectively. This result establishes the typical scale for geometric anisotropy in the presented dielectric resonator design in a simulational aspect. If one observes larger anisotropy in the PR image than this geometric anisotropy scale, the observed anisotropy in PR can be due to the gap nodal structure of the sample. In the following section, the degree of geometric anisotropy will be established again through experimental tests.

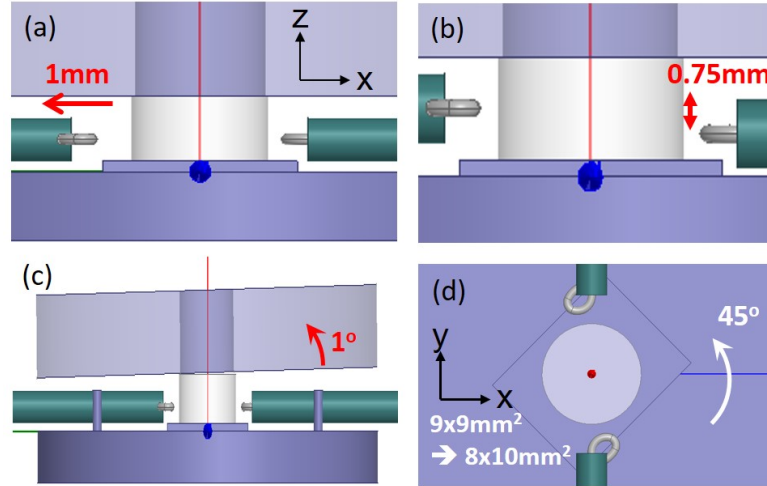


Fig. 5.4 HFSS simulated setup asymmetries to test the robustness of the uniformity of the angular dependence of the current density. (a) A shift in the loop position by 1 mm in the x-direction, (b) by 0.75 mm in the z-direction, (c) a tilted top plate by an angle of  $1^\circ$ , (d) rectangular shaped sample with  $45^\circ$  counterclockwise rotation.

## 5.3 Experimental results with dielectric resonator

### 5.3.1 LSM-PR from a conventional s-wave superconductor

The first validation required for the DR design to be utilized as a gap spectroscopy is to experimentally prove that it imposes only marginal geometric anisotropy to the measured PR. To do this, the PR is measured and imaged from a Nb sample whose superconducting gap has small ( $\lesssim 9\%$ ) [84] anisotropy. Since the anisotropy in  $b_\Theta(T)$  is only  $< 0.4\%$  for this case at the measurement temperature ( $\sim 8$  K), the anisotropy in the PR image from the Nb sample should arise mainly from the geometric anisotropy of the resonator.

The Nb thin film sample was grown on a silicon substrate by Ar sputtering from

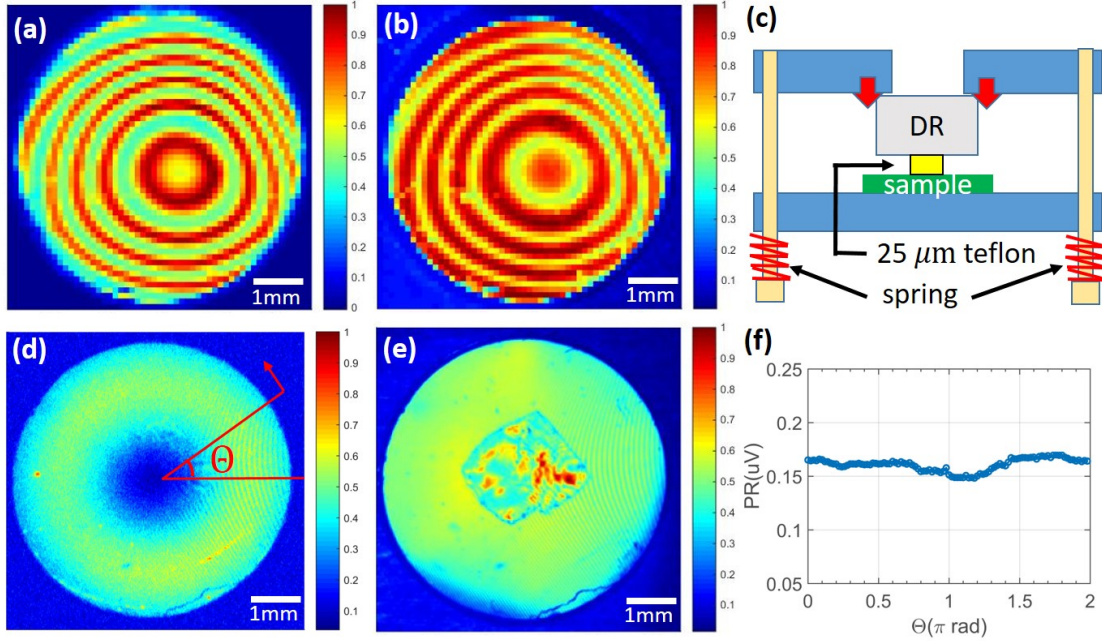


Fig. 5.5 (a) A PR image taken with a sapphire dielectric disk placed on a Nb thin film sample at temperature  $T = 8.02$  K, modulation frequency  $f_{mod} = 10$  kHz, input microwave power  $P_{in} = -10$  dBm, and  $TE_{011}$  resonance frequency  $f_0 \sim 20.57$  GHz. The image is dominated by the Newton-ring pattern. (b) Corresponding reflectivity image, which is also dominated by a Newton-ring pattern. Note that the bright pattern in the reflectivity corresponds to the dark pattern in PR and vice versa. (c) Schematic cross section diagram (not to scale) of the teflon insertion. A  $25 \mu\text{m}$ -thick teflon flake (yellow) is inserted between the sapphire disk and the sample, which makes the separation  $\sim 40$  times larger than the wavelength of the laser. (d) PR image taken after the teflon insertion and with a modulation frequency of 175 kHz. The Newton-ring pattern is greatly suppressed and the doughnut shape of the uniform circulating current distribution appears. (e) Corresponding reflectivity image showing the teflon and residual Newton rings. (f) Angular dependence of PR in (d) averaged over a wedge  $0.02\pi$  wide, showing  $\sim 8\%$  anisotropy.

a Nb target, and showed a thickness of 300 nm,  $T_c = 9.25$  K, and high  $RRR = 100$ . With this sample mounted and with the same sapphire disk and Cu top plate described above, a high  $Q (> 10^4)$  resonance is obtained at around 20.6 GHz and 4 K. Because an s-wave superconductor is predicted to have stronger PR near  $T_c$  (Fig. 3.2(c)) [53], PR is measured around 8 K, slightly below  $T_c$ .

Fig. 5.5(a) and (b) shows the image of PR and the corresponding reflectivity

with a laser modulation frequency of 10 kHz. The PR is mostly isotropic but there are two features which are not predicted by the HFSS simulation of the current distribution. One is the Newton-ring pattern and the other is the absence of doughnut-shaped PR pattern. Since PR is proportional to  $|\vec{j}|^2$ , it is expected to have a very weak signal at the center and a strong signal at the outer radius of the sample as  $|\vec{j}(x, y)|^2$  shows (Fig.5.3(c)). However, in Fig.5.5(a), the PR at the center is also strong.

For the first feature, this pattern originates from the interference of the laser light at the interface of the sapphire disk and the sample, creating Newton-rings [85]. The surface of the film and sapphire disk are smooth but not perfectly planar, creating a variable-thickness air-gap. Note that the reflectivity image has a ring pattern that is the exact complement to that of the PR image. This is expected since PR will be strong when the reflectivity is low (means more light is absorbed). Therefore, to eliminate this pattern, a 25  $\mu\text{m}$ -thick teflon flake is inserted and spring-loaded pressure is applied to fix it in place (see Fig. 5.5(c)). The role of the teflon flake placed at the center of the disk is to separate the disk from the sample by a large distance compared to the wavelength of the laser light so that it suppresses the optical interference, but it is a small distance compared to the microwave wavelength so that it does not disturb the field distribution. Note that the flake is added at a location with minimal microwave current in the  $\text{TE}_{011}$  mode. Also note that the spring-loaded pressure plays a crucial role to make rigid mechanical and thermal contact between components of the resonator (dielectric disk, sample, and top-bottom plates) while not breaking the sample.

For the second feature, the homogeneous magnitude of PR over the entire sam-

ple within the field of view of the aperture is due to the high thermal conductivity of the silicon substrate and the resulting low resolution of the PR image. Since the volume of the Nb film in this sample (300 nm thick) is small, the heat diffusion process is mainly governed by thermal properties of the silicon substrate [86]. The thermal conductivity of silicon  $\kappa_{Si}$  near  $T_c$  of the Nb is of order 100 W/mK. The thermal propagation length [87], which is the distance that heat travels within one period of the laser intensity modulation, is  $\Lambda_{Si} = \sqrt{D_{Si}/f_{mod}} = \sqrt{\kappa_{Si}/\rho c_{\rho} f_{mod}}$ , where  $D_{Si}$  is the thermal diffusivity,  $\rho$  is the mass density,  $c_{\rho}$  is the specific heat of the silicon, and  $f_{mod}$  is the modulation frequency of the laser. With  $f_{mod} = 10$  kHz we find  $\Lambda_{Si} \sim 2$  cm, which is larger than the field of view of the PR image. This large thermal propagation length of the substrate significantly reduces the resolution of the images and hence makes the magnitude of PR homogeneous throughout the sample regardless of the current distribution. To resolve this issue, a higher modulation frequency (175 kHz) is used to decrease the thermal propagation length ( $\Lambda_{Si} \sim 4.7$  mm) and enhance the resolution of the PR images. Note that using a high modulation frequency decreases the magnitude of the PR signal.<sup>3</sup> Therefore, an optimal modulation frequency is determined as the lowest modulation frequency that still clearly resolves the ring pattern of the circulating current as seen from Fig. 5.3(c). Under such conditions it should be possible to resolve the anisotropy of the PR as well.

With these two modifications adopted, PR is retaken while the other conditions are fixed. As a result, the Newton-ring pattern is effectively eliminated and the

---

<sup>3</sup>If one increases the modulation frequency of the laser intensity (decreases the modulation period), the area of the heated region within one modulation period decreases. This decreases the change in microwave transmission during one modulation period, which is the magnitude of PR.

doughnut-shaped PR is observed, as seen from Fig. 5.5(d), which confirms the simulated circulating uniform current. From this Newton-ring-free high-resolution image, the angular dependence of PR is examined and shows  $\sim 8\%$  of anisotropy (Fig. 5.5(f)). The result is consistent with the HFSS simulated geometric anisotropy in  $|\vec{j}|^2$  (5  $\sim$  7% each from several mechanisms) from Sec. 5.2.2. This means that if there is any systematic anisotropy in PR larger than the  $\leq 8\%$  background geometric anisotropy observed, it should originate from the anisotropy of the superconducting gap function, which establishes conditions for the validity of the LSM-DR method. Note that even though there exists PR from a point defect at the  $\Theta = \pi$  direction in Fig. 5.5(d), it does not overwhelm the PR from the defect-free area and also its contribution is marginal in the PR angular dependence plot in Fig. 5.5(f). This confirms the advantage of the new dielectric resonator method over the previous spiral resonator method, whose issue was illustrated in Fig. 5.1.

### 5.3.2 LSM-PR from a $d_{x^2-y^2}$ -wave superconductor

With these baseline results established, an unpatterned epitaxial and coherent  $c$ -axis oriented  $\text{YBa}_2\text{Cu}_3\text{O}_7$  (YBCO) thin film, a representative example unconventional superconductor with a 4-fold symmetric  $d_{x^2-y^2}$  gap, is examined with the dielectric resonator. The film thickness is 40 nm and it is  $c$ -axis normal on a sapphire substrate with  $\text{CeO}_2$  buffer layer, having a coherent structure in the  $a$ - $b$  plane. Note that this film is heavily twinned and these boundaries can host Andreev bound states (ABS) [56, 59, 62]. Note that twinning does not disrupt the 4-fold symmetry of the  $d_{x^2-y^2}$  gap. As

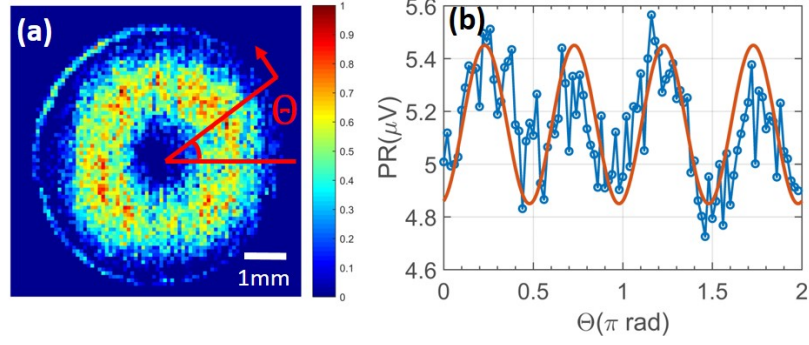


Fig. 5.6 (a) PR image from a 40 nm thick unpatterned YBCO thin film measured at  $T = 275$  mK,  $P_{in} = -5$  dBm,  $f_{mod} = 250$  kHz, and  $P_{laser} = 0.35$  mW. The definition of angle  $\Theta$  is shown in red. (b) Angular dependence of PR with a  $\sin^2 2\Theta$  fit as a guide to the eye. A weak 4-fold anisotropy is visible, consistent with a 4-fold symmetry of the  $d_{x^2-y^2}$  gap of YBCO.

long as the  $a$ ,  $b$ -directions are the same throughout the film, the 4-fold anisotropy will survive. Since the temperature dependence of the nonlinear Meissner coefficient  $b_\Theta$  of a nodal superconductor becomes large as  $T \rightarrow 0$  [53], the PR is measured at  $T = 275$  mK. A high modulation frequency  $f_{mod} = 250$  kHz is used to obtain sufficiently high resolution for the PR image. With 4 nodes in its gap function, YBCO is expected to show 4-fold symmetric PR. Indeed, as one can observe in Fig. 5.6(a) and (b), the PR image and its angular dependence show a 4-fold symmetric pattern with  $\sim 12.5\%$  anisotropy, making a clear contrast to the Nb case in Fig. 5.5(d) and (f). This result confirms the ability of the LSM-PR measurement with the dielectric resonator as a gap spectroscopy for unpatterned superconducting samples.

In the PR image, one can specifically relate a real space angle  $\Theta$  to a direction in  $k$ -space. Assuming the crystallographic directions ( $a$ ,  $b$ -axes) of the film follow those of the substrate, which is true for the coherent YBCO film grown on the sapphire substrate, one can deduce the crystallographic directions of the film from the cleaving

directions of the substrate. With the crystallographic directions known, the  $k_x$  and  $k_y$  directions in k-space and hence the gap nodal and anti-nodal directions can be determined. Then, the direction of the tangential current on the sample at a real space angle  $\Theta$  can be matched to those k-space directions.

Note that the PR along the gap nodal direction ( $\Theta = 0$  in Fig. 5.6) is smaller than that along the gap anti-nodal direction, contrary to the simple expectation from the bulk superconducting state of a  $d_{x^2-y^2}$  superconductor. This is due to the paramagnetic nonlinear Meissner effect which occurs due to the ABS at the twin boundary surfaces of the YBCO film [56]. This paramagnetic Meissner effect (PME) becomes dominant as  $T \rightarrow 0$  [59, 62]. The PME gives a 45-degree rotated anisotropy in  $b_\Theta(T)$  compared to that from the conventional (diamagnetic) NLME [47, 54]. This causes the PR image to rotate 45-degrees compared to the expectation from the conventional NLME, giving larger PR along the gap anti-nodal direction. The detailed explanation of the PR from PME can be found in Ref [47, 54] and Chap. 4.

Regarding the comparison with the previous spiral resonator in terms of the performance as a gap nodal spectroscopy, the 4-fold 12.5% anisotropy that the dielectric resonator shows from un-patterned YBCO sample is similar to the 13% anisotropy obtained from the patterned YBCO spiral resonator under the same measurement conditions. However, the PR from the spiral resonator shows  $> 5$  times larger magnitude of the signal and a clearer image since the sample is self-resonant and thus very sensitive to the thermal perturbation. Thus, if a sample can be prepared in a spiral form without any defects, the spiral resonator is still preferred. However, if a sample is prone to degradation or defects under the patterning procedure, the dielectric res-

onator method is superior.

PR contrast in the dielectric resonator method can be enhanced by utilizing several strategies. The first strategy is to increase the kinetic inductance fraction [88] of the sample in the resonator (which reveals anisotropy originating from the gap) over the geometric inductance of the entire resonator. This can be done by making the thickness of the film comparable or smaller than the magnetic penetration depth. A second strategy is to decrease the geometric factor [89] which is defined by the field energy stored in the volume of the dielectric disk over that in the surface of the sample. This can be achieved by decreasing the height of the disk or measuring PR in higher  $TE_{01n}$  modes with  $n > 1$ .

### 5.3.3 Future direction: LSM-PR with DR on single crystal samples

In most cases, a recipe for creating new superconducting materials is first discovered in the form of single crystals. Then, with some years of hard work by the sample growing experts, a recipe for the new material in the form of thin films can be found. A recipe for a fabricated thin film device comes at the final stage. Therefore, it would be good if one can extend the LSM-PR technique to single crystal samples so that the pairing symmetry of the new material can be revealed at the early stages of discovery. In this section, we list some of the preliminary results of the LSM-PR technique with DR on single crystal samples, and propose an alternative future design of the resonator which can study LSM-PR effectively on these single crystal samples.

The first examined single crystal was  $CeCoIn_5$  from Chris Ekberg (University of

Maryland). The material is one of the heavy Fermion superconductors and evidence for  $d_{x^2-y^2}$ -wave pairing symmetry already exists [10, 11, 90]. Thus, one expects an anisotropic, 4-fold symmetric PR image, and it would be an excellent example to see if the dielectric resonator design works for single crystals. However, an important issue has been identified. For most of the unconventional superconductors in single crystal form, including CeCoIn<sub>5</sub>, even the largest piece has a lateral size smaller than 3 mm, which is the diameter of the rutile disk, as seen in Fig. 5.7(a). In order for the induced circulating current density on the sample in the TE<sub>011</sub> mode to be azimuthally uniform, each lateral dimension of the crystal should be larger than 5 mm.<sup>4</sup> If the size of the crystal is smaller than that, the high magnetic field region will see the sharp edge of the crystal and the induced current on the sample will be enhanced around the edge. This edge effect dominates and distorts the PR image as seen in Fig. 5.7(b), so that determination of the pairing symmetry is hindered.

The next examined single crystal was KFe<sub>2</sub>As<sub>2</sub> from Yong Liu (AMES lab). Again, this material also has evidence for  $d_{x^2-y^2}$ -wave pairing symmetry from previous studies [91–93]. The issue with this material is that even the cleaved surface is not flat, and the polished surface degrades very quickly in air. Fig. 5.7(c) shows a polished surface of the cleaved KFe<sub>2</sub>As<sub>2</sub> crystal. The PR image from this rocky surface is dominated by topographic features as seen in Fig. 5.7(d), which again hinders determination of pairing symmetry from the image.

One proposal to circumvent these issues of the crystal size and the surface terrain

---

<sup>4</sup>Thickness can be arbitrary although 0.5 ~ 1 mm is preferred so that the sample is not too fragile and to not increase radiation loss from the opened side space of the dielectric resonator.

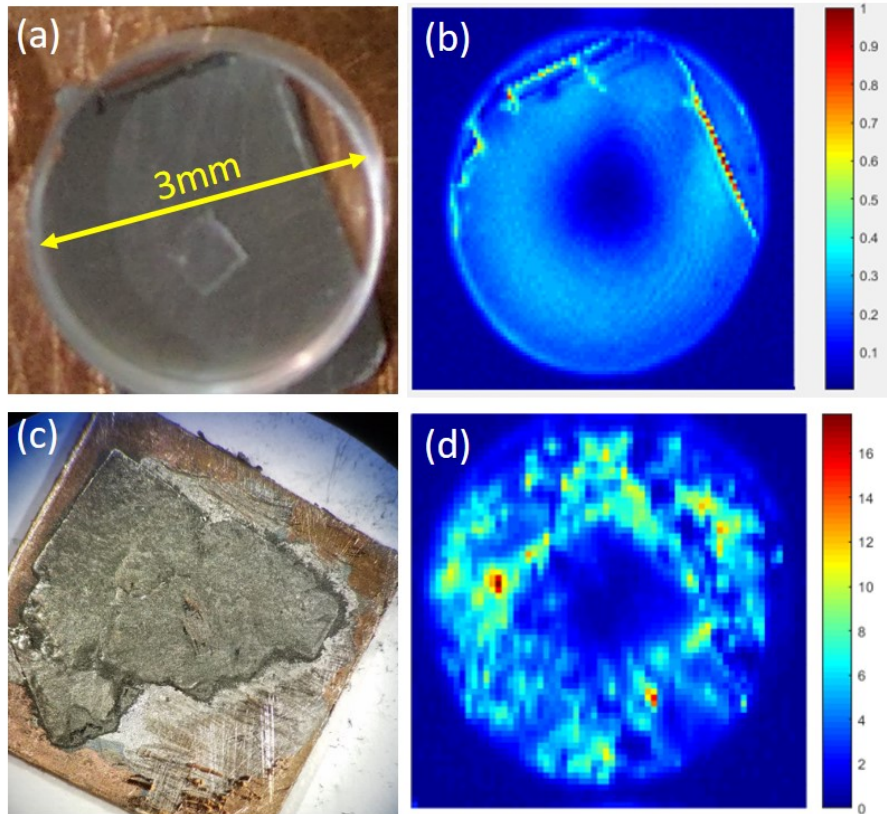


Fig. 5.7 (a) Photo of rutile disk (3 mm diameter) and the  $\text{CeCoIn}_5$  crystal under study. The object at the center is the Teflon flake used to minimize the Newton ring pattern in the PR image. As seen, the size of the crystal is smaller than the disk and edges are exposed. (b) PR image from  $\text{CeCoIn}_5$  at 460 mK. (c) Polished  $\text{KFe}_2\text{As}_2$  crystal (grey) soldered to  $1 \text{ mm}^2$  Cu sheet (brown). Topographic features still remain. (d) PR image from 200 mK of the  $\text{KFe}_2\text{As}_2$  crystal. Teflon flake insertion was not required here as the topographic features already prevented the formation of the Newton ring pattern. The color scales in (b) and (d) are in arbitrary units.

features is to give up on the spatial scanning of the laser beam. Instead, one can try to find a region somewhere on the surface of the sample that is free from terrain features and is away from the edges. This kind of clean region should be present at least in a certain area of the crystal. On the clean area, if one applies a linearly polarized microwave magnetic field by locating a microwave waveguide with a sub-mm-length linear slit above the clean area (Fig. 5.8)<sup>5</sup>, the microwave transmission can survey the response of the sample with polarized induced current. Experiments with a similar working principle but different purpose were already manifested [94, 95]. In this situation if one illuminates a laser beam on the clean area under the slit and then rotates the sample (which is sitting on a piezo-rotator), the polarization direction of the induced current will rotate with respect to the sample. Eventually, one will accumulate LSM-PR for the entire  $2\pi$  range of the current direction (momentum space), which will reveal the anisotropy of PR and the gap function.

---

<sup>5</sup>As long as it does not make the sample kinetic inductance fraction too small, the slit length can be sub-mm. A simulation should be carried to determine the slit length to check this point.

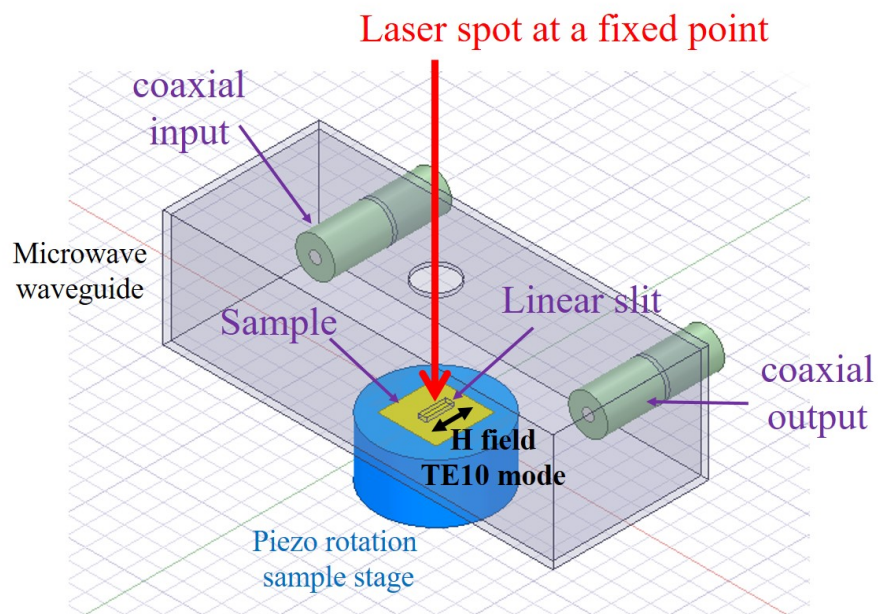


Fig. 5.8 The proposed waveguide setup for examining pairing symmetry of single crystal samples with LSM-PR. The waveguide has an aperture for the laser light to illuminate the sample, and has a linear slit to apply a linearly polarized magnetic field to a fixed position at the sample.

# CHAPTER 6

---

## Microwave Impedance Spectroscopy

---

- Recommended readings for this chapter: [10, 81, 90, 96–99]

This chapter begins the second part of this thesis. In this chapter, an introduction to the microwave surface impedance study of superconducting systems will be given. The introduction includes background theory, measurement and data processing procedures, a way to interpret the data, and cavity design. This information will be a preparation for the readers to understand the results and discussion of the example studies of topological superconductors in the following chapters (Chap. 7, 8).

### 6.1 Microwave complex conductivity

Conductivity is a quantity which describes the response of a physical system to a given electromagnetic field. For example, when a sample is subjected to an electric and magnetic field, it generates a current in response. The conductivity determines how much current the sample generates. In the local electrodynamics limit where

the penetration depth  $\lambda$  is greater than the BCS coherence length  $\xi_0$  (for the case of a superconductor) and skin depth  $\delta >$  mean free path  $l_{mfp}$  (for the case of normal metal),

$$\vec{j} = \sigma \vec{E}. \quad (6.1)$$

Here,  $\vec{j}$  is the current density,  $\sigma$  is conductivity, and  $\vec{E}$  is the electric field. In the case of direct current (DC) drive,  $\sigma$  is real. However, for the case of a finite frequency, alternating current (AC) drive, the system has both in-phase and out-of-phase response to the field. Therefore,  $\sigma$  becomes complex.

$$\vec{j} = \tilde{\sigma} \vec{E} = (\sigma_1 - i\sigma_2) \vec{E}. \quad (6.2)$$

Here, the real part ( $\sigma_1$ ) represents the in-phase response, the imaginary part ( $\sigma_2$ ) represents the 90° out-of-phase (quadrature) field response of the system, and the minus sign is a convention associated with the choice of time dependence  $e^{i\omega t}$ . In the following sections, I will introduce how one can model this finite frequency conductivity in the case of normal metals and superconductors.

### 6.1.1 Drude model of conductivity

For the case of a normal metal, the complex conductivity produced by free carriers can be described by the Drude model.

$$\tilde{\sigma} = \frac{ne^2}{m^*} \frac{\tau}{1 + i\omega\tau}. \quad (6.3)$$

Here,  $n$  is electron density of the system,  $e$  is an electric charge of the electron,  $m^*$  is the effective mass of the electrons in the energy bands that govern transport phenomena,  $\tau$  is scattering life time which represents the time interval between two scattering events that alter the electron momentum, and  $\omega$  is the angular frequency ( $2\pi f$ ) of the electromagnetic field applied to the system. The combination  $ne^2/m^*$  is often called the "oscillator strength" and is a common coefficient that appears in conductivity expressions.

An important figure which determines the nature of the response to the electromagnetic field is the dimensionless quantity  $\omega\tau$ . If  $\omega\tau \ll 1$ ,

$$\tilde{\sigma} \simeq \frac{ne^2\tau}{m^*}. \quad (6.4)$$

In this case the system is governed by a dominant in-phase response  $\sigma_1 \gg \sigma_2$ , and the system behaves essentially as a resistor. On the other hand, if  $\omega\tau \gg 1$ ,

$$\tilde{\sigma} \simeq i \frac{ne^2}{m^*\omega}. \quad (6.5)$$

In this case, the system is governed by a dominant out-of-phase response  $\sigma_1 \ll \sigma_2$ , and the system behaves essentially as an inductor. Therefore, for a given  $\tau$ , by controlling the measurement frequency  $\omega$  of the microwave experiment, one can in principle switch the character of the response for a normal metal, although it may require going to the THz or infrared frequency range.

### 6.1.2 Two fluid model

For the case of a superconductor at finite temperature, primarily due to thermal excitation there exists a mixture of normal electrons (normal fluid) with normal fluid fraction  $f_n$  and superconducting electrons (superfluid) with superfluid fraction  $f_s$ . The normal fluid, with finite  $\tau$ , gives both in and out-of-phase responses as described in the above section.

$$\tilde{\sigma}_n = \frac{ne^2}{m^*} \frac{f_n \tau}{1 + i\omega\tau}. \quad (6.6)$$

The superfluid, on the other hand, with infinite electron scattering life time  $\tau \rightarrow \infty$ , gives only an out-of-phase response:

$$\tilde{\sigma}_s = i \frac{f_s ne^2}{m^* \omega}. \quad (6.7)$$

Hence the total conductivity of the superconductor is given by,

$$\tilde{\sigma}(T, \omega) = \frac{ne^2}{m^*} \left( \frac{f_n(T)\tau(T)}{1 + i\omega\tau(T)} + i \frac{f_s(T)}{\omega} \right). \quad (6.8)$$

Note that  $f_s + f_n = 1$ , and this model, which is called the two fluid model [100], has successfully explained the temperature and frequency dependence of electrodynamic properties of superconductors. Note that in this model,  $f_n$  and  $f_s$  are temperature dependent but not frequency dependent quantities. However, if the photon energy of the probing electromagnetic signal ( $\hbar\omega$ ) becomes comparable to the energy required to break a Cooper pair into excited quasiparticles ( $2\Delta$ ), one needs to consider frequency

dependence of  $f_n$  and  $f_s$ , which complicates the analysis. Thus, it is a good habit to compare  $\hbar\omega$  and  $2\Delta$  before proceeding with a two-fluid analysis.

The real and imaginary parts of the complex conductivity take different roles in describing the field response of the superconductor. While  $\sigma_1$  describes the normal Ohmic transport behavior of the normal fluid,  $\sigma_2$  describes the screening of the field mainly due to the superfluid. The propagation constant  $\tilde{k}$  of the electromagnetic field inside a material with a propagation factor  $e^{i(\tilde{k}z + \omega t)}$  is [98, 101],

$$\tilde{k} = k + i\kappa = \sqrt{-i\mu\omega\sigma} = \sqrt{-i\mu\omega(\sigma_1 - i\sigma_2)}. \quad (6.9)$$

Here,  $\mu$  is magnetic permeability of the material, and  $\kappa$  is the decay constant of the field whose inverse is the screening length, which is the penetration depth  $\lambda$  for the case of a superconductor. In the superconducting state well below  $T_c$  and at a low frequency  $\hbar\omega \ll 2\Delta$  which satisfies the  $\sigma_1 \ll \sigma_2$  condition,

$$\kappa^2 = 1/\lambda^2(\omega, T) = \mu\omega\sigma_2(\omega, T). \quad (6.10)$$

From this relation, the magnetic penetration depth  $\lambda$  can be found.  $\lambda$  is an important piece of information not only for designing microwave devices for applications but also because its temperature dependence can help to reveal the pairing symmetry of the superconductor [15].

On top of the penetration depth information from  $\sigma_2$ , if one is able to measure frequency dependence of the complex conductivity  $\tilde{\sigma}(\omega)$  at each temperature, by fit-

ting the frequency dependent data with the two-fluid model expression (Eq. (6.8)) in terms of  $\omega$ , one can estimate the oscillator strength  $ne^2/m^*$ , quasiparticle scattering life time  $\tau$ , and normal fluid fraction  $f_n$ . If the frequency dependent data of  $\tilde{\sigma}(\omega, T)$  is not available but one has only the temperature dependence  $\tilde{\sigma}(T)$  from a single measurement frequency, one can still estimate  $\tau(T)$  and  $f_n(T)$  with the following trick.

From Eq. (6.8), the real and imaginary parts of the conductivity can be obtained as,

$$\sigma_1 = \frac{ne^2}{m^*} \frac{f_n \tau}{1 + \omega^2 \tau^2} \quad (6.11)$$

$$\sigma_2 = \frac{ne^2}{m^*} \frac{1 + \omega^2 \tau^2 - f_n}{\omega(1 + \omega^2 \tau^2)}. \quad (6.12)$$

If one divides Eq. (6.12) by Eq. (6.11), it yields a quadratic equation for  $\omega\tau$  in terms of the conductivity ratio  $\sigma_2/\sigma_1$  and normal fluid fraction  $f_n$ , with solution,

$$\omega\tau = 0.5 \left[ \frac{\sigma_2}{\sigma_1} f_n \pm \sqrt{\left(\frac{\sigma_2}{\sigma_1} f_n\right)^2 - 4(1 - f_n)} \right]. \quad (6.13)$$

To have real solutions for  $\tau$ ,  $f_n$  must satisfy the following condition,

$$f_n \geq \frac{2}{1 + \sqrt{1 + (\sigma_2/\sigma_1)^2}}, \quad (6.14)$$

from which one can estimate the minimum value of  $f_n(T)$  ( $\min f_n(T)$ ) with the measured data of  $\sigma_2$  and  $\sigma_1$ . With  $\min f_n(T)$  and Eq. (6.13), one can also estimate the scattering life time  $\tau(T)$ . Finally, by plugging the obtained  $\min f_n(T)$  and  $\tau(T)$  back

to Eq. (6.11), the oscillator strength  $ne^2/m^*$  can be estimated. Note that this two-fluid model assumes a homogeneous medium. For a inhomogeneous medium, one needs to consider a detailed current distribution in the medium. Therefore, the estimated values of  $f_n$ ,  $\tau$ , and  $ne^2/m^*$  from the simple two-fluid model above should only be taken as "effective" values in such case.

### 6.1.3 Connection between complex conductivity and surface impedance

The conductivity is a key piece of information governing the field response of a superconductor. How can one experimentally determine it? For the case of DC, the conductivity can be calculated once the resistance of the sample is experimentally measured. For the case of AC, microwave complex conductivity can be obtained by experimentally measuring the surface impedance  $Z_s = R_s + iX_s$  of the sample.  $R_s$  is the surface resistance which dictates microwave dissipation of the sample, and  $X_s$  is the surface reactance which describes the microwave inductance of the sample. In the same local limit as mentioned above,  $\tilde{\sigma}$  and  $Z_s$  have a simple relation,

$$Z_s = R_s + iX_s = \sqrt{\frac{i\mu\omega}{\tilde{\sigma}}}. \quad (6.15)$$

#### Surface impedance in various limits

In the low frequency and low temperature limit of the superconducting state ( $\sigma_1 \ll \sigma_2$ ),  $\sigma \simeq -i\sigma_2$  and the right hand side of Eq. (6.15) becomes pure imaginary. By comparing the imaginary part of the left and right hand sides of Eq. (6.15) before

taking the square,

$$iX_s \simeq \sqrt{\frac{i\mu\omega}{-i\sigma_2}} = i\sqrt{\frac{\mu\omega}{\sigma_2}},$$

and after taking the square of Eq. 6.15,

$$i2R_s X_s = i\text{Im}\left[\frac{i\mu\omega}{\sigma_1 - i\sigma_2}\right] = i\frac{\mu\omega\sigma_1}{\sigma_1^2 + \sigma_2^2} \simeq i\frac{\mu\omega\sigma_1}{\sigma_2^2},$$

one can arrive at (Yes! It is being very kind for the future student!),

$$R_s(\omega, T) = \frac{1}{2}\mu^2\omega^2\lambda^3(\omega, T)\sigma_1(\omega, T), \quad (6.16)$$

$$X_s(\omega, T) = \sqrt{\mu\omega/\sigma_2} = \mu\omega\lambda(\omega, T). \quad (6.17)$$

Hence, a measurement of the surface reactance  $X_s$  can also provide the penetration depth  $\lambda$ , while the surface resistance  $R_s$  provides information on  $\sigma_1(\omega, T)$ . This regime  $\sigma_1 \ll \sigma_2$  and the corresponding results for  $Z_s$  (Eq. (6.10, 6.16, 6.17)) hold for most of the topologically trivial superconductors at low temperature. However, for the case of an intrinsic topological superconductor with surface residual normal fluid, even in the superconducting state at low frequency and temperature, the  $\sigma_1 \ll \sigma_2$  regime does not hold anymore. The analysis of  $Z_s$  for intrinsic TSCs will be discussed in more detail in Chap. 8.

Now, back to the general case, if one raises the temperature high enough so that one moves into the normal state ( $T > T_c$ ) with large scattering rate ( $\omega\tau \ll 1$ ),

$\sigma_1 \gg \sigma_2$  so that

$$Z_s = R_s + iX_s \simeq \sqrt{\frac{i\mu\omega}{\sigma_1}} = \frac{1+i}{\sqrt{2}} \sqrt{\frac{\mu\omega}{\sigma_1}}, \quad (6.18)$$

and hence  $R_s = X_s$ . One may ask what the benefit of studying  $Z_s$  in this "Large scattering rate regime" ( $\omega\tau \ll 1$ ) is. In surface impedance experiments, while it is easy to measure the relative change in the surface reactance  $\Delta X_s(T) = X_s(T) - X_s(T_{ref})$ , it is very hard to directly measure the absolute value of  $X_s(T)$ . However, if one measures  $R_s$  in the large scattering rate regime, by equating  $R_s = X_s$ , one can obtain the absolute value of  $X_s$ . Then, by applying the measured relative change  $\Delta X_s(T)$ , one can finally obtain the absolute value of  $X_s(T)$  in the full temperature range down to the superconducting state. In the following sections, the experimental methods and procedures of the surface impedance  $Z_s$  measurement will be discussed.

## 6.2 Microwave surface impedance measurement

### 6.2.1 Transmission measurement setup and procedure

The surface impedance  $Z_s$  of a superconducting sample can be obtained from both resonant techniques and non-resonant techniques. In this thesis, we will discuss only the resonant techniques. Readers who are interested in the non-resonant techniques can refer to Ref. [102, 103]. For the resonant techniques, one can obtain  $Z_s$  from the resonance properties (resonant frequency  $f_0$  and quality factor  $Q$ ) of a microwave transmission resonance that involves the sample of interest. Therefore, a

transmission measurement should be performed to obtain  $Z_s$  of the sample.

Since the LSM-PR measurement introduced in Chap. 2 is nothing but a microwave transmission measurement with a laser perturbation, the same setup can be used for  $Z_s$  measurement by just turning off the laser. One change for convenience is that the input and output microwave signals are now generated and received by the Keysight vector network analyzer (VNA) N5242A (Fig. 6.1), instead of the signal generator and the microwave detector (Fig. 2.3(a)). The VNA calculates a voltage ratio of the signal at its input and output port to obtain the microwave transmission scattering parameter  $S_{21}^{tot}$ .<sup>1</sup> The generated input signal goes into the microwave transmission line (blue lines in Fig. 6.1) of the dilution fridge and reaches down to the resonator attached to the mixing chamber plate (MXC). With no laser illumination and the optical windows closed, the typical base temperature at the resonator is  $\approx 30$  mK. The signal passed through the resonator comes back to the output port of the VNA. The details of various resonator designs will be discussed in Sec. 6.3

Since  $S_{21}^{tot}$  calculated by the VNA includes cable loss from the transmission line, one needs to subtract out this cable loss in order to obtain the scattering parameter purely from the resonator. For this correction, an additional transmission line measurement called a thru line measurement, which follows the same signal path but bypasses the resonator in a separate cooldown, is used. The measured transmission from this correction line is called thru- $S_{21}$  ( $S_{21}^{thru}$ ). By subtracting  $S_{21}^{thru}$  from  $S_{21}^{tot}$ , one

---

<sup>1</sup>Note that all the scattering parameters are complex functions of frequency.

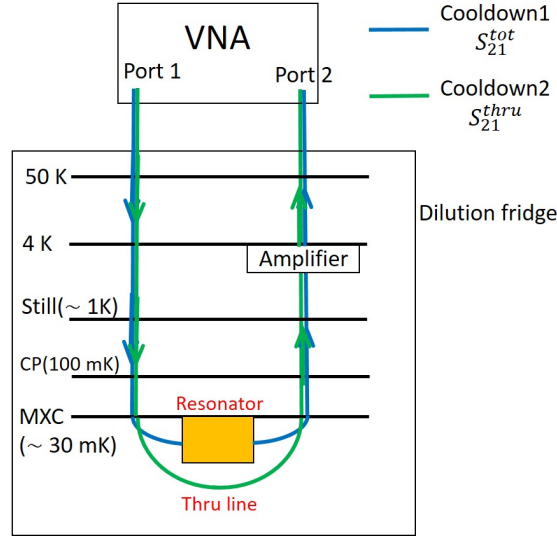


Fig. 6.1 Schematic view of the signal path of the microwave transmission measurement  $S_{21}^{tot}$  (blue) that includes the resonator, and the signal path of the thru line transmission measurement  $S_{21}^{thru}$  (green) that shares the same signal path except that it bypasses the resonator at a separate cooldown. The thru line measurement  $S_{21}^{thru}$  gives a measure of the cable loss.

can estimate the resonator transmission  $S_{21}^{res}$ ,

$$S_{21}^{res} = S_{21}^{tot} - S_{21}^{thru}. \quad (6.19)$$

With the above procedure for finding  $S_{21}^{res}$ , broadband transmission (0.1 ~ 20 GHz) is first measured to locate the resonant peaks.<sup>2</sup> For each located peak, a narrow band measurement is done to precisely resolve the sharp  $S_{21}^{res}(f)$  near the peak of each resonance (Fig. 6.2(a)). This peak  $S_{21}(f)$  measurement is conducted with various input microwave powers  $P_{in}$ . In principle, higher  $P_{in}$  is preferred since it helps to enhance the signal-to-noise ratio of the  $S_{21}$  measurement. However, if one increases

<sup>2</sup>One may be concerned about the possible presence of broadband noise coming down the cable to the resonator. However, the resonator itself behaves as a narrow-band filter, inducing a large field intensity on the sample surface only at the resonant frequencies. Therefore, the effect of broadband noise can be ignored.

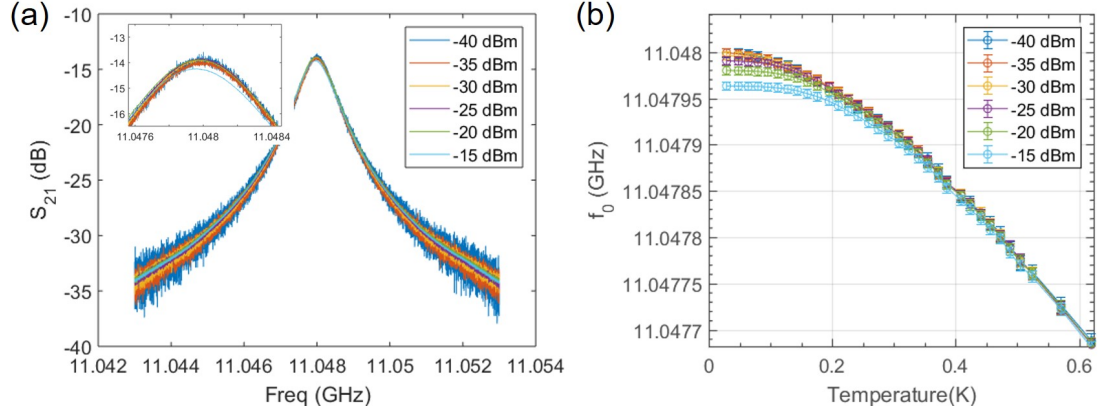


Fig. 6.2 (a) Typical  $S_{21}$  measurement near a resonance peak. Inset shows the effect on  $S_{21}(f)$  with variation of  $P_{in}$ . Data at  $P_{in} = -15$  dBm (skyblue) shows a suppression of the peak due to the microwave heating of the sample. (b) Temperature dependence of the resonant frequency  $f_0(T)$  for various values of  $P_{in}$ . The dependence on  $P_{in}$  saturates below -30 dBm.

$P_{in}$  too much, the input signal induces sample heating which distorts the peak  $S_{21}(f)$  as seen in the inset of Fig. 6.2(a) (distortion starts at  $P_{in} = -15$  dBm).<sup>3</sup> The effect of sample heating at high  $P_{in}$  can also be seen in the temperature dependence of the resonant frequency  $f_0(T)$  (Fig. 6.2(b)). Therefore, one needs to find a sweetspot for  $P_{in}$ ; utilize the largest  $P_{in}$  without affecting  $S_{21}(f)$  and  $f_0(T)$ . For example, in Fig. 6.2(b), the  $f_0(T)$  curve depends on  $P_{in}$  at high power but the dependence is independent of power below  $-30$  dBm. This means  $S_{21}(f)$  is free from the effect of microwave heating or nonequilibrium quasiparticles. In this case, using  $P_{in} \sim -30$  dBm would be an optimal choice.

<sup>3</sup>dB is a logarithmic ratio. When it is converted from the linear ratio (lin),  $\text{dB} = 10\log_{10}(\text{lin})$ . dBm is a unit of power in logarithmic ratio widely used in the microwave community. 0 dBm corresponds to 1 mW and -20 dBm corresponds to 0.01 mW, for example.

## 6.2.2 Determination of resonance properties $f_0$ and $Q$

With the measured  $S_{21}(f)$  curve, one can characterize the resonance properties. There are the resonant frequency  $f_0$ , which is related to the reactance of the system ( $f_0 \sim 1/\sqrt{LC}$  where  $L$  is the inductance and  $C$  is the capacitance of the system), and the quality factor  $Q$  which is related to the microwave dissipation  $P_{diss}$  in the system ( $1/Q \sim P_{diss}$ ). The characterization of  $f_0$  and  $Q$  can be done by fitting the  $S_{21}(f)$  curve near the resonance in two different ways. One method is Lorentzian fitting [96] which fits the magnitude of  $S_{21}(f)$  only with the following model,

$$|S_{21}(f)| = a_1 + a_2 f + \frac{|S_{21}^{max}| + a_3 f}{\sqrt{1 + 4Q_L^2 \left(\frac{f}{f_0} - 1\right)^2}}. \quad (6.20)$$

Here,  $a_1$ ,  $a_2$ , and  $a_3$  are coefficients which account for background frequency dependence of  $S_{21}(f)$ ,  $|S_{21}^{max}|$  is the magnitude of the peak  $S_{21}$  without the background, and  $Q_L$  is a "loaded" quality factor. The other way of fitting is to use the "Phase versus frequency fit" [96] which models the phase  $\phi$  of the complex  $S_{21}(f) = |S_{21}(f)|e^{i\phi(f)}$  with,

$$\phi(f) = \phi_0 + 2 \tan^{-1} \left[ 2Q_L \left( 1 - \frac{f}{f_0} \right) \right], \quad (6.21)$$

where  $\phi_0$  is a phase offset. Each method has its own advantages. Lorentzian fitting is known to perform better when the  $S_{21}(f)$  data is noisy. Phase versus frequency fitting performs better when the noise is small [96] and only requires half of the fitting parameters (3) compared to the Lorentzian fitting (6).

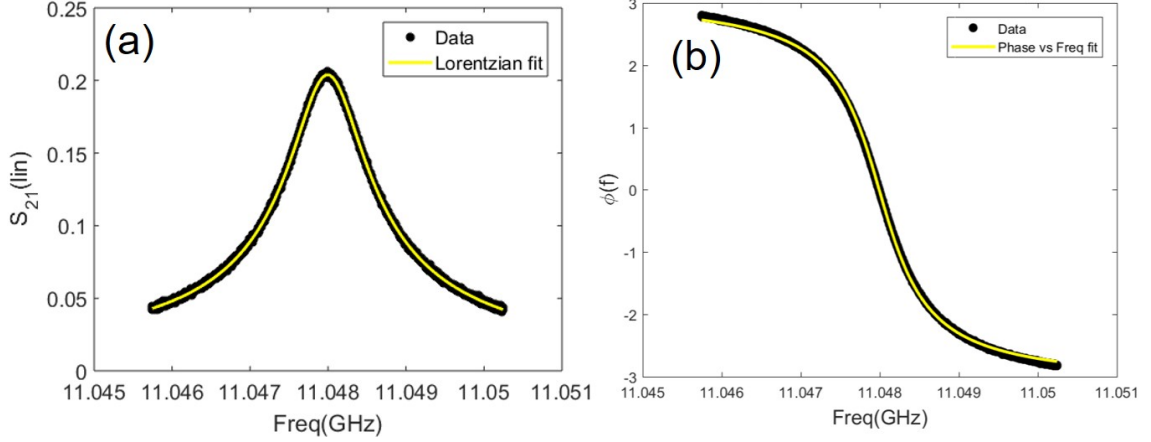


Fig. 6.3 (a) Example plot of  $|S_{21}(f)|$  data in linear scale (black) near the peak and corresponding Lorentzian fit curve (yellow). The fitting results in  $a_1 = 0$ ,  $a_2 = 2.71 \times 10^{-14}$  s,  $a_3 = -1.75 \times 10^{-13}$  s,  $|S_{21}^{max}| = 0.206$ ,  $f_0 = 11.048$  GHz, and  $Q_L = 11520$ . (b) Phase  $\phi(f)$  of the same  $|S_{21}(f)|$  data (black) and Phase versus frequency fit curve (yellow). The fitting results in  $\phi_0 = -0.0153$ ,  $f_0 = 11.048$  GHz, and  $Q_L = 12122$ .

Ideally, the quality factor  $1/Q$  should describe the dissipation from the resonator itself. However, to excite and pick up the microwave signal, the resonator should be coupled to the external world through excitation/pick-up loops. This coupling causes some portion of the energy in the resonator to leak out to the external world, adding an additional source of dissipation which is described by  $1/Q_c$  where  $Q_c$  is called the coupling  $Q$ . The  $Q$  arising purely from losses within the resonator is called the unloaded  $Q$  ( $Q_u$ ). The  $Q$  factor obtained from fitting the raw  $S_{21}$  data above is called the loaded  $Q$  ( $Q_L$ ) because it describes the dissipation from both the resonator itself  $1/Q_u$  and the coupling  $1/Q_c$ ,

$$1/Q_L = 1/Q_u + 1/Q_c. \quad (6.22)$$

To obtain information on the dissipation purely from the resonator, one needs to know

$Q_u$  which removes the effect of coupling. In the case of equal coupling from the input and output side,  $Q_u$  can be calculated as [104, 105],

$$Q_u = \frac{Q_L}{1 - |S_{21}(f_0)|}. \quad (6.23)$$

To obtain the dissipated microwave power from the sample  $P_{diss}^s$ , which is related to the resistance  $R_s$  of the sample, one needs to further subtract the dissipated power from the background components of the resonator. The main sources of the background dissipation of the resonator are Ohmic dissipation from the metallic enclosure  $P_{diss}^{enc}$  of the resonator, dielectric loss from the dielectrics  $P_{diss}^{diel}$ , and radiation loss from any openings of the resonator  $P_{diss}^{rad}$ . Therefore the unloaded Q can be written as,

$$P_{diss}^{tot} = P_{diss}^s + P_{diss}^{enc} + P_{diss}^{diel} + P_{diss}^{rad}, \quad (6.24)$$

$$\frac{1}{Q_u} = \frac{1}{Q_s} + \frac{1}{Q_{enc}} + \frac{1}{Q_{diel}} + \frac{1}{Q_{rad}}. \quad (6.25)$$

The detailed estimation and subtraction of  $P_{diss}$  from each background component varies depending on the resonator design, so it will be discussed further in Sec. 6.3. Once the subtraction is done, it leaves only the sample contribution to the quality factor  $Q_s$ .

On the other hand, extracting the absolute value of the sample contribution to the resonant frequency  $f_0$  is not a simple task [81]. In contrast to the case of the resistance and dissipated power, contributions to the reactance from each component of the resonator do not simply add up linearly. Instead of the absolute value of the reso-

nant frequency, a relative temperature dependence  $\Delta f_0(T) = f_0(T) - f_0(T_{ref})$ <sup>4</sup> can be studied much more easily since the change in the inductive response is dominated by the superconducting sample. The background components of the resonator typically have very weak temperature dependence on their material properties in the low temperature limit below 10 K, whereas most of the superconducting samples undergo a large change in their electromagnetic properties in that temperature range. The conversion of  $Q_s(T)$  and  $\Delta f_0(T)$  to  $R_s(T)$  and  $X_s(T)$  will be discussed in the following Sec. 6.2.3.

### 6.2.2.1 Error bar determination

Ideally, the error bars of the resonance properties ( $f_0$  and  $Q_L$ ) should be determined by repeating  $S_{21}(f)$  measurement under the same conditions (temperature and  $P_{in}$ ) and in large number ( $> 30$ ). Once the distribution of  $f_0$  and  $Q_L$  is obtained from the repeated  $S_{21}(f)$  dataset, the error bar of  $f_0$ ,  $Q_L$  can be determined as the standard deviation of the  $f_0$ ,  $Q_L$  distribution. However, performing this procedure for all temperatures and  $P_{in}$  points takes an enormous amount of time.

Instead, the error bar can be also determined by a deviation of  $f_0$  and  $Q_L$  from the estimated values which increases the root-mean-square error  $\sigma_{RMS}$  of the fit by 5%. The main source of the error bar of  $f_0$  and  $Q_L$  is the noise in the  $S_{21}(f)$  data. If the signal-to-noise ratio of  $S_{21}$  is large (small) which makes the  $S_{21}(f)$  curve well- (poorly-) defined,  $f_0$  and  $Q_L$  can have a narrower (wider) range of values while giving

---

<sup>4</sup> $T_{ref}$  is a reference temperature and usually set to the base temperature of the measurement.

fits with similar values of  $\sigma_{RMS}$ . Once the error bar of  $f_0$  and  $Q_L$  are determined, I utilize the standard error propagation methods from the relation between the resonance properties and extracted quantities of interest ( $Z_s$ ,  $\lambda$ , etc.), so that the error bar for the extracted quantities can also be determined.

### 6.2.3 Converting resonance properties ( $f_0$ and $Q$ ) into surface impedance ( $Z_s$ )

Once  $\Delta f_0(T)$  and  $Q_s(T)$  are obtained, the surface impedance  $Z_s = R_s + iX_s$  of the sample can be determined as [89],

$$R_s(T) = G_{geo}/Q_s(T) \quad (6.26)$$

$$\Delta X_s(T) = -2G_{geo} \frac{\Delta f_0(T)}{f_0}. \quad (6.27)$$

$$G_{geo} = \frac{\omega\mu_0 \int_V dV |H(x, y, z)|^2}{\int_S dS |H(x, y)|^2}. \quad (6.28)$$

Here,  $\int_V dV$  represents the integration over the volume of the resonator, and  $\int_S dS$  represents the integration over the surface of the sample.  $G_{geo}$  is the sample geometric factor which can be calculated either analytically using the field solution inside the resonator for each resonant mode (if the solution is available), or experimentally by comparing the measured  $R_s$  from Eq. (6.26) with calculated  $R_s = \sqrt{\mu\omega\rho_{trans}}/2$  from transport resistivity  $\rho_{trans}$ . Note that this calculation is valid in the  $\omega\tau \ll 1$  limit in the normal state of the sample. Ramping the temperature to reach this large scattering rate regime helps to find not only  $G_{geo}$  but also the absolute value of  $X_s(T)$ . When the

$\omega\tau \ll 1$  regime is reached, the complex conductivity  $\tilde{\sigma}$  only has a real part, resulting in  $R_s = X_s = \Delta X_s(T) + X_{s0}$  (as already discussed in Eq. 6.18). By comparison of  $R_s$  and  $\Delta X_s$ , the offset in the sample reactance  $X_{s0}$  can be found, which yields the absolute value of  $X_s(T)$ . With the absolute values of  $R_s(T)$  and  $X_s(T)$  determined, one can calculate the microwave complex conductivity  $\tilde{\sigma}(T)$  whose real and imaginary parts provide useful information about the normal fluid and superfluid response of a superconductor.

One important question here is, what is the unambiguous experimental signature that one has achieved the  $\omega\tau \ll 1$  regime? In this regime,  $R_s(T) = X_s(T)$  so their temperature derivative  $dR_s/dT$ ,  $dX_s/dT$  should also be the same above the temperature  $T_{ls}$  where the large scattering rate  $\omega\tau \ll 1$  regime is achieved. Therefore, by translating the  $\Delta X_s(T)$  curve (note that  $dX_s/dT = d(\Delta X_s)/dT$ ) and finding a temperature regime above which  $dR_s/dT = d(\Delta X_s)/dT$  is satisfied,  $T_{ls}$  can be identified. Note that the relative magnitude of the temperature derivative of  $R_s$  and  $X_s$  has  $G_{geo}$  as a common factor, thus the estimated value of  $G_{geo}$  does not affect this comparison test.

#### 6.2.4 Nonlocal limit

In Sec. 6.1.3, the simple relation between  $\tilde{\sigma}$  and  $Z_s$  (Eq. (6.15)) is discussed in the local limit ( $\lambda > \xi_0$  and  $\delta > l_{mfp}$ ). While the local limit holds for most of the unconventional superconductors (especially for type II), it would be good to mention how the relation changes in the nonlocal limit. In the extreme nonlocal limit ( $\omega\tau \gg 1$

and  $l_{mfp} \gg \lambda$ ),  $Z_s$  approaches to  $Z_s^{nonlocal}$  which is given by [106],

$$Z_s^{nonlocal} = 0.289\mu\omega\lambda_L(1 + i\sqrt{3})\left(\frac{v_F}{\omega\lambda_L}\right)^{1/3}, \quad (6.29)$$

where  $\lambda_L = \sqrt{m^*/\mu ne^2}$  is the London penetration depth. Nonlocal effects also influence the temperature dependence of the penetration depth. Readers who are interested in the nonlocal effect on the temperature dependence of the penetration depth  $\lambda(T)$  can refer to Ref. [15].

## 6.3 Types of resonators

In this section, various types of dielectric resonators (DR) which host microwave transmission resonances for surface impedance measurement will be introduced.

### 6.3.1 Disk Dielectric resonator

The disk shape dielectric resonator (DR) is our first generation microwave resonator for  $Z_s$  measurement which allows simultaneous LSM-PR measurement. As introduced in Fig. 5.2, the details of the resonator dimensions, field distributions, mode frequencies have already been introduced in Sec. 5.2.1. Only the detailed aspects for surface impedance measurement, which have not introduced in Sec. 5.2.1, will be discussed here.

The geometric factor of the disk DR can be calculated from its definition (Eq. (6.28)), while the analytical field solution in the resonant modes was obtained by B. W. Hakki and P. D. Coleman [76]. For the rutile disk resonator with a diameter of 3 mm, height of 2mm, and at its fundamental mode ( $TE_{011}$ )  $f_0 \approx 10$  GHz, and a sample on one side of the disk, one finds that  $G_{geo} \approx 225\Omega$ . For the sapphire disk resonator with a diameter of 6.35 mm, height of 3mm, and at its fundamental mode ( $TE_{011}$ )  $f_0 \approx 20$  GHz, one finds that  $G_{geo} \approx 391\Omega$ . The calculated  $G_{geo}$  directly connects the measured temperature dependence of the resonant frequency  $\Delta f_0(T)$  data to the that of the surface reactance  $\Delta X_s(T)$  (Eq. 6.27). In the  $\sigma_1 \ll \sigma_2$  limit which holds for most of the superconductors (without residual normal fluid) at  $T < 0.3T_c$ ,  $\Delta X_s(T)$  can be converted directly to the temperature dependence of the penetration depth  $\Delta\lambda(T)$  (Eq. 6.17). In this manner, the disk DR is employed to study  $\Delta\lambda(T)$  of thin-film superconducting samples (Chap. 7)

Regarding the surface resistance  $R_s$  of a sample in the disk DR, the examination of the dissipation ( $1/Q$ ) from sources other than the sample can be done as follows. First, the radiation loss in the disk DR is marginal since the cutoff frequency of wave propagation through the aperture is 58.6 GHz for the rutile and 29.3 GHz for the sapphire disk DR. These cutoffs are much higher than the measurement frequencies of 11 GHz (rutile DR) and 20 GHz (sapphire DR), and hence the radiation field cannot propagate. Also, the dielectric loss should be marginal too since the loss tangent  $\tan \delta = 1/Q_{diel}$  is  $\sim 10^{-8}$  for both rutile and sapphire below 10 K [78]. Finally, in terms of Ohmic dissipation from the enclosure, the top plate is a niobium plate which was annealed to 800 °C for 3 hours in a high vacuum at Jefferson Lab [107]. This is the

same treatment which has been applied to produce niobium cavities with low loss for the use in radio frequency particle accelerator cavities. The treatment typically yields an extremely low surface resistance of  $\sim 1 \text{ n}\Omega$  at 1.5 GHz and 2 K [107]. As  $R_s \sim \omega^2$  for conventional superconductors at low temperature ( $T < 0.3T_c$ ) (Eq. (6.16)), one expects  $R_s \sim 54 \text{ n}\Omega$  at 11 GHz ( $f_0$  of the rutile disk DR). If one assumes  $G_{geo}$  of the top plate to be on the same order compared to that of the bottom plate (the sample),  $1/Q_{\text{top plate}} \sim 1.38 \times 10^{-10}$ .

The unloaded quality factor  $1/Q_u$  of the disk DR at the base temperature with a fully gapped superconducting sample is typically on the order of  $10^{-5}$  (other nodal superconducting samples should have larger  $1/Q_u$ ). Considering this,  $1/Q_u \gg 1/Q_{diel}$ ,  $1/Q_{\text{top plate}}$ , and the cutoff frequency which is larger than the measurement frequency implies that the dissipation should dominantly originate from the bottom side of the disk (Fig. 6.5(a)), where the sample is screening the magnetic field. Therefore, for the case of the disk DR,  $1/Q_s = 1/Q_u - 1/Q_{diel} - 1/Q_{\text{top plate}} \approx 1/Q_s$ . Note that the size of the sample in the disk DR should be larger than the diameter of the disk (3 mm). Otherwise, some of the field will leak out and be dissipated by the exposed copper bottom plate. As seen from Fig. 6.4, the induced surface current density  $J$  on the top surface of the sample at distance  $r = 1.5 \text{ mm}$  away from the center axis of the disk is still strong ( $J(r = 1.5) \approx 0.4J_{max}$ ).<sup>5</sup> Only when  $r = 2.5 \text{ mm}$  or larger, the induced current density becomes small ( $J(r > 2.5) \lesssim 0.05J_{max}$ ). This calculation result imposes a lower bound of the sample size ( $\geq 5 \times 5 \text{ mm}^2$ ) for the disk DR to fully attribute the  $Q_s$  from the measurement to the surface resistance  $R_s$  of the sample. This

---

<sup>5</sup> $J_{max}$  is the maximum surface current density.

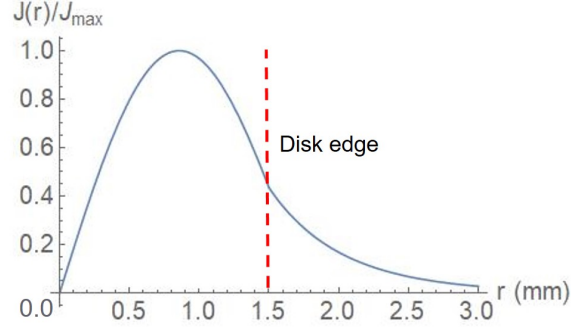


Fig. 6.4 Calculated surface current density  $J(r)$  on the bottom surface of the rutile disk DR (top surface of the sample) normalized by its maximum value. The coordinate  $r$  represents the radial distance from the center-axis of the disk. The calculation is based on the field solution given by Ref. [76]. The red dash line represents the radius of the rutile disk.

requirement is fulfilled by almost all of the thin film samples although it is not satisfied for the many of sub-mm size single crystals.

The advantage of the disk DR is that it provides a well-defined in-plane electromagnetic response, from the top surface of the sample. As long as the lateral dimension of the sample is larger than 5 mm, there is no magnetic field making detours around the edges and onto the out-of-plane facets of the sample. Therefore, the response one observes can be fully attributed to the plane adjacent to the bottom of the dielectric disk.

The disadvantage of the disk DR arises from the niobium top plate. A fully gapped  $s$ -wave superconductor starts to develop finite temperature dependence in its superfluid fraction  $f_s$  above  $\sim 0.25T_c$  [15] due to thermal excitation out of the ground state. Therefore, above  $T = 2.5$  K ( $0.25T_c$ ) the niobium top plate develops its own contribution to the frequency shift  $\Delta f_0(T)$  of the resonance. The top plate contribution is convoluted with the sample contribution, and this makes it hard to

determine  $\Delta f_0(T)$  purely from the sample. This was the main reason that the disk DR has been used to study mainly the low temperature behavior ( $T < 0.3T_c$ ) of  $\Delta\lambda(T)$  of the thin film samples whose  $T_c$  is below 8 K. Also, above the  $T_c$  of niobium, the top plate becomes too lossy so that  $Q_u$  becomes  $\sim 10^3$  or less. In such a low  $Q$  peak, our  $S_{21}(f)$  fitting methods cannot determine  $f_0$  and  $Q$  with the necessary accuracy. Hence, these niobium top plate properties limit the temperature window of the measurement. Thus, the absolute value of  $X_s(T)$  may not be found by applying the  $R_s = X_s$  trick (Sec. 6.2.3), if the  $\omega\tau \ll 1$  regime is achieved at temperatures above the  $T_c$  of niobium. Indeed, even for low- $T_c$  (1 ~ 3 K) unconventional superconductors including  $\text{Sr}_2\text{RuO}_4$  and  $\text{CeCoIn}_5$ , the  $\omega\tau \ll 1$  regime is achieved at around 20 K in the 2 ~ 15 GHz frequency range [90, 97]. Therefore, we want to have a capability of the temperature dependent  $Z_s$  measurement at least up to 20 K.

### 6.3.2 Hollow rutile cylindrical dielectric resonator

The hollow rutile cylinder dielectric resonator (hollow DR, Fig. 6.7(b)) [10, 81, 99] was introduced to address the disadvantages of the disk DR in examining small-sized single crystals, and in accurately measuring the absolute value of  $X_s$ , so that the full complex conductivity  $\tilde{\sigma}$  can be obtained. The two main changes are replacing the niobium top plate with a copper top plate, and replacing the solid rutile disk with a hollow rutile cylinder (Fig. 6.7(b)). Removing the niobium top plate enables determination of the absolute value of  $X_s$ . Due to the absence of significant background temperature dependence of  $f_0$  and  $Q$  from the niobium, we can measure

$R_s(T)$  and  $\Delta X_s(T)$  of the sample up to high temperature so that the absolute value of  $X_s(T)$  can be determined. The newly introduced copper top plate (or wall) shows only a small change ( $< 3\%$ ) in its electrical resistivity between 4 to 20 K [108], cutting down the background temperature dependence to a manageable level.

However, the drawback of using copper walls is that it introduces much more Ohmic dissipation compared to the niobium plate for the same amount of field exposure. To resolve this issue, one needs to decrease the amount of the field that is exposed to the copper walls. This can be done by introducing a space between the rutile cylinder (where most of the fields are concentrated) and the top and bottom walls. The spacing can be introduced by using a sapphire rod (Fig. 6.5(b)) as a mechanical supporting structure of the hollow rutile cylinder.

Once the minimal field exposure to the walls is achieved, introducing the hollow rutile cylinder instead of the solid disk allows one to study small-sized ( $\sim 1\text{ mm}^3$ ) crystals. The sample is inserted in the middle of the empty bore (Fig. 6.5(b)). Since the sample changes the field distribution inside the bore, and not the field distribution far away from the rutile cylinder, the amount of the field exposed to the copper walls remains low regardless of the sample size. This fact means that the measured resonant properties ( $f_0$  and  $Q$ ) from the hollow DR will be dominated by the field response of the sample rather than that of the walls regardless of the sample size. Therefore, samples with a variety of sizes can be tested.<sup>6</sup>

Figure. 6.5(b) shows our first generation hollow DR cavity design which includes

---

<sup>6</sup>Of course, one should be warned that if the crystal is too small (imagine the extreme case of a  $1\text{ }\mu\text{m}^3$  sized sample), the field response would be insensitive to the  $Z_s$  of the sample.

the above remedies. The hollow rutile cylinder has dimensions of outer diameter  $OD = 10$  mm, inner diameter  $ID = 3$  mm, and height  $H = 10$  mm. The cylinder is made by SurfaceNet GmbH, which is located in Germany. There are top and bottom sapphire disk spacers which separate the cavity walls and the DR. The top spacer has a dimension of  $D = 4$  mm and  $H = 2$  mm. The bottom spacer has a rod structure of  $D = 2.95$  mm,  $H = 5$  mm (which thermally anchors the sample to the rest of the parts) connected to the disk structure of  $D = 4$  mm and  $H = 2$  mm. The diameter of the top and bottom copper cavity walls are the same as the copper bottom plate of the disk DR.

The first generation hollow DR hosts more than 20 resonant modes in between 2 and 20 GHz. However, depending on the field distribution, not all of these modes involve the response of the sample. By comparison of the resonance properties ( $f_0, Q$ ) between when the sample is inserted and when it is absent, five modes which clearly involve the sample response were found at 2.71 (TE<sub>011</sub>), 4.58 (TE<sub>013</sub>), 5.73 (TE<sub>021</sub>), 6.89 (TE<sub>015</sub>), and 7.12 GHz (TE<sub>023</sub>).<sup>7</sup>

In the standard cavity perturbation theory, as the sample is inserted, the sample introduces an additional dissipation channel. Hence the quality factor  $Q$  of the resonator should decrease. However, among the 5 sample-response-dominant modes, the two low frequency modes (2.71 and 4.58 GHz modes) shows the opposite behavior where  $Q$  increases after the sample insertion. One possible scenario is that the exposed field to the top and bottom cavity walls with the 2 mm height sapphire spacers are

---

<sup>7</sup>In the notation "TE<sub>*mnl*</sub>", "TE" means "transverse electric field". The indices  $m, n, l$  represent the number of nodes of the field distribution in the azimuthal, radial, and height-directional coordinates of the cylinder. The identification of the modes is done by HFSS simulation, confirming previous results by X. Zhang [99] with a hollow DR of the same dimension and dielectric constant.

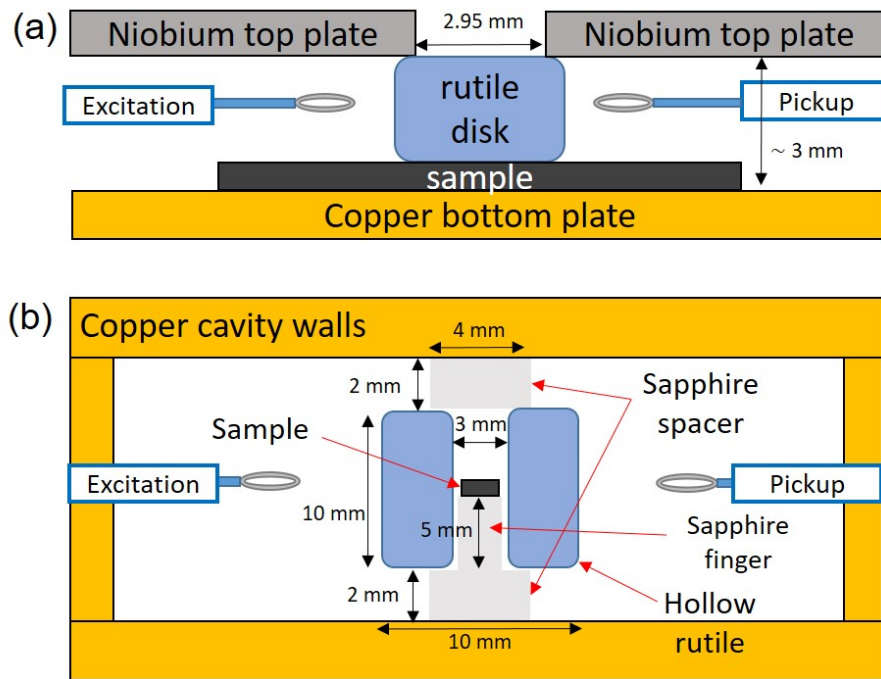


Fig. 6.5 (a) Schematic cross section diagram of the disk DR as a reminder (Fig. 5.2) and comparison to (b). Note that the large sample acts as a superconducting bottom plate for the DR. (b) Cross section view of the first generation hollow DR design. The bright grey parts are sapphire spacers which allow spacing between the lossy copper walls and the DR. The DR structure is a hollow cylinder with empty space of diameter = 3 mm. The sample is sitting in the middle as a perturbation to the field distribution generated by the hollow DR resonance. The drawing is not to scale.

actually not ignorable for those low frequency modes. In this case, if the redistributed field after the insertion of the sample results in lower amounts of exposed field on the copper walls, the Ohmic dissipation from the walls decreases and the Q of the modes increases. Indeed, the low frequency modes, due to their longer wavelength, have a greater proportion of the field outside of the rutile cylinder compared to the high frequency modes. This fact makes the above hypothesis more plausible. A quantitative check of the hypothesis, estimation on how far the copper walls should be separated from the rutile cylinder, and a remedy to fix this issue will be introduced in the next section (Sec. 6.3.3).

Another issue of the first generation hollow DR is the large temperature dependence of the rutile dielectric properties above 10 K. The hollow DR design adopts a large rutile cylinder so the contribution to the field stored energy from the rutile cylinder is much larger than in other DR designs. Therefore, the temperature dependence of the dielectric properties of the rutile significantly affects the DR resonant frequency  $f_0(T)$ , which is demonstrated in Fig. 6.6. First, dielectric crystals, such as rutile and sapphire, are known to contain paramagnetic impurities which act inductively in response to the external microwave field [109]. These paramagnetic impurities were reported to lead to a sharp upturn in  $f_0(T)$  as  $T \rightarrow 0$  [99, 109]. Indeed, this effect can be seen in the low temperature close-up of  $f_0(T)$  of the first generation hollow DR with no sample present (Fig. 6.6(a)). Second, the high dielectric constant of rutile, which enables resonant modes in a compact volume, undergoes a rapid decrease as the temperature is increased above 10 K [78, 109]. The rapid decrease in the dielectric constant  $\epsilon(T)$  yields a rapid increase in  $f_0(T) \sim 1/\sqrt{\epsilon(T)}$ , and this is clearly seen

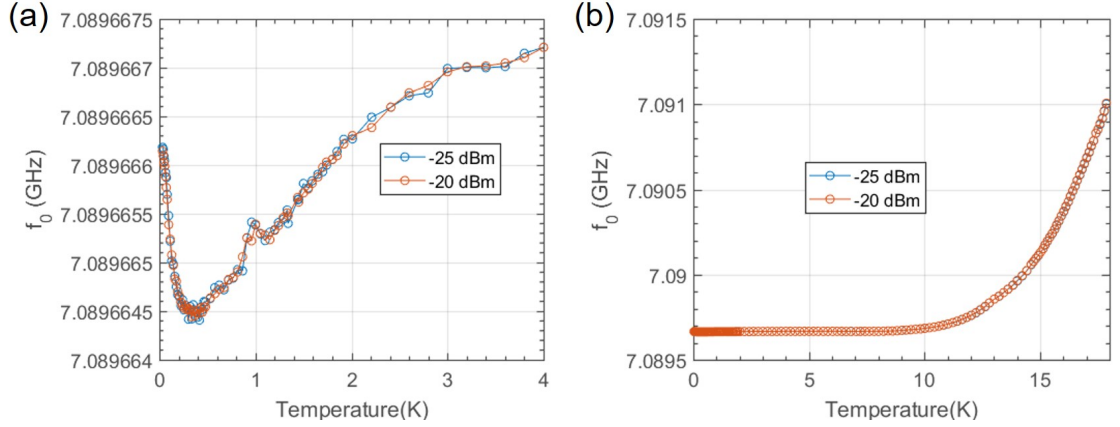


Fig. 6.6 (a) Low temperature resonant frequency  $f_0(T)$  study of the first generation hollow DR without a sample. The legend indicates the input microwave power  $P_{in}$  used in the measurement. (b) High temperature  $f_0(T)$  study of the hollow cylinder DR in the absence of a sample.

in the high temperature range data in the absence of a sample (Fig. 6.6(b)).

### 6.3.3 Upgrade on the hollow cylindrical dielectric resonator

As described above, the first generation hollow DR had two major issues. One is the substantial presence of fields on the cavity walls. The other is the highly temperature dependent dielectric and magnetic properties of rutile. To resolve the first issue, two remedies can be applied. One is to remove the disk sapphire spacers which unfortunately guide the fields to the top and the bottom walls due to their high ( $\approx 10$ ) dielectric constant. Instead, a very thin, wide sapphire wafer can suspend the hollow rutile in vacuum away from the walls (Fig. 6.7). The other remedy is to push back the walls away from the rutile. The first generation hollow DR has a cavity radius  $R_{cav} = 15$  mm and a height of the cavity  $H_{cav} = 14$  mm. An HFSS field simulation

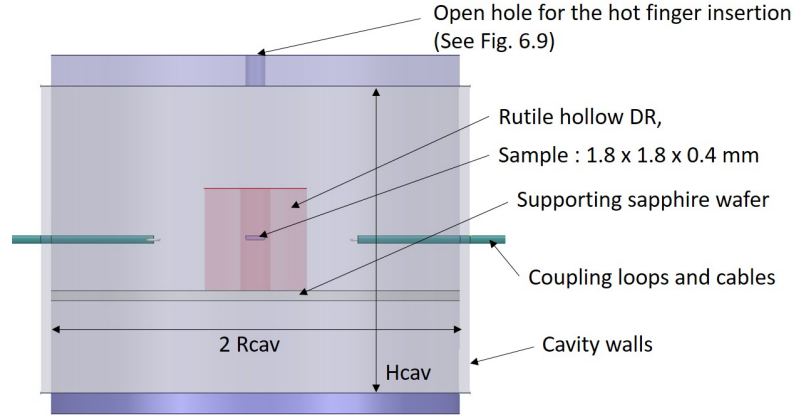


Fig. 6.7 HFSS simulation design of the second generation of the hollow DR (view from the side).

was performed to see how far the walls should be moved away to minimize the field reaching the walls. Figure 6.8(a),(c) shows an integration of the surface magnetic field  $\int dSH^2$  (here,  $\int dS$  represents surface integration) of the sample and the top, bottom, and side walls of the cavity. As expected, the increase in both  $H_{cav}$  and  $R_{cav}$  diminishes the surface field at the walls while increasing, or at least not decreasing, the surface field on the sample. For a more quantitative comparison, we defined the ratio of the integrated surface magnetic field in the walls compared to that in the samples,

$$M = \frac{\int_{walls} H^2 dS}{\int_{sample} H^2 dS}, \quad (6.30)$$

If this figure of merit  $M$  is small, it means the sample takes a larger portion while the wall takes a smaller portion of the field response. This ratio was on the order of 1 ( $M = 0.65$ ) for the first generation hollow DR, which means that a large field intensity is reaching the walls. However, as seen in Fig. 6.8(b),(d), the increase in  $H_{cav}$  (when

$R_{cav} = 15$  mm) rapidly decreases  $M$  more than a factor of 6 and almost saturates at  $H_{cav} = 30$  mm. Further, the increase in  $R_{cav}$  up to 20 mm (when  $H_{cav} = 30$  mm) smoothly decreases  $M$  more than a factor of 2. Note that  $R_{cav}$  larger than 20 mm was not simulated as it makes the cavity thermal and physical mass too large. In the end, an  $R_{cav} = 20$  mm,  $H_{cav} = 30$  mm cavity is predicted to have a walls-to-sample field energy ratio  $M = 0.048$  which is much smaller compared to the value  $M = 0.65$  of the original geometry. At the moment this thesis is being written, the new cavity design of  $R_{cav} = 20$  mm,  $H_{cav} = 30$  mm is being constructed and will be experimentally tested soon.

The second issue of the 1st generation hollow DR, which is the temperature dependence of the rutile dielectric properties, can be resolved by thermally disconnecting the sample temperature and the resonator (cavity walls + hollow DR) temperature. This can be done by a "hot finger" technique [110]. As seen in Fig. 6.9, the cavity and hollow rutile are thermally anchored to the cold plate of the fridge. This cold plate (CP) is thermally isolated from the mixing chamber plate (MXC), so that it can stay at its base temperature of 100 mK even though the temperature at the MXC changes. On the top wall of the cavity, a separate thermal stage is mechanically mounted through Vespel SP-1 rods. The thermal stage acts as a thermal reservoir for the sample and it is thermally connected to the MXC through copper braidings so that it can reach the base temperature of the MXC. The Vespel rods have a vanishingly small thermal conductivity at cryogenic temperature [111]. Considering the temperature dependent thermal conductivity of the Vespel, 3 Vespel rods with  $D = 0.125$  inch,  $H = 2$  inches will transmit  $90 \mu\text{W}$  of heat when the thermal reservoir is even at 20 K and the cold

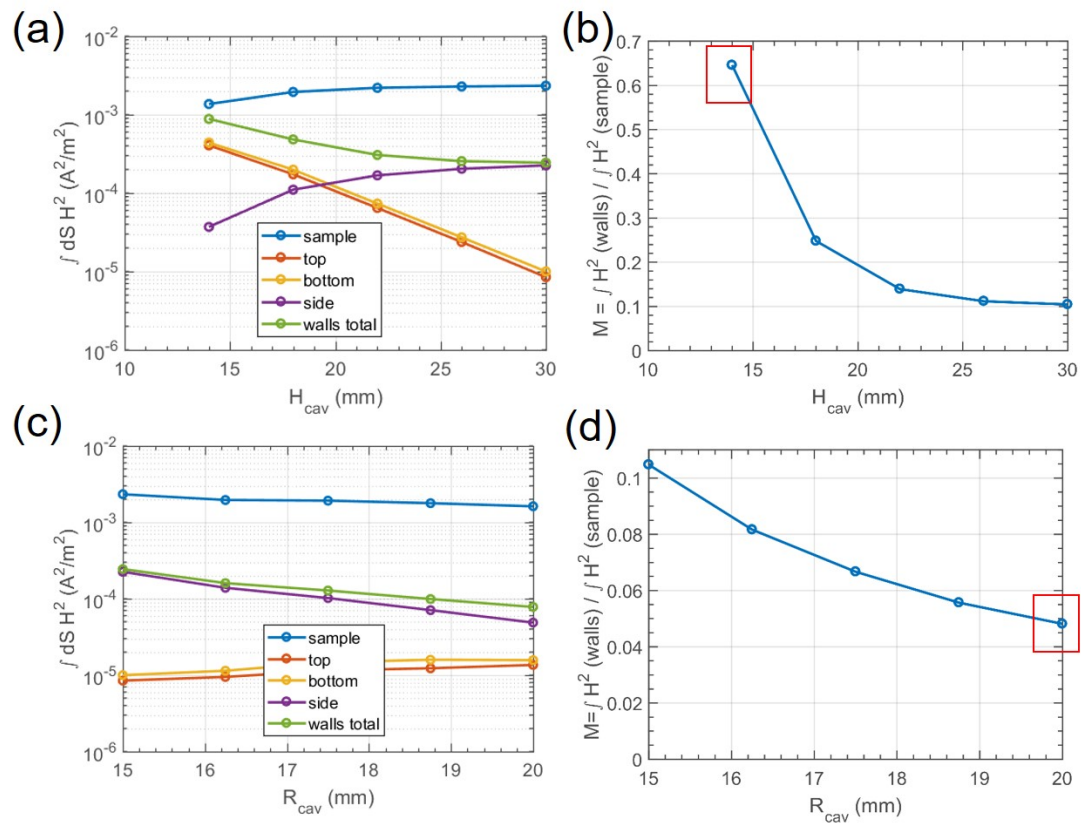


Fig. 6.8 Integrated surface magnetic field over the surface of each component of the resonator in terms of (a)  $H_{cav}$  variation and (c)  $R_{cav}$  variation. The walls-to-sample integrated surface field ratio  $M$  as a function of (b)  $H_{cav}$  (for  $R_{cav} = 15$  mm) and (d)  $R_{cav}$  (for  $H_{cav} = 30$  mm).

plate (CP) is at 100 mK. The cooling power of the CP at 100 mK is  $100 \mu\text{W}$ , so the heat should be handled by the CP

The thermal reservoir and the sample are connected by a non-magnetic 304 stainless steel (SS304) weak link.<sup>8</sup> The weak link is designed to provide cooling power to the sapphire hot finger and the sample so that they can reach the base temperature within a reasonable time frame. At the same time, the weak link design aims to provide modest thermal isolation so that MXC and the reservoir do not have too large a temperature increase when the sample and the finger are heated up for the  $f_0(T)$ ,  $Q(T)$  studies of the sample. Considering these requirements, the SS304 weak link dimensions are determined to be  $D = 0.125$  inch,  $H = 0.5$  inch, and thickness =  $0.006$  inch [112], transmitting 1 mW of heat when the sample and the finger are at 20 K and the reservoir is at 100 mK for example. Note that the MXC (where the reservoir is anchored) has a cooling power of 1 mW at 350 mK. Therefore, if one increases the sample temperature up to 20 K, it will increase the MXC temperature to  $\sim 350$  mK, and that only increases the CP temperature by 9 mK in our system due to a weak thermal connection between the CP and MXC.

The second generation hollow DR design which adopts the two modifications (large cavity, hot finger) is shown in Fig. 6.9. With this new design, two measurements are needed to determine the surface impedance  $Z_s$  of the sample. The first one is for the background dissipation measurement without the sample but with the hot finger carried to high temperature. The second one is for the actual sample property measurement with the sample inserted on the hot finger and the temperature of the

---

<sup>8</sup>This weak link design is adopted from the design of N. Murphy [112].

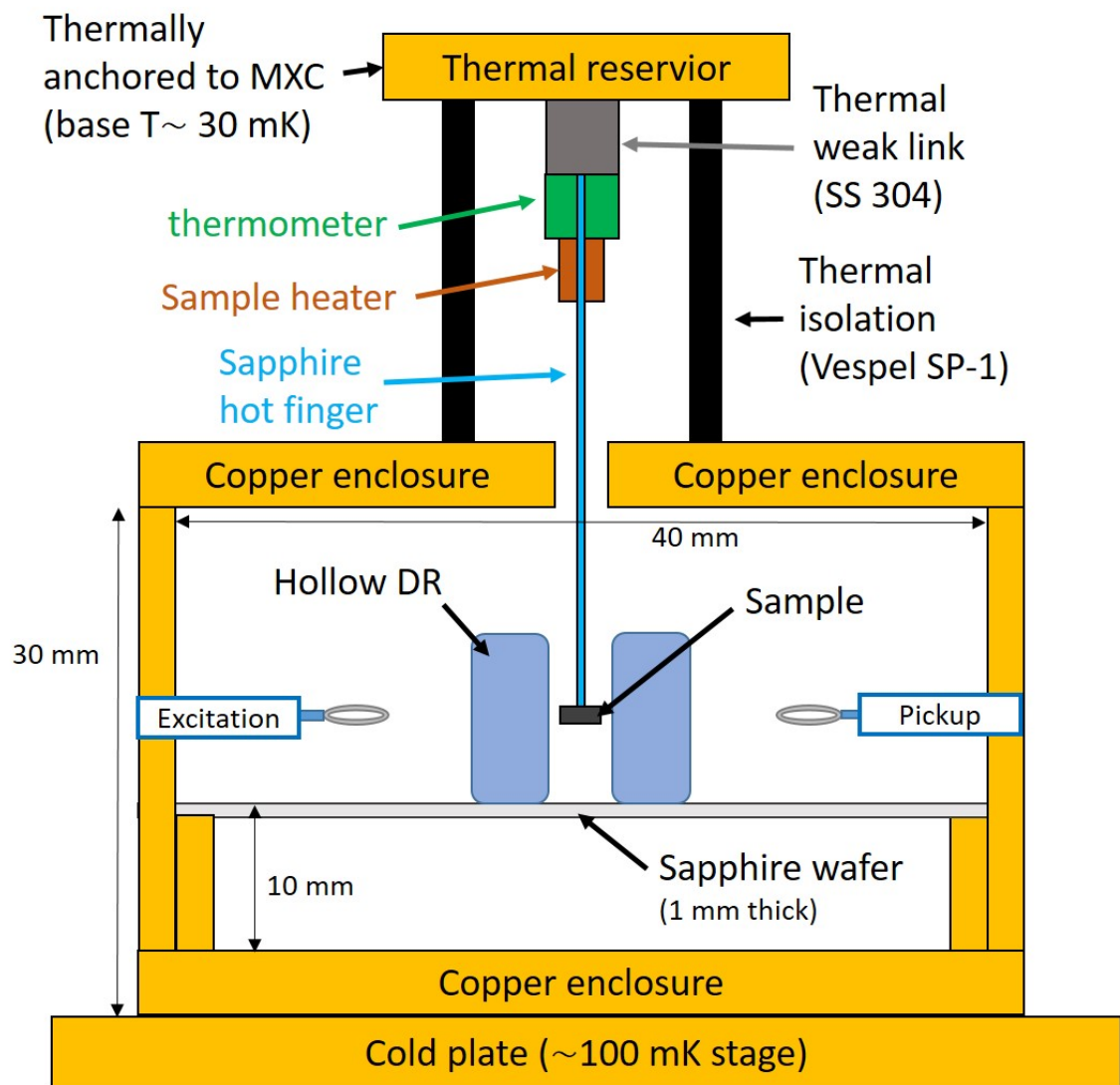


Fig. 6.9 The second generation, large-cavity hollow DR design with hot finger technique. In practice, this resonator will be inverted (upside down) when placed in the Bluefors XLD dilution fridge. The drawing is not to scale.

finger and sample varied. The sample quality factor  $Q_s(T)$  can be determined by the results of those two measurements [81] (after coupling effects are removed),

$$1/Q_u^{\text{wo sample}} = 1/Q_{\text{walls}} + 1/Q_{\text{diel}} + 1/Q_{\text{rad}}, \quad (6.31)$$

$$1/Q_u^{\text{w sample}} = 1/Q_s + 1/Q_{\text{walls}} + 1/Q_{\text{diel}} + 1/Q_{\text{rad}}, \quad (6.32)$$

$$1/Q_s(T) = 1/Q_u^{\text{w sample}}(T) - 1/Q_u^{\text{wo sample}}(T), \quad (6.33)$$

where the difference is carried out at each temperature of interest. Here,  $Q_u^{\text{w sample}}$  and  $Q_u^{\text{wo sample}}$  are the unloaded quality factor with and without the sample present. The surface resistance of the sample  $R_s$  can be determined from the sample quality factor  $Q_s$  (Eq. (6.26)). The geometric factor, to convert  $Q_s$  to  $R_s$  and to obtain the absolute value of  $X_s$ , can be found by the experimental method described in Sec. 6.2.3. In the following two chapters, the above described disk DR and hollow DR techniques will be applied to the topologically non-trivial superconductors, as promised.

## CHAPTER 7

---

### Microwave Meissner Screening study of an Artificial Topological Superconductor - $\text{SmB}_6/\text{YB}_6$

---

- This Chapter expands upon material previously published as Ref. [113].
- Recommended readings for this chapter: [28–30, 113–118]

In this chapter, a microwave penetration depth study of  $\text{SmB}_6/\text{YB}_6$  thin film bilayers, a proximity coupled topological insulator / superconductor (TI/SC) system, will be introduced. The TI/SC system is a representative example of artificial topological superconductors (TSC). The importance of studying the TI/SC bilayer system will be discussed and the strength of the microwave technique in characterizing the properties of this system will be demonstrated. Finally, the interpretation of the obtained characteristic properties of the TI/SC system through the microwave Meissner screening study will be discussed.

## 7.1 Motivation for a microwave study of TI/SC systems

Creating an experimental platform which hosts Majorana bound states (MBSs) in a condensed matter system is a goal that has received great attention recently [119, 120]. Due to robust topological protection, the MBS is a promising qubit candidate for quantum computation [121]. One of the platforms proposed to realize the MBS is a topological insulator / superconductor (TI/SC) bilayer system [28]. With the induced spinless  $p$ -wave superconductivity (a type of TSC) in the topological surface states (TSS), an MBS has been predicted to exist in its vortex core [29, 122–124]. Therefore, it is important for the physics community to establish and understand the properties of TI/SC bilayer systems.

There have been a number of studies on the Bi-based TI ( $\text{Bi}_2\text{Se}_3$ ,  $\text{Bi}_2\text{Te}_3$ , etc) / SC systems through point contact spectroscopy (PCS) [125], ARPES [22, 126], and STM [30, 127, 128] measurements. DC techniques such as PCS and STM probe the magnitude of the superconducting order parameter induced in the top surface of the TI with a probing depth range limited to the mean free path or coherence length, and cannot be applied to the case when an insulating bulk region is present (Fig. 7.1). ARPES studies the angle-resolved magnitude of the induced order parameter from the first few atomic layers of the top surface of the TI.

In contrast, a microwave Meissner screening study investigates the high frequency electromagnetic field response. The microwave field propagates through an insulating layer and penetrates inside the superconducting system to the scale of the

penetration depth, which is comparable to the thickness of typical thin-film bilayers ( $< 200$  nm) (Fig. 7.1). Since the field screening response is induced throughout the entire bilayer, it can reveal more details of the proximity-coupled bilayer [114, 115, 117, 129, 130] that are not directly available to the other techniques. It is also important to note that the screening response study does not require specialized surface preparation which is critical for success of many of the other techniques.

The distinct capabilities of the Meissner screening study on the proximity-coupled system have been previously demonstrated on conventional normal (N) / superconductor (S) bilayer systems such as Cu (N) / Nb (S) [115, 116, 131–138]. It can reveal the spatial distribution of the order parameter and the magnetic field profile throughout the film, as well as their evolution with temperature. From such information, superconducting characteristic lengths such as the normal coherence length  $\xi_N$  and normal penetration depth  $\lambda_N$  of the proximity-coupled normal layer can be estimated. The study can also reveal thickness dependent proximity-coupling behavior, which helps to estimate the thickness of the surface states ( $t_{\text{TSS}}$ ) for TI/SC bilayers. The  $\xi_N$ ,  $\lambda_N$ , and  $t_{\text{TSS}}$  of a proximity-coupled TI layer determine the radius of a vortex, the maximum spacing between vortices in a lattice, and the minimum thickness of the TI layer. Such information is required to avoid intervortex tunneling of MBSs, which would result in a trivial fermionic state [139].

Compared to other high frequency electromagnetic techniques such as THz optical measurement, the advantage of the microwave Meissner screening study for investigating the properties of a TI/SC bilayer is that the energy of a 1 GHz microwave photon ( $\approx 4 \mu\text{eV}$ ) is a marginal perturbation to the system. On the other hand, the

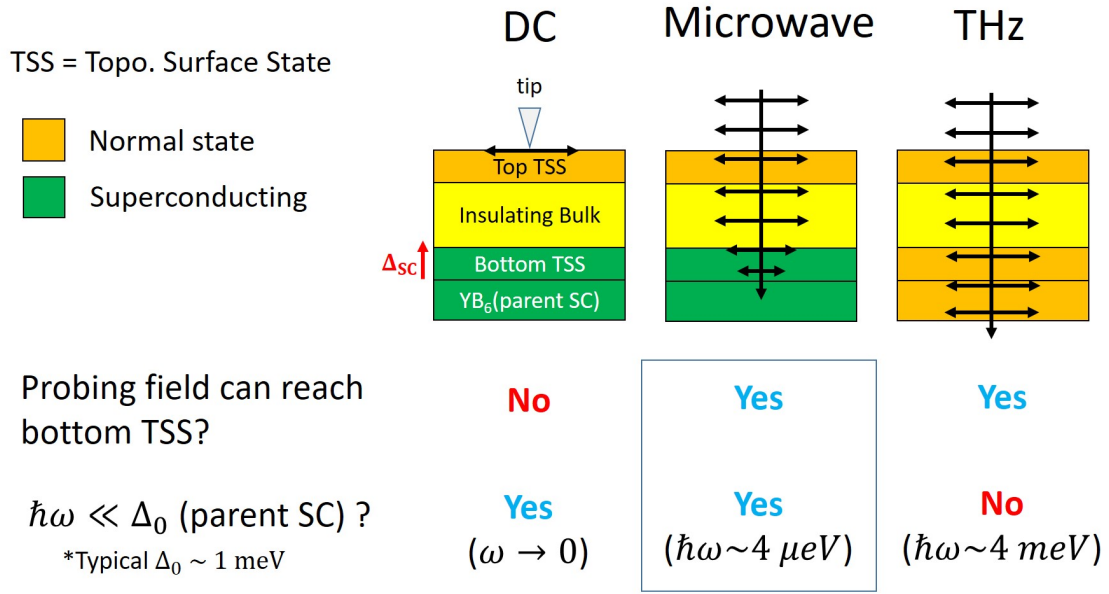


Fig. 7.1 Comparison table of DC, microwave, and THz techniques as characterization tools for the TI/SC system. Black arrows represent the spatial penetration of the probing signal of each technique. Here,  $\omega$  is the angular frequency of the probing signal, and  $\Delta_0$  is BCS gap of the parent superconductor.

energy of a 1 THz optical photon ( $\approx 4$  meV) is comparable to the gap energy ( $\leq 3$  meV) of typical superconductors used in TI/SC systems such as Nb, Pb, Al, NbSe<sub>2</sub>, and YB<sub>6</sub> [140–142]. This high photon energy of the THz technique breaks Cooper pairs, which hinders investigation of the ground state superconducting properties of the system. Therefore, the microwave screening study is an ideal method to study details of the induced order parameter in TI/SC bilayers. The advantages of the microwave study in TI/SC systems are well summarized in Fig. 7.1.

As seen from the advantages listed in Fig. 7.1, There is a clear demand for the demonstration of the microwave Meissner screening study for the TI/SC bilayer system. In the remainder of the chapter, we will introduce the results of our microwave Meissner screening study (penetration depth measurement) on SmB<sub>6</sub>/YB<sub>6</sub>.

$\text{SmB}_6/\text{YB}_6$  is a strong candidate for a topological Kondo insulator / superconductor bilayer systems. The existence of the insulating bulk in  $\text{SmB}_6$  has been under debate [23, 24, 143–148]. From measurements of the temperature dependence of the Meissner screening with a systematic variation of  $\text{SmB}_6$  thickness, our study shows evidence for the presence of an insulating bulk region in the  $\text{SmB}_6$  thin films. Through a model of the electrodynamics, the study also provides an estimation for the characteristic lengths of the bilayer system including the thickness of the surface states. The details of the experiment and the model will be discussed in the following sections.

## 7.2 Experiment

### 7.2.1 Sample preparation

$\text{SmB}_6/\text{YB}_6$  bilayers were prepared by an *in-situ* sequential sputtering process (i.e., without breaking vacuum) to insure the ideal superconducting proximity effect, which is a prerequisite for the current study and analysis [149].  $\text{SmB}_6$  and  $\text{YB}_6$  share the same cubic crystal structure with almost the same lattice constant ( $\approx 4.1 \text{ \AA}$ ), which allows the fabrication of bilayers by sequential high-temperature growth under the same conditions.  $\text{YB}_6$  is a superconducting rare-earth hexaboride and it has been reported that slight boron deficiency improves the superconducting transition temperature ( $T_c$ ) of  $\text{YB}_6$  [118]. Thus, for this study, slightly boron deficient  $\text{YB}_6$  films (B/Y = 5.6) were used as the superconducting layers.

YB<sub>6</sub> thin films were deposited on Si(001) substrates. To remove the native oxide layer on the Si substrate, we treated it with hydrofluoric acid (HF) before the thin film deposition. The base pressure of the deposition system was  $2 \times 10^{-8}$  Torr. The deposition process was performed at 860 °C under a pressure of 10 mTorr Ar gas (99.999 %). The thickness of the YB<sub>6</sub> layers for all films was fixed to be 100 nm. The subsequent SmB<sub>6</sub> deposition was performed under the same temperature and pressure conditions, and an additional sputtering of a B target was employed to compensate B deficiency which is present in the films fabricated by the sputtering of a stoichiometric SmB<sub>6</sub> target [149, 150]. The compositions (i.e., stoichiometry) of YB<sub>6</sub> and SmB<sub>6</sub> thin films were examined with wavelength dispersive spectroscopy (WDS) measurements. The thicknesses of the bilayers were confirmed with cross-sectional scanning electron microscopy (SEM) measurements.

The geometry of the bilayers is schematically shown in Fig. 7.2(a). The YB<sub>6</sub> film has a thickness of 100 nm and  $T_c = 6.1$  K obtained from a DC resistance measurement [118]. The thickness of the SmB<sub>6</sub> layers ( $t_{\text{SmB}_6}$ ) are varied from 20 to 100 nm for systematic study. These bilayers all have  $T_c = 5.8 \pm 0.1$  K without a noticeable  $t_{\text{SmB}_6}$  dependence of  $T_c$ .

## 7.2.2 Effective penetration depth measurement

The measurement of the effective penetration depth  $\lambda_{eff}$  is conducted with the rutile disk dielectric resonator (DR) setup described in Sec. 6.3.1. The resonator is cooled down to the base temperature of 40 mK. As the temperature of the sample

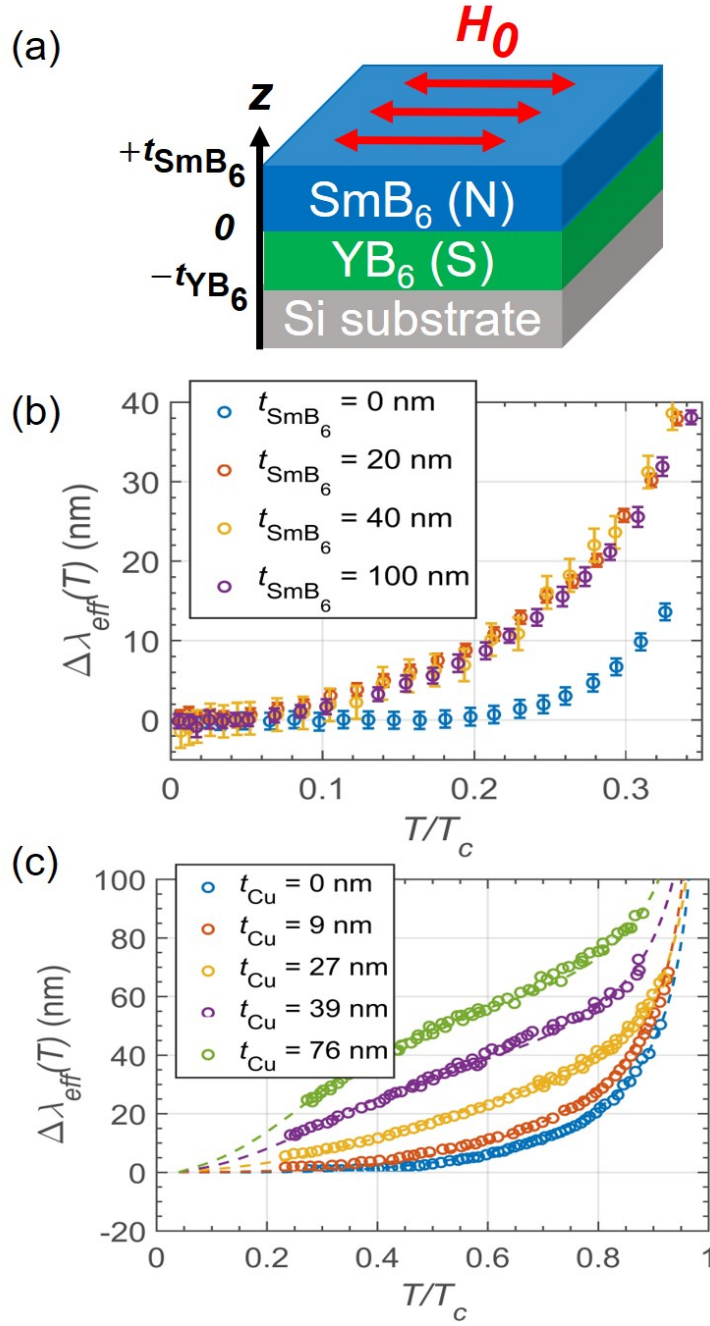


Fig. 7.2 (a) A schematic of the bilayer consisting of an SmB<sub>6</sub> film and a YB<sub>6</sub> film. A parallel microwave magnetic field ( $H_0$ ) is applied to the top surface of the SmB<sub>6</sub> layer (red arrows). (b) Temperature dependence of the effective penetration depth  $\Delta\lambda_{\text{eff}}(T)$  of the SmB<sub>6</sub>/YB<sub>6</sub> bilayers for various SmB<sub>6</sub> layer thickness ( $t_{\text{SmB}_6}$ ). (c)  $\Delta\lambda_{\text{eff}}(T)$  of a Cu/Nb (conventional metal / superconductor) bilayers [116] for various Cu layer thickness ( $t_{\text{Cu}}$ ). The dashed lines are the model fits [116].

is increased from the base temperature, the change of the resonance frequency is measured,  $\Delta f_0(T) = f_0(T) - f_0(T_{ref})$  (See Sec. 6.2.2).  $T_{ref}$  here is set to 230 mK ( $\approx 0.04T_c$  of the bilayers), below which  $f_0(T)$  of the bilayers shows saturated temperature dependence. This data is converted to the change in the effective penetration depth  $\Delta\lambda_{eff}(T)$  using a standard cavity perturbation theory [10, 151, 152],

$$\Delta\lambda_{eff}(T) = \lambda_{eff}(T) - \lambda_{eff}(T_{ref}) = -\frac{G_{geo}}{\pi\mu_0} \frac{\Delta f_0(T)}{f_0^2(T)}. \quad (7.1)$$

Here,  $G_{geo}$  is the geometric factor of the resonator described in Sec. 6.2.3. Note that the error bar in the  $\Delta\lambda_{eff}(T)$  data is estimated from the error bar of  $f_0$  (Sec. 6.2.2.1) and the standard error propagation from the relation between  $\Delta\lambda_{eff}(T)$  and  $f_0(T)$ .

Fig. 7.2(b) shows  $\Delta\lambda_{eff}(T)$  for the SmB<sub>6</sub> (N) / YB<sub>6</sub> (S) bilayers for various SmB<sub>6</sub> layer thickness  $t_{SmB_6}$ . The single layer YB<sub>6</sub> thin film (i.e.,  $t_{SmB_6} = 0$ ) shows temperature independent behavior below  $T/T_c < 0.2$ . This is not only consistent with the BCS temperature dependence of  $\Delta\lambda(T)$  for a spatially homogeneous, fully-gapped superconductor [15, 153], but also consistent with previous observations on YB<sub>6</sub> single crystals [142, 154]. However, once the SmB<sub>6</sub> layer is added,  $\Delta\lambda_{eff}(T)$  clearly shows temperature dependence below  $T/T_c < 0.2$ . Here, the important unconventional feature is that the low temperature profile of  $\Delta\lambda_{eff}(T)$  for the SmB<sub>6</sub>/YB<sub>6</sub> bilayers shows only a marginal  $t_{SmB_6}$  dependence. This is in clear contrast to the case of the Cu (N) / Nb (S) bilayers shown in Fig. 7.2(c). The  $\Delta\lambda_{eff}(T)$  for this conventional metal/superconductor bilayer system shows considerable evolution as the normal layer thickness  $t_{Cu}$  increases. This is because when the decay length of the

induced order parameter  $\xi_N(T)$  decreases with increasing temperature, the thicker (thinner) normal layer undergoes a larger (smaller) change in the spatial distribution of the order parameter, and hence the spatial profile of the screening. Therefore, the marginal  $t_{\text{SmB}_6}$  dependence of  $\Delta\lambda_{eff}(T)$  for the  $\text{SmB}_6/\text{YB}_6$  bilayer implies that even though  $t_{\text{SmB}_6}$  is increased, the actual thickness of the proximity-coupled screening region in the  $\text{SmB}_6$  layer remains roughly constant.

## 7.3 Model

### 7.3.1 Meissner screening model of the bilayer system

To quantitatively analyze this unconventional behavior, an electromagnetic screening model for a proximity-coupled bilayer is introduced.[115, 116, 136, 138] The model solves Maxwell's equations combined with the second London equation for the current and field inside the bilayer with appropriate boundary conditions at each temperature (See Appendix A), to obtain the spatial profile of the magnetic field  $H(z, T)$  and the current density  $J(z, T)$  as a function of temperature [115], where  $z$  denotes the coordinate along the sample thickness direction as depicted in Fig. 7.2(a). From the obtained field and current profiles, one can obtain the total inductance  $L(T)$  of

the bilayer as

$$\begin{aligned}
L(T) = & \frac{\mu_0}{H_0^2} \int_{-t_s}^0 [H^2(z, T) + \lambda_s^2(T)J^2(z, T)] dz \\
& + \frac{\mu_0}{H_0^2} \int_0^{+d_N} [H^2(z, T) + \lambda_N^2(z, T)J^2(z, T)] dz \\
& + \frac{\mu_0}{H_0^2} \int_{+d_N}^{+t_N} [H^2(z)] dz,
\end{aligned} \tag{7.2}$$

from which one can obtain an effective penetration depth from the relation  $L(T) = \mu_0 \lambda_{eff}(T)$ . Here,  $H_0$  is the amplitude of the applied microwave magnetic field at the top surface of the normal layer (see Fig. 7.2(a)),  $\lambda_s$  ( $\lambda_N$ ) is local penetration depth of the superconductor (normal layer),  $t_s$  is the thickness of the superconductor,  $t_N$  ( $N=SmB_6$  or Cu) is the total thickness of the normal layer, and  $d_N$  ( $\leq t_N$ , integration limit of the second and third terms in Eq. (7.2)) is the thickness of the proximity-coupled region in the normal layer, which is assumed to be temperature independent. In Eq. (7.2),  $H^2$  is proportional to field stored energy and  $\lambda^2 J^2$  is proportional to kinetic stored energy of the supercurrent. The first, second, and third integration terms come from the superconductor, the proximity-coupled part of the normal layer, and the uncoupled part of the normal layer, respectively.

A schematic view of the order parameter profile in the bilayers is shown in Fig. 7.3. As seen in Fig. 7.3(a), for a conventional metal,  $d_N$  is the same as  $t_N$  since the entire normal layer is uniformly susceptible to induced superconductivity, and thus the third integration term in Eq. (7.2) becomes zero. However, as seen in Fig. 7.3(b), if there exists an insulating bulk region blocking the propagation of the order parameter up to the top surface in the normal layer (as in the case of a thick TI), only the bottom

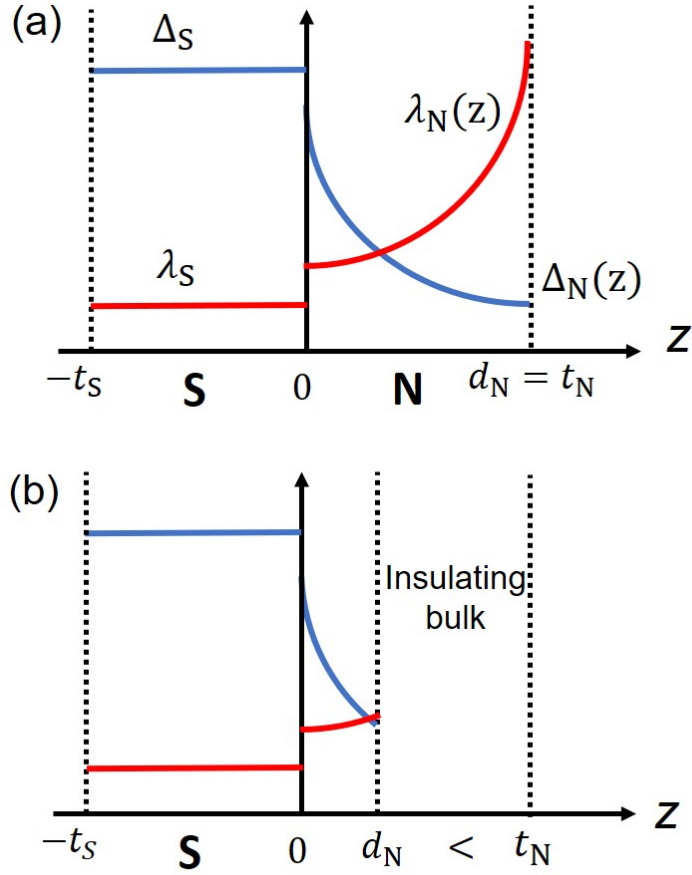


Fig. 7.3 (a) Schematic spatial profile of the order parameter  $\Delta_{N,S}$  (blue) and the local penetration depth  $\lambda_{N,S}$  (red) through the normal layer (N) / superconductor (S) bilayer sample for the case of the absence of an insulating bulk.  $z$  is the thickness direction coordinate and  $t_N$  ( $t_S$ ) is the thickness of the normal layer (superconductor). The proximitized thickness  $d_N$  is equal to the normal layer thickness  $t_N$ . (b) In the presence of an insulating bulk,  $d_N < t_N$  since the insulating bulk blocks propagation of the order parameter to the top surface. Note that the microwave magnetic field is applied to the right surfaces.

conducting surface adjacent to the superconductor is proximity-coupled. In this case,  $d_N$  becomes the thickness of the bottom conducting surface states. The third integration term in Eq. (7.2), which accounts for the uncoupled portion of the normal layer, becomes non-zero. However, this third term can be removed by taking  $\Delta L(T)$  into account since the un-coupled  $\text{SmB}_6$  region has temperature-independent microwave properties below 3 K [155], whereas the temperature range of the measurement here extends well below 2 K.

### 7.3.2 Spatial and temperature dependence of the Meissner screening

The spatial dependence of screening of the proximity-coupled normal layer is imposed by that of the induced order parameter  $\Delta_N$  (Fig. 7.3(a)), which can be approximated by an exponential decay profile  $\Delta_N(z, T) = \Delta_N(0, T)e^{-z/\xi_N(T)}$  in terms of the normal coherence length  $\xi_N(T)$  [117]. The position dependent normal penetration depth is inversely proportional to the order parameter  $\lambda_N \sim 1/\Delta_N$  [156] so its position dependence is expressed as  $\lambda_N(z, T) = \lambda_N(0, T)e^{z/\xi_N(T)}$ . Here, the temperature dependence of  $\lambda_N$  at the interface is assumed to follow that of the superconductor [157]  $\lambda_N(0, T)/\lambda_N(0, 0) = \lambda_S(T)/\lambda_S(0) \cong 1 + \sqrt{\pi\Delta_0/2k_B T} \exp(-\Delta_0/k_B T)$ , which is the asymptotic behavior below  $0.3T_c$  for a fully-gapped superconductor [15, 153].<sup>1</sup>

For the temperature dependence of the screening in the normal layer,  $\xi_N(T)$  plays a crucial role since it determines the spatial distribution of  $\Delta_N(z, T)$ . If the

---

<sup>1</sup> $\text{YB}_6$  is a well-known fully-gapped  $s$ -wave superconductor [142, 154]. The superconducting Hamiltonian of the proximitized surface states of the TI layer is expected to have an effective  $p_x + ip_y$  pairing symmetry [28], which is also fully-gapped in the  $k_{xy}$  plane where the screening response in our measurement is investigated.

sample is in the clean limit, the temperature dependence of the normal coherence length is given by  $\xi_N = \hbar v_F / 2\pi k_B T$ , where  $v_F$  denotes the Fermi velocity of the N layer. In the dirty limit, it is given by  $\xi_N = \sqrt{\hbar v_F l_N / 6\pi k_B T}$  [114], where  $l_N$  denotes the mean-free path of the N layer. For the model fitting, the simplified expressions  $\xi_N^{clean}(T) = \xi_N^{clean}(T_0) \times T_0 / T$  and  $\xi_N^{dirty}(T) = \xi_N^{dirty}(T_0) \times \sqrt{T_0 / T}$  are used, with  $\xi_N(T_0)$  as a fitting parameter. Here,  $T_0$  is an arbitrary reference temperature of interest. Note that the divergence of  $\xi_N(T)$  as  $T \rightarrow 0$  should be cut off below a saturation temperature due to the finite thickness of the normal layer, which is theoretically predicted [114, 158], and also experimentally observed from magnetization studies on other bilayer systems [134, 137]. In our measurements, the effect of this saturation of  $\xi_N(T)$  can be seen from the sudden saturation of the  $\Delta\lambda_{eff}(T)$  data below  $0.04T_c$  (see Fig. 7.2(b) and Fig. 7.4(b-d)). Therefore, only the data obtained in a temperature range of  $T/T_c \geq 0.04$  is fitted, where the  $\Delta\lambda_{eff}(T)$  data indicates that  $\xi_N$  is temperature dependent.

A given set of these parameters  $\lambda_S(0)$ ,  $\lambda_N(0,0)$ ,  $\xi_N(T_0)$ , and  $d_N$  determines a model curve of  $\Delta\lambda_{eff}(T)$ . Therefore, by fitting the experimental data to a model curve, one can determine the values of these characteristic lengths. This screening model has successfully described  $\Delta\lambda(T)$  behavior of various kinds of normal / superconductor bilayers [116, 136, 138].

## 7.4 Results

### 7.4.1 YB<sub>6</sub> Single layer

As seen in Fig. 7.4(a), the model is first applied to fit  $\Delta\lambda_{eff}(T)$  of a single layer YB<sub>6</sub> thin film (i.e., no SmB<sub>6</sub> layer on top) to obtain  $\lambda_s(0)$ : the simplest case where one needs to consider only the first term in Eq. (7.2). Here, the data in a temperature range of  $T < 1.6$  K ( $\approx 0.28T_c$  of the SmB<sub>6</sub>/YB<sub>6</sub> bilayers) is fitted to avoid the contribution from the niobium top plate to  $\Delta f_0(T)$ . The best fit is determined by finding the fitting parameters that minimize the root-mean-square error  $\sigma_{RMS}$  of  $\Delta\lambda_{eff}(T)$  between the experimental data and the model fit curves. The error bar for the estimated fit parameters are determined by a deviation from the estimated parameter value which increases  $\sigma_{RMS}$  by 5%. The best fit for the single layer YB<sub>6</sub> data gives  $\lambda_s(0) = 227 \pm 2$  nm (and  $2\Delta(0)/k_B T_c = 3.66 \pm 0.01$ ). This estimate is larger than the value  $\lambda_s(0) \approx 134$  nm measured by a muon spin rotation study from a single crystal YB<sub>6</sub> sample [142] with higher  $T_c = 6.94$  K (and  $2\Delta(0)/k_B T_c = 3.67$ ). This is reasonable considering that the higher  $T_c$  implies a longer mean free path  $l_{mfp}$  [159], and shorter  $\lambda_s(0)$  through the relation  $\lambda_s(0) = \lambda_L(0)\sqrt{1 + \xi_0/l_{mfp}}$  [160] where  $\lambda_L(0)$  is London penetration depth at  $T = 0$  K and  $\xi_0$  is BCS coherence length of the superconductor.

## 7.4.2 SmB<sub>6</sub>/YB<sub>6</sub> bilayer

We now fix the value of  $\lambda_s(0)$  of the YB<sub>6</sub> layer and focus on extracting the characteristic lengths of the induced superconductivity of the bilayers. Recent PCS measurements on a series of SmB<sub>6</sub>/YB<sub>6</sub> bilayers [118] help to reduce the number of fitting parameters: the point contact measurement on the bilayer with  $t_{\text{SmB}_6} = 20$  nm at 2 K showed perfect Andreev reflection, i.e., conductance doubling at the interface between a metal tip and the top surface of the SmB<sub>6</sub>, indicating that the entire 20 nm thick SmB<sub>6</sub> layer is proximity-coupled. Therefore,  $d_N$  is fixed to 20 nm when fitting the  $\Delta\lambda_{eff}(T)$  data of the bilayer with  $t_{\text{SmB}_6} = 20$  nm.

The fitting is conducted with the clean and the dirty limit temperature dependence of  $\xi_N(T)$  as shown in Fig. 7.4(b). The clean limit fit (blue) gives  $\xi_N^{clean}(2\text{K}) = 52 \pm 1$  nm,  $\lambda_N(0,0) = 340 \pm 2$  nm with  $\sigma_{RMS}$  of 0.237. On the other hand, the dirty limit fit (red) gives  $\xi_N^{dirty}(2\text{K}) = 262 \pm 180$  nm,  $\lambda_N(0,0) = 505 \pm 7$  nm with  $\sigma_{RMS}$  of 0.780. According to the fitting result, not only does the dirty limit fit apparently deviate from the data points, but also the  $\sigma_{RMS}$  of the dirty limit is three times larger than that of the clean limit, implying that the clean limit is more appropriate for describing  $\xi_N(T)$  of the SmB<sub>6</sub> layer. Henceforth, the  $\Delta\lambda_{eff}(T)$  data for the bilayers with other  $t_{\text{SmB}_6}$  is fit using the clean limit temperature dependence of  $\xi_N$ . Also, the obtained value of  $\xi_N(2\text{K}) = 52$  nm will be used when the data of the bilayers with other  $t_{\text{SmB}_6}$  is fitted, as the Fermi velocity of the surface bands, which determines the value of  $\xi_N$ , does not have a clear TI layer thickness dependence [22].

For the bilayers with  $t_{\text{SmB}_6} = 40$  and 100 nm,  $d_N$  is now set to be a free fitting

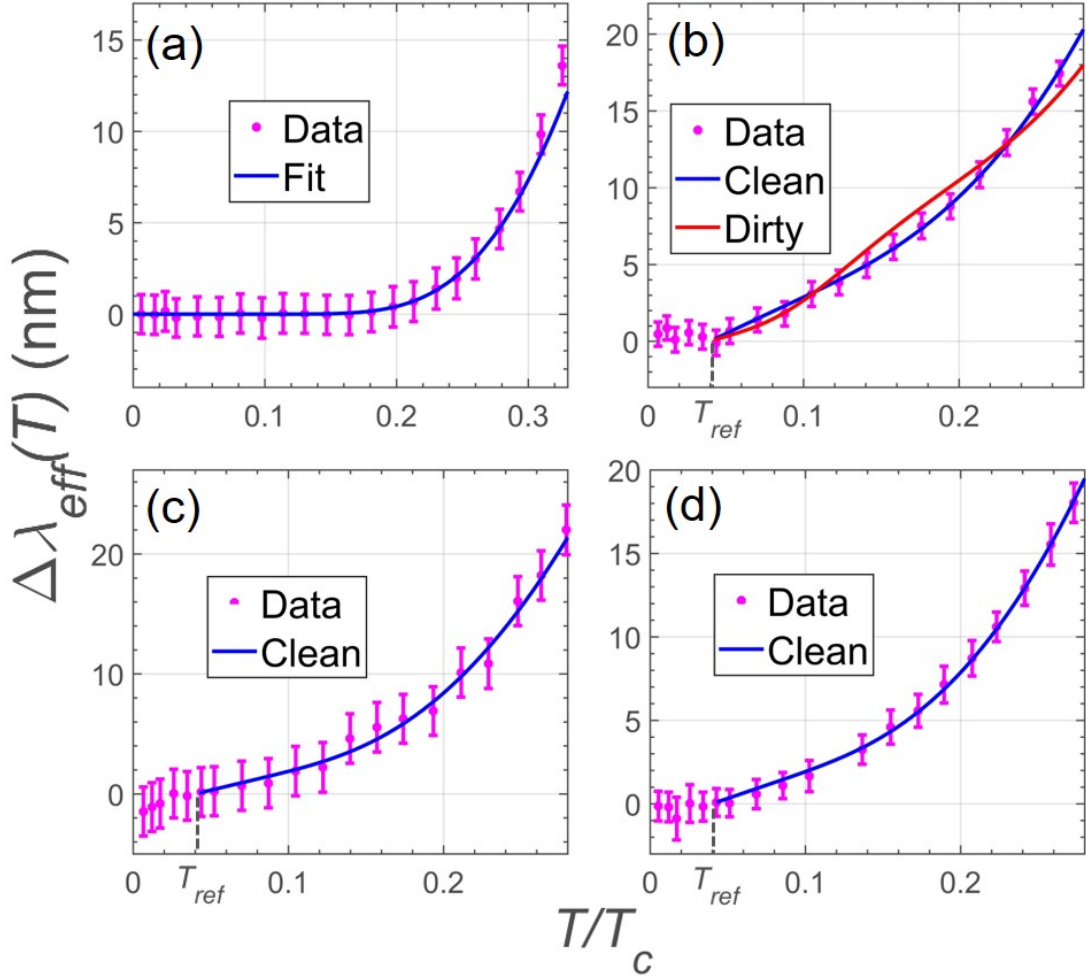


Fig. 7.4  $\Delta\lambda_{eff}(T)$  vs.  $T/T_c$  data and fits for  $\text{SmB}_6/\text{YB}_6$  bilayers at low temperature,  $T/T_c < 0.3$ . (a) The single layer  $\text{YB}_6$  (100 nm) ( $t_{\text{SmB}_6} = 0$  nm). The magenta points are data, and the blue line is a fit from the electromagnetic screening model. (b) The bilayer with  $t_{\text{SmB}_6} = 20$  nm. The blue line is a fit with the clean limit temperature dependence of  $\xi_N(T)$ , and the red line is a fit with the dirty limit temperature dependence. (c) and (d) The bilayers with  $t_{\text{SmB}_6} = 40$  nm and 100 nm, respectively.

Characteristic lengths	SmB <sub>6</sub> layer thickness		
	20 nm	40 nm	100 nm
$\xi_N(2\text{K})$ (nm)	$52 \pm 1$	52*	52*
$d_N$ (nm)	20*	$8 \pm 2$	$10 \pm 1$
$\lambda_N(0,0)$ (nm)	$340 \pm 2$	$159 \pm 2$	$207 \pm 2$

Table 7.1 Summary of the extracted characteristic lengths from the electrodynamic screening model for TI/SC bilayers for different  $\text{SmB}_6$  layer thickness. All fits on the bilayers assume  $\lambda_c(0) = 227$  nm which is obtained from the fitting on the single layer  $\text{YB}_6$ . Note that the values with the asterisk are fixed when the fitting is conducted.

parameter. As seen from Fig. 7.4(c) and (d), the resulting fit line gives  $d_N = 8 \pm 2$  nm,  $\lambda_N(0,0) = 159 \pm 2$  nm for the bilayer with  $t_{\text{SmB}_6} = 40$  nm, and  $d_N = 10 \pm 1$  nm,  $\lambda_N(0,0) = 207 \pm 2$  nm for the bilayer with  $t_{\text{SmB}_6} = 100$  nm. The estimated  $d_N \approx 9$  nm is much smaller than  $t_{\text{SmB}_6}$ , which is consistent with the absence of induced order parameter in the top surface of 40 and 100 nm thick SmB<sub>6</sub> layers measured by point contact spectroscopy [118]. A summary of the estimated characteristic lengths  $\xi_N(2\text{K})$ ,  $d_N$ , and  $\lambda_N(0,0)$  for the case of 20, 40, and 100 nm thick SmB<sub>6</sub> layers on top of YB<sub>6</sub> is presented in Table. 7.1.

### 7.4.3 Validity of the extracted characteristic lengths of the SmB<sub>6</sub>/YB<sub>6</sub> bilayers

To confirm the validity of the estimated values of the characteristic lengths of the SmB<sub>6</sub>/YB<sub>6</sub> bilayers obtained in Sec. 7.4.2, one of the parameters  $\xi_N$  is converted to the Fermi velocity  $v_F$ , whose value has been reported from other measurements on SmB<sub>6</sub>. From the clean limit relation  $\xi_N = \hbar v_F / 2\pi k_B T$ , one arrives at  $v_F = 8.5 \times 10^4$  m/s. As seen from Table. 7.2, this value is similar to the values obtained from the ARPES and DC transport measurements. However, the  $v_F$  values from theory and STM are an order of magnitude smaller. Recent DFT calculation accompanied by STM measurements [161, 162] and an independent theoretical calculation [163] show that the discrepancy can be explained by termination-dependent band bending at the surface of SmB<sub>6</sub>. The value of  $\xi_N(2\text{K})$  is also directly compared to that obtained from the DC transport study on Nb/SmB<sub>6</sub> bilayers [149]. The transport study has estimated

	This work	previous work
$\xi_N(2K)$ (nm)	52 (clean limit)	9[149] (dirty limit)
$v_F$ ( $10^4$ m/s)	8.5	4[164, 165] (ARPES) 9[149] (transport) 0.6[161] (STM) 0.4[166] (theory)
$t_{TSS}$ (nm)	$\approx 9$	6[149] (transport) 32[167] (spin pumping)

Table 7.2 Characteristic lengths ( $\xi_N$  and  $t_{TSS}$ ) of the SmB<sub>6</sub>/YB<sub>6</sub> bilayers and derived property (Fermi velocity  $v_F$ ) for SmB<sub>6</sub> obtained from the microwave Meissner screening study compared to those from previous studies.

a smaller value (9 nm) compared to our result (52 nm). This could be due to the differences in the grain size. Note that the grain size of the sample in the transport study is 4 nm whereas that of this study is 100 nm.

## 7.5 Implication of the results

### 7.5.1 Robust bulk insulation and thickness of the surface states

We now discuss the implications of these results and propose a microscopic picture for the proximity coupled bilayers. The important implication of the above results is the absence of Meissner screening in the bulk of proximity-coupled SmB<sub>6</sub>, which is consistent with the existence of an insulating bulk region inside the SmB<sub>6</sub> layer. If the entire SmB<sub>6</sub> layer is conducting without an insulating bulk inside, the proximity-coupled thickness  $d_N$  should be equal to  $t_{\text{SmB}_6}$  for thicker films too, considering the

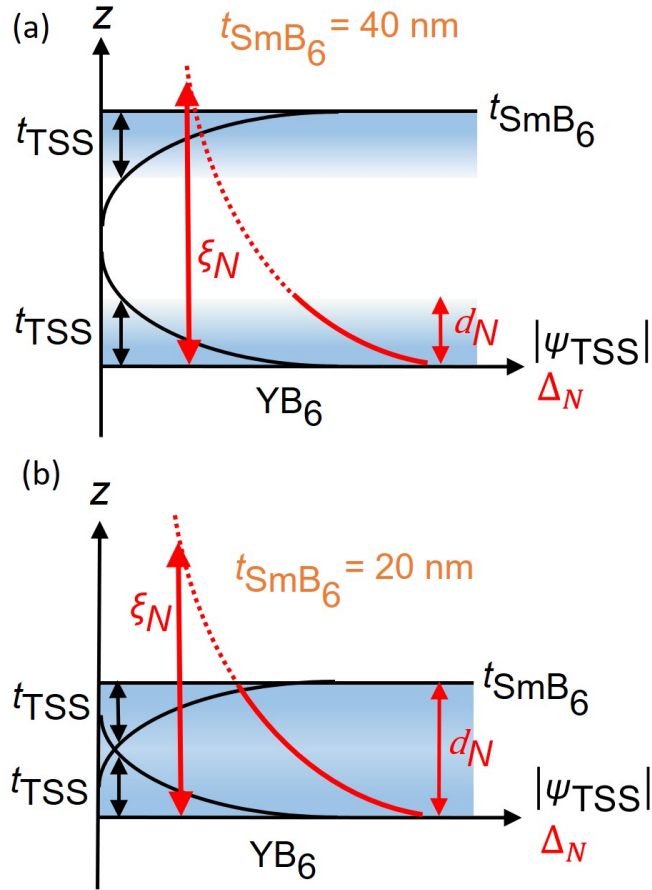


Fig. 7.5 Schematic view (not to scale) of the proposed position dependence of the surface states wavefunction  $|\psi_{\text{TSS}}(z)|$  (black) and induced order parameter  $\Delta_N(z)$  (red) in the  $\text{SmB}_6/\text{YB}_6$  bilayer. The  $|\psi_{\text{TSS}}(z)|$  is also visualized by the blue gradations. The sketches are based on the estimated proximity-coupled thickness  $d_N \approx 9$  nm and the normal coherence length  $\xi_N(2\text{K}) = 52$  nm for the case of  $t_{\text{SmB}_6} =$  (a) 40 nm, and (b) 20 nm.

long normal coherence length of  $\approx 52$  nm. In that case, as  $t_{\text{SmB}_6}$  increases, one would expect a continuous evolution of stronger  $\Delta\lambda(T)$  as seen in the Cu/Nb system (Fig. 7.2(c)), which is not observed in Fig. 7.2(b). Also, the estimated  $d_N \approx 9$  nm for the bilayers with  $t_{\text{SmB}_6} = 40$  and 100 nm is much smaller than half of  $t_{\text{SmB}_6}$ . As illustrated in Fig. 7.5(a), this situation can only be explained if a thick insulating bulk region of  $t_{\text{bulk}} \approx 22$  and 82 nm exists in the bilayers with  $t_{\text{SmB}_6} = 40$  and 100 nm respectively.

This thick insulating bulk provides a spatial separation between the top and bottom surface conducting states, not allowing the order parameter to propagate to the top surface. Thus, only the bottom surface states are proximitized in the  $t_{\text{SmB}_6} = 40$  and 100 nm cases, and hence one can conclude that the proximitized thickness  $d_N \approx 9$  nm equals the thickness of the surface states  $t_{\text{TSS}}$ . Note that this confirmation of the presence of the insulating bulk in the TI layer cannot be made solely from the PCS study. Even if the PCS study observed the absence of the order parameter on the top surface of the TI layer ( $\text{SmB}_6$  in this case), it could be either due to an insulating bulk, or due to a short normal coherence length  $\xi_N < t_{\text{SmB}_6}$ . The large value of  $\xi_N = 52$  nm, which is larger than  $t_{\text{SmB}_6} = 40$  nm, rules out the latter scenario and confirms the presence of an insulating bulk inside the  $\text{SmB}_6$  layers.

This picture is also consistent with the observation that the entire  $\text{SmB}_6$  layer with  $t_{\text{SmB}_6} = 20$  nm is proximity-coupled (Fig. 7.5(b)); the top and the bottom conducting surface state wavefunctions are likely to be weakly overlapped based on  $2t_{\text{TSS}} \approx t_{\text{SmB}_6}$  through the exponentially decaying profile (Fig. 7.5(b)). Thus the induced order parameter is able to reach to the top surface states, giving  $d_N = 20$  nm for this case. Although such overlap is expected to open a hybridization gap in the surface states, the fact that 20 nm  $\text{SmB}_6$  on  $\text{YB}_6$  is entirely proximity-coupled implies that the opened gap is much smaller than the energy difference between the Fermi level of  $\text{SmB}_6$  and the Dirac point. Note that topological protection might not be affected by such weak hybridization, provided that the Fermi level is sufficiently far away from the Dirac point present in thick  $\text{SmB}_6$  [22].

## 7.5.2 Design parameters for a vortex Majorana device

Besides confirming the existence of an insulating bulk in the  $\text{SmB}_6$  layer, the extracted fitting parameters based on the electromagnetic model provide an estimate for the important characteristic lengths such as  $\xi_N$ ,  $\lambda_N$ , and  $t_{\text{TSS}}$ , as seen from Sec. 7.4.2. These estimates can be utilized in designing a TI/SC device such as a vortex MBS device.  $\xi_N$  determines the radius of the vortex core  $r_v$ . In the mixed state above the first critical field,  $\lambda_N$  determines the maximum spacing  $R_v$  between neighboring vortices in the vortex lattice [160]. The ratio  $r_v/R_v$  determines the overlap of the two adjacent MBSs. The overlap of the wavefunctions of the two MBSs results in intervortex tunneling, which splits the energy level of the MBSs away from zero energy and makes them trivial fermionic excitations [139],

$$\Delta E_{\text{split}} \sim \frac{1}{\sqrt{k_F R_v(\lambda_N)}} \exp\left(-\frac{R_v(\lambda_N)}{r_v(\xi_N)}\right). \quad (7.3)$$

Therefore, information on  $\xi_N$  and  $\lambda_N$  helps to evaluate how secure the MBSs of a device will be against intervortex tunneling.

$t_{\text{TSS}}$  determines a minimum required thickness of the device. If the thickness of the device is too thin ( $t_{\text{SmB}_6} \sim t_{\text{TSS}}$ ), the wavefunction overlap between the top and bottom surface states becomes significant, which opens a large hybridization gap up to the Fermi level (Fig. 7.6(c)). As a result, the surface states lose not only the electric conduction but also lose the spin-momentum locking property [22]. In this case, an MBS is not hosted in the vortex core, and hence a thickness larger than the esti-

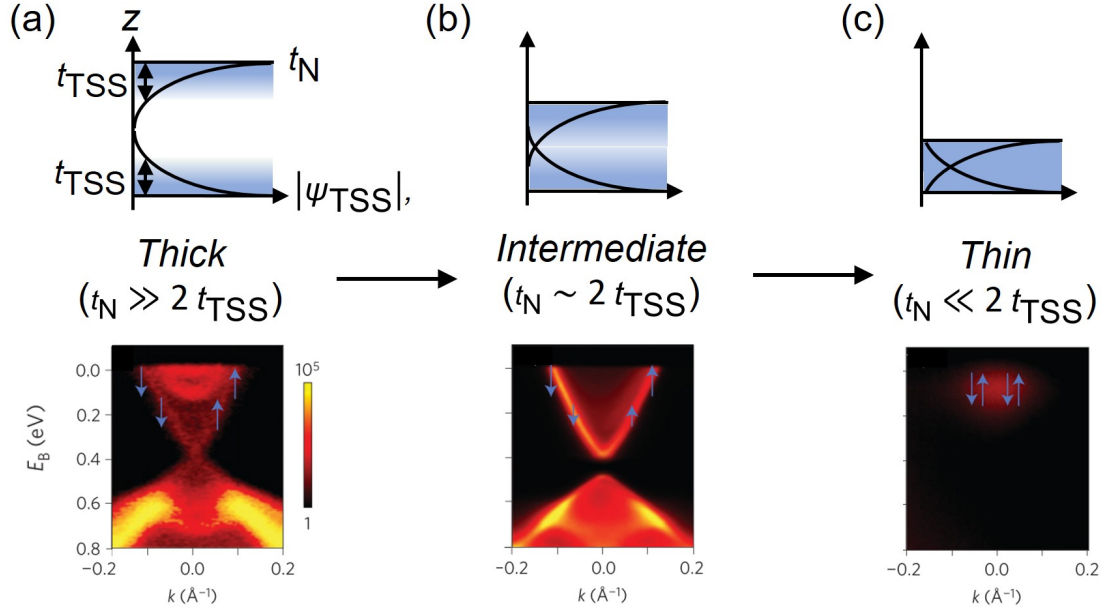


Fig. 7.6 (Top row) Illustrations (not to scale) of the surface state wavefunctions  $|\psi_{TSS}(z)|$  in a TI/SC bilayer for various limits of the TI layer thickness  $t_N$ . (Bottom row) Band structure near the Dirac point for each limit is plotted from the ARPES measurement on  $\text{Bi}_2\text{Se}_3/\text{NbSe}_2$ , a representative TI/SC bilayer (Ref. [22]). (a) For the thick TI layer limit ( $t_N \gg t_{TSS}$ ), no overlap occurs between the top and bottom surface state wave functions. (b) For the intermediate TI layer limit ( $t_N \sim 2t_{TSS}$ ), a small wavefunction overlap occurs. A small hybridization gap opens but it does not reach the Fermi level. The spin-momentum locking of the surface state is still intact. (c) For the thin TI layer limit ( $t_N \ll 2t_{TSS}$ ), the top and bottom surface states are fully hybridized. A large hybridization gap eliminates the linear Dirac dispersion.

mated  $2t_{TSS}$  is recommended. These discussions show how the characteristic lengths extracted from the Meissner screening study serve as a guideline to design a vortex MBS device with TI/SC bilayer systems.

## 7.6 Summary

In this chapter, a microwave Meissner screening study is introduced and utilized to investigate the spatially dependent electrodynamic screening response and the corresponding properties of the TI/SC bilayers, an example artificial Topological superconducting system. The advantages of the study in investigating the properties of a TI/SC system is demonstrated by the measurement and modeling of the temperature dependence of the screening with systematic TI-layer thickness variation. The study goes beyond the surface response to examine the screening properties of the entire TI layer, and uncovers the existence of an insulating bulk in the TI layer conclusively. Also, the study provides an estimate for characteristic lengths of the TI/SC bilayer, which sheds light on the design of a vortex MBS device providing guidelines for the radius of the vortex core, the energy level splitting due to the intervortex tunneling, and the thickness of the device. With its versatile capabilities, the microwave Meissner screening study can serve as a standard characterization method for a variety of TI/SC systems before using them as building blocks in topological quantum computation.

## CHAPTER 8

---

### Microwave Conductivity study of an Intrinsic Topological Superconductor - $\text{UTe}_2$

---

- This Chapter expands upon material previously published as Ref. [26].
- Recommended readings for this chapter: [12, 17, 26, 27, 168–173]

In this chapter, the microwave impedance spectroscopy method introduced in Chap. 6 will be applied to a candidate intrinsic topological superconductor (TSC),  $\text{UTe}_2$ . Intrinsic TSCs are expected to possess a Majorana normal fluid at their boundary on top of the superfluid in their bulk, analogous to topological insulators and semimetals. A microwave impedance  $Z_s$  measurement and consequent complex conductivity  $\tilde{\sigma}$  study is the right tool to investigate the expected mixture of normal and superfluid in an intrinsic TSC since  $\tilde{\sigma}$  is sensitive to the response of both fluids. Evidence for the existence of a normal fluid in the zero temperature limit, and the chiral spin-triplet pairing state of  $\text{UTe}_2$ , will be provided through this study.

## 8.1 Possibility of topological superconductivity in $\text{UTe}_2$

### 8.1.1 Types of intrinsic topological superconductors

As discussed in Sec. 1.3.2, fully gapped superconductors with certain symmetries can possess nontrivial topological invariants in their BdG hamiltonian [18]. The non-trivial topology gives rise to an intrinsic Majorana normal fluid at the boundary, which is protected by the superconducting gap. Despite the intense interest arising from their potential application for topological quantum computation, there have been only a few TSC candidate materials, such as  $\text{Sr}_2\text{RuO}_4$  [174] and  $\text{Sn}_{1-x}\text{In}_x\text{Te}$  [175]. The pairing state of  $\text{Sr}_2\text{RuO}_4$  is still controversial [168], raising doubts on the possibility of TSC in this material. The pairing state of  $\text{Sn}_{1-x}\text{In}_x\text{Te}$  is very sensitive to disorder [17], being an obstacle for further examining the possibility of TSC.

For the case of nodal superconductors, due to the existence of the nodes in the gap, there is no global topological protection for a surface normal fluid. However, when a superconductor with accidental point-nodes breaks time-reversal symmetry (TRS), the nodes come in pairs and may possess Chern numbers<sup>1</sup> with opposite sign [17, 169]. In this case, the system is predicted to host gapless Majorana arc states in the surface Brillouin zone, which connect the pairs of point nodes (Fig. 8.1) [169]. The nodes and surface arc states connecting the nodes are protected (robust) by the topological invariant (Chern number) assigned to the nodes, so this system forms a second type of intrinsic topological superconductor with surface normal fluid. Since

---

<sup>1</sup>A Chern number is a type of topological invariant which is defined by geometric phase (Berry phase) of the electron wavefunction.

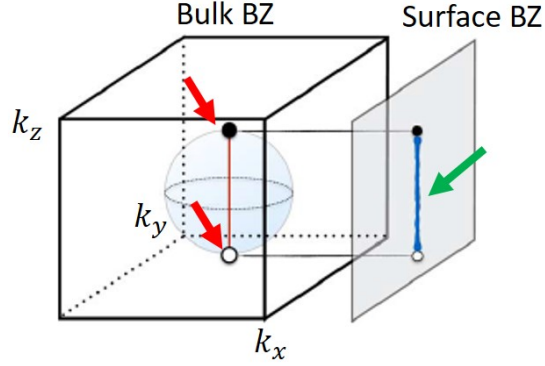


Fig. 8.1 (Left) Bulk Brillouin zone (BZ) of a time-reversal symmetry breaking superconductor with two point nodes (red arrows) on the Fermi surface (sphere). These two point nodes may have non-zero Chern numbers with opposite sign (denoted as black and white). (Right) Surface Brillouin zone of such a system. Surface Majorana arc states which connect the pair of point nodes are depicted by the blue line (green arrow). Reprinted with permission from Ref. [169].

the nodes in the superconducting gap and the Majorana arc are analogous to the Weyl nodes in the Fermi surface and the Fermi arc of a Weyl semimetal, the system is often nick-named a "Weyl superconductor" [17].

### 8.1.2 Possibility of Weyl superconductivity in $\text{UTe}_2$

A Weyl superconductor has not been found in spite of its exotic topological phase and the predicted surface Majorana normal fluid. This is because the system is required to break TRS, but superconductors with broken TRS are extremely rare. However, a recently discovered equal-spin-triplet superconductor  $\text{UTe}_2$  [170] has showed evidence of broken TRS [27]. One of the representative methods to check for broken TRS is the polar Kerr effect measurement [176]. The polar Kerr effect is the rotation of the polarization angle of a light reflected from a magnetic material. By investigating

the rotation angle across the  $T_c$  of a superconductor, one can check whether the superconducting state of the material breaks TRS. Indeed, as seen in Fig. 8.2(a), a  $\text{UTe}_2$  crystal shows a finite polar Kerr rotation as the system enters the superconducting state, which indicates the broken TRS in this system.

Another method to check the possibility of broken TRS for the case of the spin-triplet superconductor is the specific heat measurement. The superconducting order parameter of a triplet superconductor is in a vector form  $\vec{d}$ , contrary to the scalar order parameter  $\Delta$  of a singlet superconductor. The orbital magnetic moments  $\vec{m}_{orb}$  of the Cooper pair of a triplet superconductor can be represented by its vector order parameter;  $|\vec{m}_{orb}| \sim |\vec{d} \times \vec{d}^*|$  [177]. A non-zero  $\vec{m}_{orb}$  breaks the TRS of a system. For  $\vec{m}_{orb}$  to be non-zero,  $\vec{d}$  should have a chiral (complex) form with a two-component order parameter;  $\vec{d} = \vec{d}_1 + i\vec{d}_2$ . Therefore, having the two-component order parameter is the prerequisite for a triplet superconductor to break TRS. The specific heat measurement should show a sharp jump in its temperature dependence when each order parameter develops. As seen in Fig. 8.2(b), the specific heat data across the  $T_c$  of the  $\text{UTe}_2$  crystals show two sharp jumps, implying the existence of a two-component order parameter in this material. The evidence again supports the scenario of broken TRS in  $\text{UTe}_2$ .

With evidence of broken TRS, it is a natural question whether one can find evidence of a chiral spin-triplet pairing state with nodes in the gap (Weyl nodes) in  $\text{UTe}_2$ , and the existence of the expected surface normal fluid. To address this question, a microwave complex conductivity  $\tilde{\sigma} = \sigma_1 - i\sigma_2$  study (Chap. 6) is employed with  $\text{UTe}_2$ . The real part  $\sigma_1$  is dominated by the response from the normal fluid. Hence

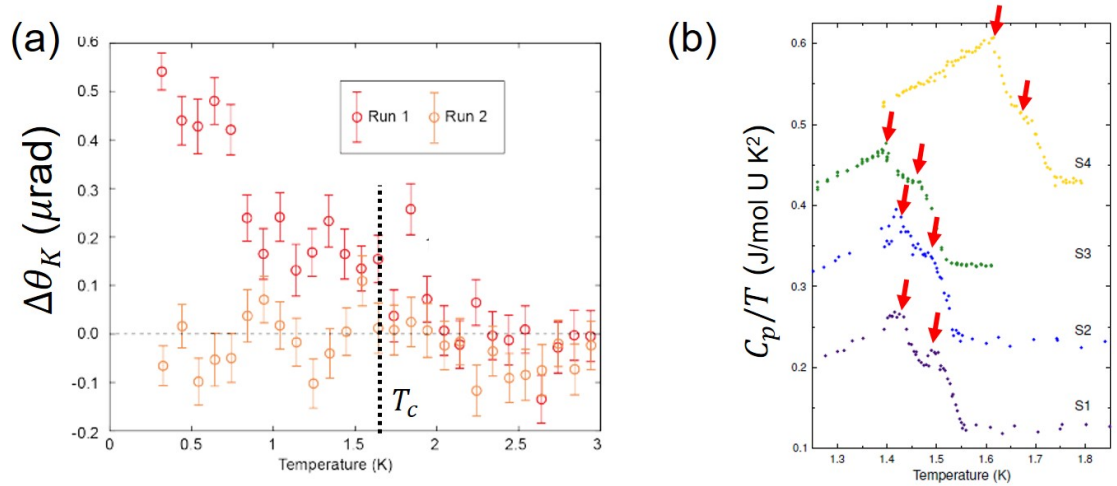


Fig. 8.2 (a) Polar Kerr rotation measurement on the  $ab$ -plane of a  $\text{UTe}_2$  single crystal under zero-field cooldown. The difference between the results of two cooldowns is attributed to the formation of different magnetic moment domains below  $T_c$  in each cooldown. (b) Specific heat measurement of  $\text{UTe}_2$  near  $T_c$ , showing clear two transition behavior (red arrows). These two results are reprinted from Ref. [27].

$\sigma_1$  is ideal to examine the question of the existence of the surface normal fluid. The imaginary part  $\sigma_2$  is dominated by the superfluid response. Hence  $\sigma_2$  is ideal to study the superconducting pairing state. This complex conductivity  $\tilde{\sigma}$  can be obtained once the surface impedance  $Z_s$  of the sample is measured (Eq. 6.15). Therefore, in the following sections,  $Z_s$  measurement of  $\text{UTe}_2$  will be discussed.

## 8.2 Experiment

### 8.2.1 UTe<sub>2</sub> sample growth and preparation

For the microwave impedance measurement, single crystal samples (S1, S2, and S3) of UTe<sub>2</sub> were grown by the chemical vapor transport method using iodine as the transport agent [170]. The crystal structure is orthorhombic where the *a* (and *b*)-axis consists of a chain of U (and Te) atoms each, as shown in Ref. [170]. The sample sizes are about  $\sim 2 \times 3 \times 0.5 \text{ mm}^3$  for S1, S2 and  $\sim 1.8 \times 2 \times 0.5 \text{ mm}^3$  for S3 with the shortest dimension being the crystallographic *c*-axis of the orthorhombic structure. For the microwave surface impedance measurement, the top and bottom *ab*-plane facets were polished on an aluminum oxide lapping film with  $0.3 \text{ }\mu\text{m}$  particle size. The mid-point  $T_c$  of the samples from DC transport measurements ranges from 1.6 to 1.75 K. Samples S1, S2 were polished under ambient conditions and then stored in a nitrogen-filled gloved box (oxygen content < 0.5 ppm). Sample S3 was polished and encapsulated by Apeizon N grease inside a nitrogen-filled glove bag (oxygen content < 0.05%) to exclude the possibility of surface oxidization. After this treatment, Sample S3 was stored in the same nitrogen-filled glove box (oxygen content < 0.5 ppm) when the sample was not in use.

## 8.2.2 Microwave impedance measurement in the disk DR

The initial  $Z_s$  measurement on sample S1 was conducted with the disk DR whose setup and the measurement procedure is explained in Sec. 6.3.1. A rutile disk was placed on top of the sample surface and facilitates microwave transmission resonances (Fig. 8.3(a)). The  $TE_{011}$  resonance mode occurs at  $\approx 11$  GHz in this structure. The microwave magnetic field of the mode is radial from the axis of the disk (which is parallel to the  $c$ -axis of the sample) and induces an azimuthal circulating current on the  $ab$ -plane sample surface, and hence surveys the  $ab$ -plane electrodynamic response. The temperature of the sample was varied from 20 mK to 2.4 K. As the temperature of the sample was varied, the change in resonant frequency  $\Delta f_0(T) = f_0(T) - f_0(T_{min})$ , and the quality factor  $Q(T)$  were measured. To avoid sample heating by microwave currents, weak microwave power  $P_{in} = -30$  dBm was used.<sup>2</sup> Note that we found the  $P_{in}$  dependence of  $f_0(T)$  saturates below  $P_{in} = -25$  dBm (Fig. 8.3).

The measured resonant properties ( $f_0(T), Q(T)$ ) can be converted into surface resistance  $R_s(T)$  and the change in surface reactance  $\Delta X_s(T)$  as explained in Sec. 6.2.3. The exact absolute value of  $X_s$  should be obtained by equating  $R_s(T) = X_s(T)$  in the temperature region where  $dR_s/dT = dX_s/dT$  is satisfied due to the large scattering rate above  $T_c$  (See Sec. 6.2.3). This temperature region is typically much higher than  $T_c$  and cannot be reached in the disk DR due to the background temperature dependence from the niobium top plate above  $\sim 2.5$  K. Thus the main utility of the disk DR is to obtain a rough estimate for  $Z_s$  by equating  $R_s(T)$  and  $X_s(T)$  just above

---

<sup>2</sup>This value is the power at the output port of the network analyzer. The actual microwave power incident to the resonator is  $\approx P_{in} - 10$  dB due to the cable loss at 11 GHz.

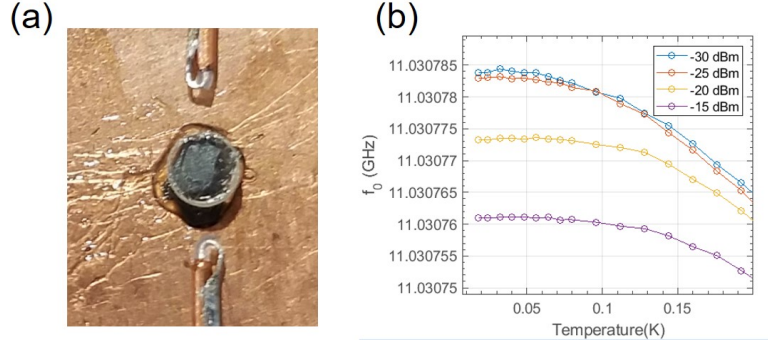


Fig. 8.3 (a) Top view of the rutile disk (transparent disk) placed on top of a UTe<sub>2</sub> crystal (grey). The input and output coupling loops are also shown. (b) Input microwave power  $P_{in}$  dependence of the resonant frequency  $f_0(T)$  of a UTe<sub>2</sub> crystal measured in a disk DR. For input power below  $-25$  dBm, no change in  $f_0(T)$  was seen, implying that the sample heating effect is not present.

$T_c$  assuming the large scattering rate regime is almost reached. As the slope of  $R_s(T)$  ( $dR_s/dT$ ) and  $\Delta X_s(T)$  ( $dX_s/dT$ ) is similar above  $T_c$  (Fig. 8.4(a)), this trick will not change the qualitative behavior and the temperature dependence of  $Z_s$  in the low temperature limit ( $T < 0.3T_c$ ). Hence, it is a good place to start. The data and analysis which will be presented in the sections below is on sample S1 in the disk DR unless otherwise noted. For the quantitatively rigorous approach to obtaining the absolute  $X_s$ , the hollow DR setup has been designed (Sec. 6.3.2, 6.3.3) but is still under construction at the moment this thesis is being written. This new setup will facilitate measurement of the absolute value of  $Z_s$  of UTe<sub>2</sub> without any ambiguity.

One thing to note before discussing the  $Z_s$  measurement results is the sample thickness and shape. The microwave field intensity decays exponentially within a magnetic penetration depth inside a superconductor. Therefore, the microwave response of the sample originates from a depth of  $1 \sim 2$  magnetic penetration depths.

This means that if there exists a surface response distinct from a bulk response, the contribution from the surface would not be overwhelmed by that of the bulk even though the thickness of the sample is much larger than the penetration depth. Also, the microwave current density is sharply enhanced at the exposed edges and surfaces as the magnetic field changes its direction rapidly [36], which increases the weighting factor for the surface contribution even further. Therefore, if there exists a surface normal fluid response, one should still be able to observe a signature of it from  $Z_s$  study even in a thick single crystal.

## 8.3 Results

### 8.3.1 Microwave surface impedance and complex conductivity

The left y-axis of Fig. 8.4(a) shows the obtained surface impedance  $Z_s = R_s + iX_s$  of sample S1 as a function of temperature. The surface resistance  $R_s$  decreases monotonically below  $T_c \approx 1.6$  K and reaches a surprisingly high residual value  $R_s(0) \approx 22$  m $\Omega$  at 11 GHz. To have a better sense on how large the residual  $R_s(0)$  of UTe<sub>2</sub> is, the normalized  $R_s$  (normalized by  $R_n = R_s(T_c)$ ) of UTe<sub>2</sub> is compared to that of a few examples of topologically trivial superconductors in Fig. 8.4(b). Below  $T_c$ , the fully-gapped *s*-wave superconductor Ti shows a sharp drop in  $R_s(T)/R_n$  and the residual value  $R_s(0)/R_n \approx 0$ . Even for the case of the line nodal *d*-wave superconductor CeCoIn<sub>5</sub>, the residual  $R_s$  is finite but small ( $R_s(0)/R_n \approx 0.04$ ). Contrary to these cases,

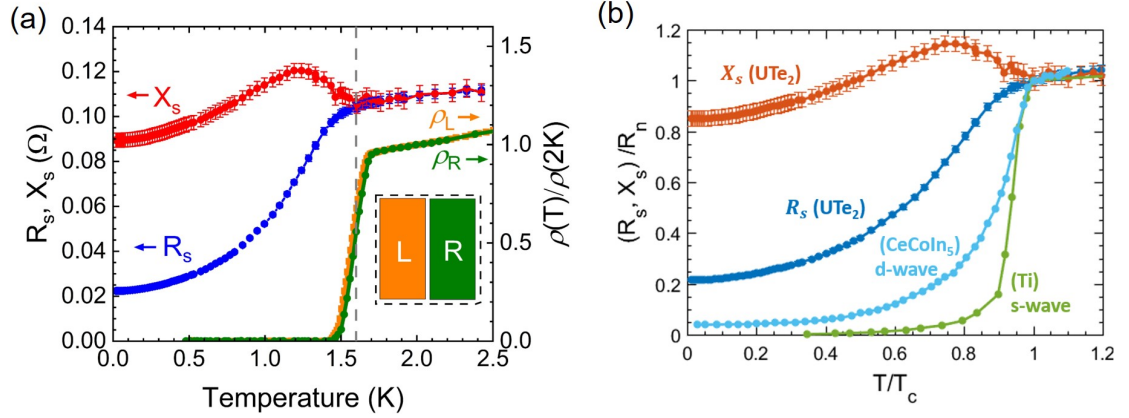


Fig. 8.4 (a) The measured temperature dependence of the surface impedance  $Z_s$  of a  $\text{UTe}_2$  sample (S1) at 11 GHz. The blue curve represents the surface resistance  $R_s$  and the red curve represents the surface reactance  $X_s$ . The two curves were constrained to merge above  $\approx 1.6$  K which is the  $T_c$  of this sample. After the surface impedance measurement, the sample (dashed rectangle inset) was divided into two pieces (L and R). Normalized electric resistivity for L (orange) and R (green) were measured with a 4 contact transport technique. The vertical dashed line shows the mid-point  $T_c$  of these pieces. (b) Normalized plot of  $Z_s(T)$  of  $\text{UTe}_2$  sample S1 is compared to  $R_s$  of the examples of topologically trivial superconductors measured at a similar frequency-to-gap ratio  $\hbar\omega/2\Delta_0 \approx 0.08$ . The skyblue line is  $R_s(T)$  of a  $\text{CeCoIn}_5$  single crystal (Ref. [90]) and Green line is  $R_s(T)$  of a Ti thin film (Ref. [178]). The normalization is done by dividing  $Z_s$  by  $R_n = R_s(T_c)$ .

$\text{UTe}_2$  shows a large residual  $R_s$  ( $R_s(0)/R_n \approx 0.21$ ). Note that all three datasets are obtained from the measurement with the same frequency-to-gap ratio  $\hbar\omega/2\Delta_0 \approx 0.08$  for a fair comparison. The result of the comparison qualitatively shows that there exists a significant dissipation channel in  $\text{UTe}_2$  even in the zero-temperature limit, implying the existence of a substantial normal fluid. Also note that the sample S1 was cut into two pieces after the  $Z_s$  measurement, and their electric resistivity (right y-axis of Fig. 8.4(a)) was measured. The temperature-dependent resistivity from each piece is identical, implying good homogeneity of the sample.

### 8.3.2 Real part of $\tilde{\sigma}$ analysis

To see the dissipative channel from the possible residual normal fluid more clearly, the  $Z_s$  data of sample S1 is converted into  $\tilde{\sigma} = \sigma_1 - i\sigma_2$  with Eq. (6.15) assuming the local electrodynamics regime. The validity of this assumption, at least in the superconducting state, will be discussed in Sec. 8.3.3. Figure 8.5(a) shows  $\sigma_1$  and  $\sigma_2$  of S1 as a function of temperature.<sup>3</sup> Here, an anomalous feature is the monotonic increase of  $\sigma_1(T)$  as  $T$  decreases. Note that  $\sigma_1$  is a property solely of the normal fluid. For superconductors with a topologically trivial pairing state, most of the normal fluid turns into superfluid and is depleted as  $T \rightarrow 0$ . As a result, in the low temperature regime,  $\sigma_1$  shows a strong decrease as temperature decreases, and is expected to reach a theoretically predicted residual value  $\sigma_1(0)/\sigma_1(T_c) = 0$  (for fully gapped  $s$ -wave [179]) and  $0.1 \sim 0.3$  (for line nodal  $d_{x^2-y^2}$ -wave [180, 181]). As shown in Fig. 8.5(b), this behavior is observed from the case of Ti [178] ( $s$ -wave) as well as CeCoIn<sub>5</sub> [90] ( $d_{x^2-y^2}$ -wave). In contrast, the UTe<sub>2</sub> crystal shows a monotonic increase in  $\sigma_1$  as the temperature decreases and reaches a much larger  $\sigma_1(0)/\sigma_1(T_c) = 1.25$ , implying the normal fluid conduction channel is still active and provides a significant contribution even at the lowest temperature.

---

<sup>3</sup>Note that the relatively large size of the error bar is not the statistical (physical) error bar but determined by the deviations of  $f_0$ ,  $Q$  which increase the root-mean-square error of  $S_{21}(f)$  fit by 5%, followed by error propagation.

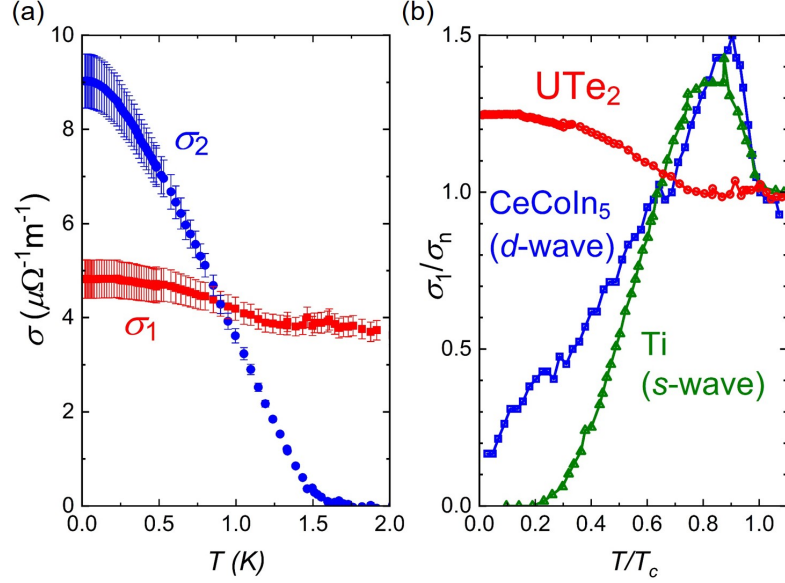


Fig. 8.5 (a) Real (red) and imaginary (blue) part of the complex conductivity  $\tilde{\sigma} = \sigma_1 - i\sigma_2$  of the UTe<sub>2</sub> sample (S1) at 11 GHz. (b) Normalized real part of conductivity of UTe<sub>2</sub> (red), a line nodal  $d_{x^2-y^2}$ -wave superconductor CeCoIn<sub>5</sub> (blue) [90], and a fully gapped  $s$ -wave superconductor Ti (green) [178] versus reduced temperature  $T/T_c$ . All measurements are done with the same low frequency-to-gap ratio of  $\hbar\omega/2\Delta_0 \approx 0.08$ .

### 8.3.3 Imaginary part $\tilde{\sigma}$ analysis

Another property one can extract from the complex conductivity is the effective penetration depth.  $\sigma_2(T)$  determines the absolute value of the effective penetration depth at each temperature as  $\sigma_2(T) = 1/\mu_0\omega\lambda_{\text{eff}}^2(T)$ . Figure 8.6(a),(b) show the obtained  $\lambda_{\text{eff}}(T)$  of sample S1, S2. From the temperature dependence  $\lambda_{\text{eff}}(T)$ , a zero temperature absolute penetration depth  $\lambda_{\text{eff}}(0)$  can be obtained by extrapolating the data with a power law fit  $\lambda_{\text{eff}}(T) - \lambda_{\text{eff}}(0) = aT^c$  over the low temperature regime  $T < 0.3T_c$  as seen in Fig. 8.6(c). The fit results in  $\lambda_{\text{eff}}(0) = 1126$  nm and  $c = 2.00$  for S1 ( $\lambda_{\text{eff}}(0) = 947$  nm and  $c = 1.92$  for S2) [172]. This value is similar to the Ura-

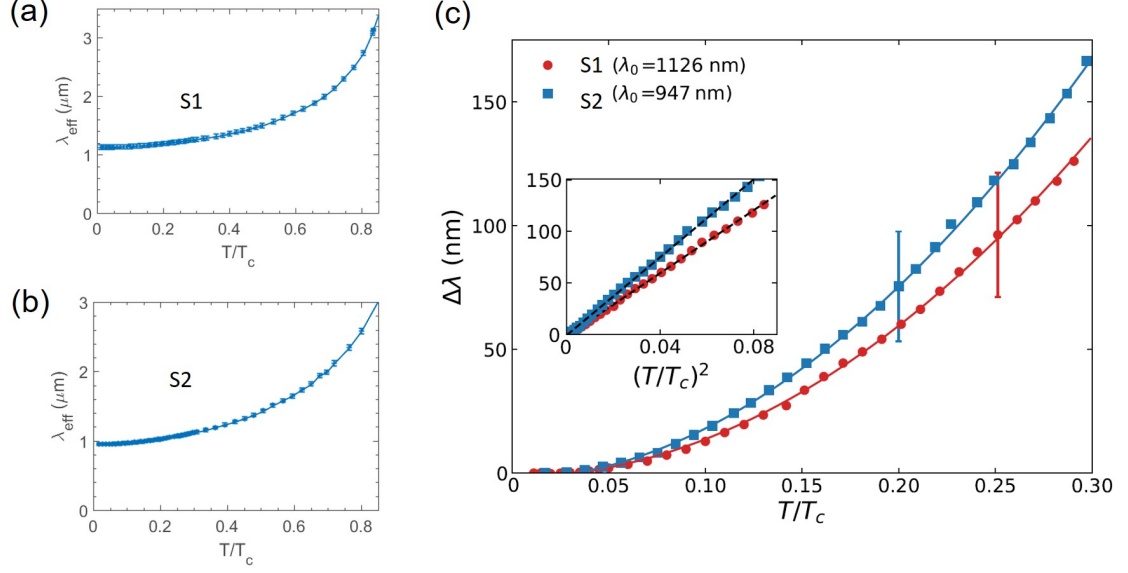


Fig. 8.6 Absolute value of the effective penetration depth  $\lambda_{\text{eff}}$  of sample (a) S1 and (b) S2. (c) Temperature dependence of the penetration depth  $\Delta\lambda_{\text{eff}}(T)$  at low temperature  $T/T_c < 0.3$  of the sample S1, S2 and their fits to a power law  $\Delta\lambda_{\text{eff}}(T) = aT^c + b$ . The vertical dash line is the estimated error bar (See Sec. 6.2.2.1). Inset is the same data plotted in terms of  $(T/T_c)^2$  to examine the quadratic ( $c = 2$ ) temperature dependence. The linear dash line is a guide to the eyes. (c) is reprinted from Ref. [172] with permission.

mium based ferromagnetic superconductor series such as UCoGe ( $\lambda_{\text{eff}}(0) \sim 1200$  nm) [182] and URhGe ( $\lambda_{\text{eff}}(0) \sim 900$  nm) [183], where UTe<sub>2</sub> represents the paramagnetic end member of the series [170]. This result is also consistent with recent muon-spin rotation measurements on UTe<sub>2</sub> which concluded  $\lambda_{\text{eff}}(0) \gtrsim 1000$  nm [184]. Note that the estimated  $\lambda_{\text{eff}} \gtrsim 1000$  nm is much larger than the BCS coherence length  $\xi_0 < 10$  nm for all three crystallographic axis estimated from  $H_{c2}$  measurement [170], the assumption of the local electrodynamics ( $\lambda_{\text{eff}} \gg \xi_0$ ) is justified in the superconducting state.<sup>4</sup>

<sup>4</sup>For the normal state, the mean-free-path  $l_{mfp} = v_F\tau$  and skin depth  $\delta$  should be compared to check for local electrodynamics. However, a fully quantitative determination of  $\tau$  requires  $Z_s(T)$  data well into the normal state (which requires a measurement in the hollow DR) and will not be discussed in this section.

Once the absolute value of the penetration depth is known, the normalized superfluid density can be calculated as  $\rho_s(T) = \lambda_{\text{eff}}^2(0)/\lambda_{\text{eff}}^2(T)$ . Its low temperature behavior gives information on the low energy excitations of the superconductor, which is sensitive to the pairing state [15]. If the pairing state is an eigenstate of the exchange operator, the pairing state can be either spin-singlet or spin-triplet. The spin-singlet pairing state scenario cannot explain our penetration depth data. Our penetration depth data shows a quadratic temperature dependence. For the singlet pairing states to show the quadratic temperature dependence, the possible cases are a  $d_{x^2-y^2}$  pairing state in the dirty limit [185], or the nonlocal electrodynamics regime [186]. In both of these cases, the low temperature behavior of the penetration depth shows a quadratic behavior below a crossover temperature  $T^*$  and shows a linear behavior above  $T^*$ . This crossover behavior can be expressed as [185, 186],

$$\Delta\lambda_{\text{eff}}(T) = \alpha \frac{T^2}{T + T^*}. \quad (8.1)$$

The possibility of the dirty  $d$ -wave scenario can be examined by checking the value of  $T^*$ . If one fits the penetration depth data of samples S1 and S2 with the above expression, one obtains  $T_{\text{impurity}}^* \geq 2.96T_c$  for both samples.  $T_{\text{impurity}}^*$  can be converted to the impurity scattering rate  $\Gamma \simeq (k_B T_{\text{impurity}}^*)^2 / (0.83^2 \Delta(0))$  [15]. If one assumes  $\Delta(0) = 2.14k_B T_c$ , which is valid for a typical weakly coupled BCS  $d_{x^2-y^2}$  state, one obtains  $\Gamma \geq 5.96k_B T_c$ . This impurity scattering rate is much larger than the critical temperature which is inconsistent with the presence of a robust superconducting state. Therefore, the dirty limit  $d_{x^2-y^2}$  pairing scenario is inconsistent to our data. The

nonlocal electrodynamics scenario can be disregarded considering the large  $T^*$  value found above and the established  $\lambda_{\text{eff}} \gg \xi_0$  relation. Also singlet states cannot explain the reported upper critical field  $H_{c2}$  which is larger than the paramagnetic limiting field [170]. Thus, only the spin-triplet pairing states are discussed below.

For a spin-triplet pairing state,  $\rho_s(T)$  follows different theoretical low temperature<sup>5</sup> behaviors  $\rho_s(T) = 1 - a(k_B T / \Delta_0(0))^n$  depending on two factors which determine the value of  $a$  and  $n$ . One is whether the magnitude of the energy gap  $|\Delta(\hat{\mathbf{k}}, T)|$  follows that of an axial state with point nodes  $\Delta_0(T)|\hat{\mathbf{k}} \times \hat{\mathbf{I}}|$  (Fig. 8.7(a)) or a polar state with a line node  $\Delta_0(T)|\hat{\mathbf{k}} \cdot \hat{\mathbf{I}}|$  (Fig. 8.7(b)). Here,  $\hat{\mathbf{k}}$  is the wave vector of an electron and  $\hat{\mathbf{I}}$  is the symmetry axis of the gap (an axis around which the gap function is symmetric) (Fig. 8.7(a),(b)). The other is whether the vector potential direction  $\hat{\mathbf{A}}$  is parallel or perpendicular to  $\hat{\mathbf{I}}$  [12, 15]. Table 8.1 shows the theoretically calculated values of  $a$  and  $n$  for 4 different possibilities of various triplet states and current directions. Figure 8.7(c) shows fits of  $\rho_s(T)$  to the theoretical behavior of the various triplet pairing states classified in Table 8.1. Note that the resulting fit parameter  $\Delta_0(0)$  and the root-mean-square error  $\sigma_{RMS}$  of the fit for each classified case is also shown in Table 8.1. Apparently, the data follows the behavior of the axial pairing state with the direction of the current aligned to  $\hat{\mathbf{I}}$ . An axial pairing state with broken TRS is a chiral pairing state ( $\vec{d} \sim (k_x - ik_y)\hat{x} + i(k_x - ik_y)\hat{y}$ ), while the one with preserved TRS is a helical state ( $\vec{d} \sim k_x\hat{x} + k_y\hat{y}$ )<sup>6</sup> [168]. With the evidence of broken TRS

<sup>5</sup>Here, the low temperature region means  $T/T_c < 0.26$  where  $\Delta_0(T) \approx \Delta_0(0)$ , which makes the fitting procedure below much simpler.

<sup>6</sup>Unlike the usual convention, please be warned that the  $\hat{k}_z$  and  $\hat{z}$  directions are not necessarily aligned with the  $c$ -axis of the crystal. Here, they are aligned with the direction of point nodes, which is the symmetry axis of the gap  $\hat{\mathbf{I}}$ .

	relative orientation	a	n	$\Delta_0(0)/k_B T_c$	$\sigma_{RMS}$
Axial state	$\vec{I} \parallel \vec{A}$	$\pi^2$	2	1.991	$1.63 \times 10^{-3}$
	$\vec{I} \perp \vec{A}$	$7\pi^4/15$	4	0.672	$2.05 \times 10^{-2}$
Polar state	$\vec{I} \parallel \vec{A}$	$27\pi\zeta(3)/4$	3	0.956	$1.24 \times 10^{-2}$
	$\vec{I} \perp \vec{A}$	$3\pi \ln 2/2$	1	20.49	$1.70 \times 10^{-2}$

Table 8.1 (First four columns) Low temperature theoretical asymptotes of the normalized superfluid density  $\rho_s(T)$  for the various spin-triplet pairing states, and the relative direction between the symmetry axis of the gap  $\vec{I}$  and the direction of the vector potential  $\vec{A}$  (which is same as that of the current) [15]. (Last two columns) The results of fitting the  $\rho_s(T)$  data with the theoretical asymptotes of each scenario.

from Ref. [27], one can argue that  $\text{UTe}_2$  shows normalized superfluid density  $\rho_s(T)$  consistent with a chiral triplet pairing state. In addition, since the symmetry axis connects the two point nodes of the chiral pairing order parameter, and the measurement surveys the  $ab$ -plane electrodynamics, one can further conclude that the point nodes are located in the  $ab$ -plane. The low temperature asymptote of  $\rho_s(T)$  in this case is given as  $\rho_s(T) = 1 - \pi^2(k_B T/\Delta_0(0))^2$ . The fitting the  $\rho_s(T)$  data into the theoretical asymptotes with a fit parameter  $\Delta_0(0)$  (Fig. 8.7(c)) yields an estimate for the gap size  $\Delta_0(0) = 1.991 \pm 0.003k_B T_c \approx 0.275 \text{ meV}$ .<sup>7</sup> Note that a recent STM study [173] measures a similar gap size (0.25 meV).

<sup>7</sup>The error bar of the fit parameters (here and the rest of the chapter) is determined by a deviation of fit parameter from the estimated values which increases the root-mean-square error  $\sigma_{RMS}$  of the fit by 5 %.

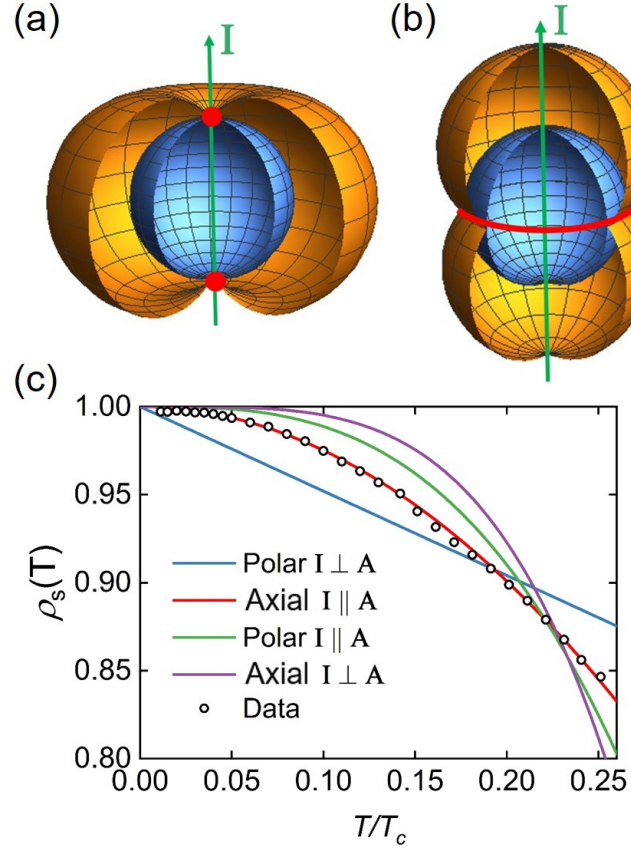


Fig. 8.7 (a) A schematic plot of the gap magnitude  $|\Delta(\vec{k})|$  (orange) and the Fermi surface (blue) in momentum space for the chiral triplet pairing state.  $\vec{I}$  represents the symmetry axis of the gap function (an axis around which the gap function is symmetric). Note that two point nodes (red) exist along the symmetry axis. (b) For the case of the polar state. A line node (red) exists along the equatorial plane. (c) Low temperature behavior of the normalized superfluid density  $\rho_s(T)$  in  $\text{UTe}_2$  with best fits for various triplet pairing states, and relative direction between the symmetry axis  $\vec{I}$  and the vector potential  $\vec{A}$  (The values of the fitting parameter and root-mean-square error can be found in Table. 8.1). Since  $\vec{I}$  connects the two point nodes of the gap of the chiral pairing state and the measurement surveys the  $ab$ -plane electrodynamic, one can conclude that the point nodes are located in the  $ab$ -plane.

## 8.4 Discussion of the origin of residual normal fluid

### 8.4.1 Extrinsic origins

Our study shows evidence for a chiral triplet pairing state and a substantial amount of normal fluid in the ground state of  $\text{UTe}_2$ . Before attributing this residual normal fluid to an intrinsic origin, one must first examine the possibilities of an extrinsic origin. One of the possible extrinsic origins would be a large impurity scattering rate  $\Gamma$  of the *bulk* superfluid, which will lead to *bulk* normal fluid. However, if one fits the temperature dependence of the normalized superfluid density into the modified theoretical asymptote for the chiral triplet state which considers impurity scattering rate  $\Gamma$  [12],

$$\rho_s(T) = 1 - \frac{1}{1 - 3 \frac{\Gamma}{\Delta_0(0)} \left( \frac{\pi}{2} \ln 2 - 1 \right)} \frac{\pi^2}{1 - \frac{\pi\Gamma}{2\Delta_0(0)}} \left( \frac{k_B T}{\Delta_0(0)} \right)^2, \quad (8.2)$$

one obtains  $\Gamma = 0.005 \pm 0.003 k_B T_c$  and  $\Delta_0(0) = 1.995 \pm 0.003 k_B T_c$  (Fig. 8.8(a)). This small impurity scattering rate is inconsistent with the impurity-induced normal fluid scenario.<sup>8</sup> Another possibility is a large number of quasiparticles excited by the microwave photons of the measurement signal. However, this scenario is also improbable because the energy to break and excite a Cooper pair to the normal state  $2\Delta_0(0) = 550 \mu\text{eV}$  ( $\Delta_0$  is the maximum energy gap) is much larger than that of the

---

<sup>8</sup>For an axial superconductor which has two point nodes, a theoretical calculation predicts  $\sigma_1(0)/\sigma_1(T_c) < 0.2$  (Ref. [187]) even with a larger impurity scattering rate  $\Gamma = 0.01$  (and with the same frequency-to-gap ratio  $\hbar\omega/\Delta_0(0) = 0.16$  used in our measurement). In our data,  $\sigma_1(0)/\sigma_1(T_c) = 1.25$  which cannot be explained by even the smaller  $\Gamma = 0.005$ .

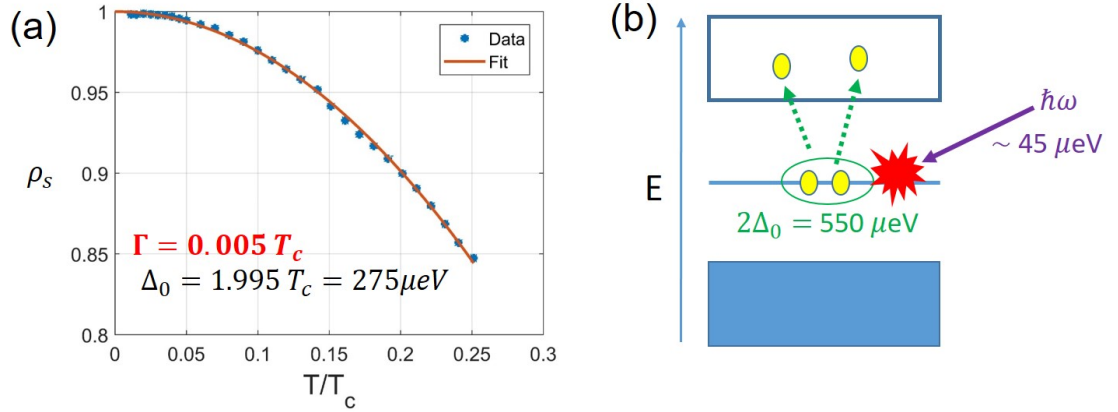


Fig. 8.8 Examination of possible extrinsic origins of residual normal fluid. (a) Scenario for the pair-breaking bulk impurity scattering rate  $\Gamma$  is examined. (b) Scenario for the pair-breaking energetic probing signal  $\hbar\omega$  is examined.

microwave photon  $E_{ph} = 45 \mu\text{eV}$  used here (Fig. 8.8(b)).

## 8.4.2 Intrinsic origins

With several candidates for extrinsic origin excluded, a possible intrinsic origin of the large residual normal fluid response is surface Majorana arc states predicted for a Weyl superconductor, which is a chiral superconductor with topologically non-trivial point nodes [17, 169]. This scenario is supported by several pieces of evidence. The chiral pairing state and the existence of point nodes are supported by evidence of an axial pairing state with point nodes from the superfluid density analysis (Sec. 8.3.3), and the evidence of broken time-reversal symmetry from the polar Kerr rotation and specific heat measurement [27] (an axial state with broken time-reversal symmetry is a chiral state). Recently, the results from a bulk thermal conductivity measurement in  $\text{UTe}_2$  [172] reveals the absence of a residual linear term as a function of tempera-

ture in the thermal conductivity, implying the absence of residual normal carriers, in the *bulk*. This suggests the residual normal fluid response observed in the microwave conductivity study should originate from the *surface*, consistent with the scenario of surface Majorana arc states of a Weyl superconductor. Later, the existence of the surface states is further supported by evidence of surface chiral in-gap density of states from STM studies of  $\text{UTe}_2$  [173]. In the future when superconducting  $\text{UTe}_2$  thin film growth is available, it will be interesting to see the thickness dependence of  $\tilde{\sigma}(T)$  near the magnetic penetration depth, which will allow us to quantitatively isolate and estimate the conductivity and dissipation of the surface state.

## 8.5 Issues and future plans

### 8.5.1 Quantitative estimation of the scattering life time

Although the above results and analysis done with the disk DR are qualitatively correct, if one wants to make the results quantitatively meaningful, the issue mentioned in the last paragraph of Sec. 8.2.2 needs to be resolved. For a recap, the issue is that the disk DR is not designed to test the sample properties above 2.5 K, whereas to obtain the exact absolute value of  $X_s(T)$  one needs to keep increasing the sample temperature until  $dR_s/dT = dX_s/dT$  is shown for more than a several Kelvin interval (Sec. 6.2.3). Determining the exact absolute value of  $X_s$  will lead to the exact estimation of the complex conductivity  $\tilde{\sigma}$  and normal state scattering life time  $\tau_n$ . With  $\tau_n$ ,

the assumption of local electrodynamics can be confirmed by comparison between the mean free path  $l_{mfp} = v_F \tau_n$  and skin depth  $\delta = 2R_s/\omega\mu_0$  in the normal state.

## 8.5.2 Microwave impedance measurement in the first generation hollow DR

To address the above issue, the first generation hollow DR setup was built (Sec. 6.3.2). By replacing the niobium top plate with copper, this resonator design allows the system to reach more than 20 K where the  $dR_s/dT = dX_s/dT$  regime in  $\text{UTe}_2$  is expected to be achieved. Also, to eliminate a possible effect from surface oxidization of  $\text{UTe}_2$ , the sample used in this measurement (S3) was polished, encapsulated, and mounted in the resonator within a nitrogen filled glove bag (Sec. 8.2.1). The sample quality factor is obtained by the subtraction of background dissipation (using Eq. (6.33)) [81].

Figure 8.9 shows the  $Z_s(T)$  obtained from sample S3 in the first generation hollow DR in the  $\text{TE}_{023}$  mode (7.12 GHz) with  $P_{in} = -30$  dBm. Again, the sample shows a large residual resistance in the zero temperature limit ( $R_s(0)/R_n(T_c) = 0.094$ ), consistent with previous results. The  $R_s(T)$  and  $X_s(T)$  curves were matched at 9 K and indeed share the same slope for a 3 K interval (7 to 10 K), but the curves diverge from each other above 10 K. The downturn in  $X_s(T)$  above 10 K is due to a background effect from the temperature-dependent dielectric constant of the hollow rutile, which shows a sharp decrease above 10 K (Fig. 6.6 and Sec. 6.3.2).

To eliminate the background temperature dependence, a second generation hol-

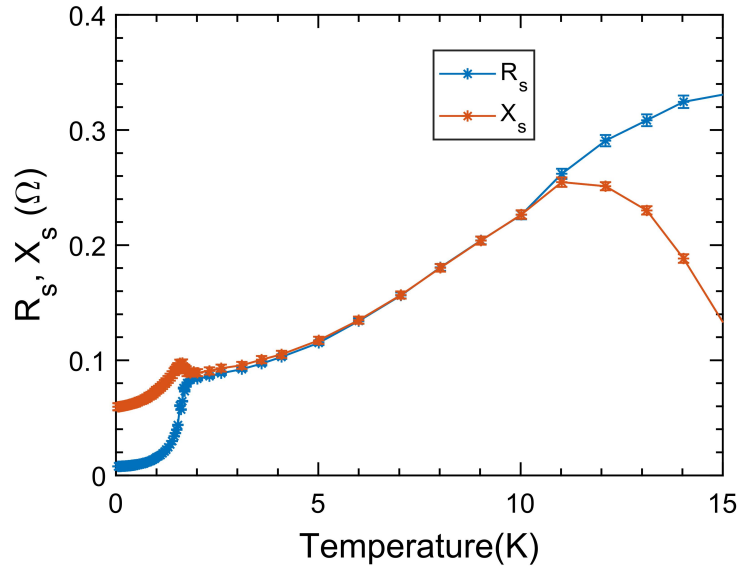


Fig. 8.9 Measured surface impedance from  $\text{UTe}_2$  sample S3 in the first generation hollow DR in the  $\text{TE}_{023}$  mode (7.12 GHz) up to 15 K. The large residual resistance  $R_s(0)$  was still observed. The  $R_s(T)$  and  $X_s(T)$  curves are matched at 9 K to convert  $\Delta X_s(T)$  to  $X_s(T)$ . The two curves shows similar slope from 7 to 10 K but diverge above 10 K due to a background temperature dependence in the rutile.

low DR was designed (Sec. 6.3.3). The new design will fix the temperature of the resonator while independently varying the temperature of the sample with a hot finger technique (Fig. 6.9) [110]. The resonator will also decrease the cavity wall dissipation by enlarging the cavity size, which will yield better accuracy in determining the surface resistance  $R_s$  of the sample. The new design is under construction and soon will deliver quantitatively rigorous  $Z_s(T)$  data of  $\text{UTe}_2$ .

## 8.6 Summary

In this chapter, a microwave surface impedance study is introduced on the TRS breaking superconductor  $\text{UTe}_2$ . The study revealed evidence of the existence of a residual normal fluid in this system through an analysis of the real part of the complex conductivity. The study also revealed the chiral spin-triplet pairing state with point nodes in the  $ab$ -plane from an analysis of the imaginary part of the complex conductivity. Together with the apparent absence of bulk normal fluid from the thermal conductivity study [172], the revealed pairing state, nodal structure, and presence of the residual normal fluid in this study further supports the possibility of Weyl superconductivity in  $\text{UTe}_2$ . A rigorous quantitative analysis will follow with measurements done with the next generation resonator design.

# CHAPTER 9

---

## Conclusion

---

In this thesis, microwave studies of various unconventional superconducting systems are introduced and their versatility is demonstrated. For discovering unconventional superconductors of various pairing states, the laser scanning microscopy photoreponse technique (LSM-PR) (Chap. 2) is introduced as a new method to "directly image" their gap nodal structure (Chap. 3). The performance of the technique is demonstrated in a patterned YBCO thin film, which is a representative  $d_{x^2-y^2}$  superconductor. The new technique has advantages which complement pre-existing methods in a way that does not require a pristine sample surface under ultra high vacuum nor complicated signal processing to interpret the data. The technique is not only sensitive to the bulk response of the sample but it is also able to study the response and underlying physics of exotic surface zero-energy bound states such as the Andreev bound state (Chap. 4). Finally, an improved design of LSM-PR gap spectroscopy was introduced (Chap. 5) to extend the applicability of the technique to samples without a patterning procedure. This will enable a newly discovered material to be examined at an earlier stage of its development. However, there is still room for further improve-

ment in the design. The LSM-PR gap spectroscopy would have greater impact if its applicability could be extended to sub-mm size single crystals, since that is the form which most of the new superconducting materials first appear. A potential design is depicted in Fig. 5.8, which provides a rotating linear excitation at a local spot of the crystal.

For unconventional superconductors with non-trivial topology, an extended version of microwave surface impedance spectroscopy is introduced (Chap. 6) and employed (Chap. 7, 8). The technique investigates the properties of the topologically non-trivial pairing states and/or properties of the consequent boundary states. For the artificial topological superconductor (TSC)  $\text{SmB}_6/\text{YB}_6$  bilayer, the characteristic length scales of the proximity coupled topological surface states are determined, which inform the design of a vortex Majorana device out of this system. For the candidate intrinsic TSC  $\text{UTe}_2$ , the chiral spin-triplet pairing state with point nodes and evidence for residual normal fluid are identified, elevating the system to one of the most promising candidates for a Weyl superconductor.

The next step of the described microwave studies would include testing other interesting candidate unconventional superconductors such as  $\text{YPtBi}$  [188],  $\text{URh}_2\text{Si}_2$  [189], and so on, whose pairing symmetry and topology are not yet known. It is also important and interesting to study these candidate unconventional superconductors in extreme conditions such as high magnetic field and pressure, where a new quantum phase of matter may emerge [171, 190].

# APPENDIX A

---

## Further details on the electromagnetic screening model

---

### A.1 Boundary conditions

Although explained in detail in Ref. [115], for the reader's convenience, the equation and the boundary conditions for the magnetic field inside a proximity-coupled bilayer, whose geometry is shown in Fig. 7.2(a), are described below. First, by combining Maxwell's equations with London's equation, one can obtain an equation for the tangential magnetic field for the bilayer

$$\frac{d^2 H(z)}{dz^2} + \frac{2}{\lambda_{N,S}(z)} \frac{d\lambda_{N,S}(z)}{dz} \frac{dH(z)}{dz} - \frac{1}{\lambda_{N,S}^2(z)} H(z) = 0. \quad (\text{A.1})$$

The boundary conditions for the tangential magnetic field are as follows,

$$H(d_N) = H_0, \text{ (top surface)} \quad (\text{A.2})$$

$$H(-d_S) = 0, \text{ (bottom surface)} \quad (\text{A.3})$$

$$H(0^+) = H(0^-), \text{ (interface)} \quad (\text{A.4})$$

$$\lambda_N^2(0, T) \frac{dH(z)}{dz} \Big|_{z=0^+} = \lambda_S^2(0, T) \frac{dH(z)}{dz} \Big|_{z=0^-}, \quad (\text{A.5})$$

where  $d_N \leq t_{smB_6}$  is the proximity-coupled thickness of the normal layer and  $d_S = t_{YB_6}$  is the thickness of the parent superconductor. The last boundary condition is a continuity condition for the superfluid velocity at the interface.

## A.2 Field solutions

With Eq.(A.1) and the approximated spatial profile of the induced order parameter in the normal layer  $\Delta_N(z, T) = \Delta_N(0, T)e^{-z/\xi(T)}$  and the normal penetration depth  $\lambda_N(z, T) = \lambda_N(0, T)e^{+z/\xi_N(T)}$ , one can obtain the spatial profile of the magnetic field in the normal and superconducting layer as follows [115]:

$$H_N(z, T) = ApI_1(p) + BpK_1(p), \text{ ( } 0 \leq z \leq d_N \text{)} \quad (\text{A.6})$$

$$H_S(z, T) = Ce^{z/\lambda_S} + De^{-z/\lambda_S}, \text{ ( } -d_S \leq z \leq 0 \text{)}, \quad (\text{A.7})$$

Here, the parameter  $p$  is defined as  $p(z, T) = (\xi_N(T)/\lambda_N(z, T))e^{-z/\xi_N(T)}$  and  $I_1, K_1$  are the modified Bessel functions of the first, second kind. The coefficients  $A, B, C, D$  can be calculated using the boundary conditions. The corresponding spatial profile of the current density can be obtained from  $z$  derivative of the magnetic field profile. After all the coefficients are obtained, the spatial profiles of the magnetic field and the current density of a normal/superconductor bilayer are fully determined. When calculating the inductance, the microwave loss is ignored so that the supercurrent density of the bilayer is approximated as the total current density  $J_s \simeq J$ . This is a valid approximation since the temperature range of the measurement ( $0 \sim 1.6$  K) is well below  $T_c$  of the bilayer ( $\sim 5.86$  K) and the microwave photon energy ( $\sim 0.044$  meV) is much lower than the zero temperature superconducting gap of the  $\text{YB}_6$  ( $> 1$  meV) [142].

---

## Bibliography

---

- [1] J. Bardeen, L. N. Cooper, and J. R. Schrieffer, “Microscopic theory of superconductivity,” *Phys. Rev.* **106**, 162 (1957) (cited on p. 1).
- [2] F. Steglich, J. Aarts, C. D. Bredl, W. Lieke, D. Meschede, W. Franz, and H. Schäfer, “Superconductivity in the Presence of Strong Pauli Paramagnetism:  $\text{CeCu}_2\text{Si}_2$ ,” *Phys. Rev. Lett.* **43**, 1892 (1979) (cited on p. 2).
- [3] H. R. Ott, H. Rudigier, Z. Fisk, and J. L. Smith, “ $\text{UBe}_{13}$ : An Unconventional Actinide Superconductor,” *Phys. Rev. Lett.* **50**, 1595 (1983) (cited on p. 2).
- [4] J. G. Bednorz and K. A. Müller, “Possible High- $T_c$  Superconductivity in the Ba-La-Cu-O System,” *Zeitschrift Fur Physik B-Condensed Matter* **64**, 189 (1986) (cited on p. 2).
- [5] M. K. Wu, J. R. Ashburn, C. J. Torng, P. H. Hor, R. L. Meng, L. Gao, Z. J. Huang, Y. Q. Wang, and C. W. Chu, “Superconductivity at 93 K in a new mixed-phase Y-Ba-Cu-O compound system at ambient pressure,” *Phys. Rev. Lett.* **58**, 908 (1987) (cited on p. 2).
- [6] S. Sanna, G. Allodi, G. Concas, A. D. Hillier, and R. D. Renzi, “Nanoscopic Coexistence of Magnetism and Superconductivity in  $\text{YBa}_2\text{Cu}_3\text{O}_{6+x}$  Detected by Muon Spin Rotation,” *Phys. Rev. Lett.* **93**, 207001 (2004) (cited on p. 2).

- [7] Z.-X. Shen, D. S. Dessau, B. O. Wells, D. M. King, W. E. Spicer, A. J. Arko, D. Marshall, L. W. Lombardo, A. Kapitulnik, P. Dickinson, S. Doniach, J. DiCarlo, T. Loeser, and C. H. Park, “Anomalously large gap anisotropy in the a-b plane of  $\text{Bi}_2\text{Sr}_2\text{CaCu}_2\text{O}_{8+\delta}$ ,” *Phys. Rev. Lett.* **70**, 1553 (1993) (cited on pp. 3, 10, 24, 26).
- [8] T. P. Devereaux, D. Einzel, B. Stadlober, R. Hackl, D. H. Leach, and J. J. Neumeier, “Electronic Raman scattering in high- $T_c$  superconductors: A probe of  $d_{x^2-y^2}$  pairing,” *Phys. Rev. Lett.* **72**, 396 (1994) (cited on pp. 3, 24, 26).
- [9] D. J. Van Harlingen, “Phase-sensitive tests of the symmetry of the pairing state in the high-temperature superconductors—Evidence for  $d_{x^2-y^2}$  symmetry,” *Rev. Mod. Phys.* **67**, 515 (1995) (cited on pp. 3, 24, 26).
- [10] R. J. Ormeno, A. Sibley, C. E. Gough, S. Sebastian, and I. R. Fisher, “Microwave Conductivity and Penetration Depth in the Heavy Fermion Superconductor  $\text{CeCoIn}_5$ ,” *Phys. Rev. Lett.* **88**, 047005 (2002) (cited on pp. 3, 75, 79, 101, 120).
- [11] M. P. Allan, F. Masee, D. K. Morr, J. Van Dyke, A. W. Rost, A. P. Mackenzie, C. Petrovic, and J. C. Davis, “Imaging Cooper pairing of heavy fermions in  $\text{CeCoIn}_5$ ,” *Nat. Phys.* **9**, 468 (2013) (cited on pp. 3, 75).
- [12] F. Gross, B. S. Chandrasekhar, D. Einzel, K. Andres, P. J. Hirschfeld, H. R. Ott, J. Beuers, Z. Fisk, and J. L. Smith, “Anomalous temperature dependence of the magnetic field penetration depth in superconducting  $\text{UBe}_{13}$ ,” *Z. Phys. B* **64**, 175 (1986) (cited on pp. 3, 136, 150, 153).

- [13] M. J. Graf, S.-K. Yip, J. A. Sauls, and D. Rainer, “Electronic thermal conductivity and the wiedemann-franz law for unconventional superconductors,” *Phys. Rev. B* **53**, 15147 (1996) (cited on p. 3).
- [14] C. C. Tsuei and J. R. Kirtley, “Pairing symmetry in cuprate superconductors,” *Rev. Mod. Phys.* **72**, 969 (2000) (cited on pp. 3, 23, 24).
- [15] R. Prozorov and R. W. Giannetta, “Magnetic penetration depth in unconventional superconductors,” *Supercond. Sci. Technol.* **19**, R41 (2006) (cited on pp. 3, 83, 97, 100, 120, 124, 149–151).
- [16] X.-L. Qi and S.-C. Zhang, “Topological insulators and superconductors,” *Rev. Mod. Phys.* **83**, 1057 (2011) (cited on p. 4).
- [17] M. Sato and Y. Ando, “Topological superconductors: a review,” *Rep. Prog. Phys.* **80**, 076501 (2017) (cited on pp. 4, 7, 136–138, 154).
- [18] A. P. Schnyder, S. Ryu, A. Furusaki, and A. W. W. Ludwig, “Classification of topological insulators and superconductors in three spatial dimensions,” *Phys. Rev. B* **78**, 195125 (2008) (cited on pp. 5, 7, 137).
- [19] M. Z. Hasan and C. L. Kane, “Colloquium: topological insulators,” *Rev. Mod. Phys.* **82**, 3045 (2010) (cited on p. 6).
- [20] D. Hsieh, D. Qian, L. Wray, Y. Xia, Y. S. Hor, R. J. Cava, and M. Z. Hasan, “A topological dirac insulator in a quantum spin hall phase,” *Nature* **452**, 970 (2008) (cited on p. 6).

- [21] Y. L. Chen, J. G. Analytis, J.-H. Chu, Z. K. Liu, S.-K. Mo, X. L. Qi, H. J. Zhang, D. H. Lu, X. Dai, Z. Fang, S. C. Zhang, I. R. Fisher, Z. Hussain, and Z.-X. Shen, “Experimental Realization of a Three-Dimensional Topological Insulator,  $\text{Bi}_2\text{Te}_3$ ,” [Science](#) **325**, 178 (2009) (cited on p. 6).
- [22] S.-Y. Xu, N. Alidoust, I. Belopolski, A. Richardella, C. Liu, M. Neupane, G. Bian, R. Huang Song-Hsunand Sankar, C. Fang, B. Dellabetta, W. Dai, Q. Li, M. J. Gilbert, F. Chou, N. Samarth, and M. Z. Hasan, “Momentum-space imaging of Cooper pairing in a half-Dirac-gas topological superconductor,” [Nat. Phys.](#) **10**, 943 (2014) (cited on pp. 6, 114, 127, 132–134).
- [23] N. Xu *et al.*, “Direct observation of the spin texture in  $\text{SmB}_6$  as evidence of the topological Kondo insulator,” [Nat. Commun.](#) **5**, 4566 (2014) (cited on pp. 6, 117).
- [24] Y. S. Eo, A. Rakoski, J. Lucien, D. Mihaliiov, Ç. Kurdak, P. F. S. Rosa, and Z. Fisk, “Transport gap in  $\text{SmB}_6$  protected against disorder,” [Proc. Natl. Acad. Sci. U.S.A](#) **116**, 12638 (2019) (cited on pp. 6, 117).
- [25] C. Kallin, “Chiral p-wave order in  $\text{Sr}_2\text{RuO}_4$ ,” [Rep. Prog. Phys.](#) **75** (2012) (cited on p. 7).
- [26] S. Bae, H. Kim, S. Ran, Y. S. Eo, I.-L. Liu, W. Fuhrman, J. Paglione, N. P. Butch, and S. M. Anlage, “Anomalous normal fluid response in a chiral superconductor,” [arXiv:1909.09032](#) (2019) (cited on pp. 7, 136).
- [27] I. M. Hayes, D. S. Wei, T. Metz, J. Zhang, Y. S. Eo, S. Ran, S. R. Saha, J. Collini, N. P. Butch, D. F. Agterberg, A. Kapitulnik, and J. Paglione, “Weyl Supercon-

- ductivity in  $\text{UTe}_2$ ,” [arXiv:2002.02539 \(2020\)](#) (cited on pp. 7, 136, 138, 140, 151, 154).
- [28] L. Fu and C. L. Kane, “Superconducting proximity effect and majorana fermions at the surface of a topological insulator,” [Phys. Rev. Lett. 100, 096407 \(2008\)](#) (cited on pp. 8, 113, 114, 124).
- [29] N. Read and D. Green, “Paired states of fermions in two dimensions with breaking of parity and time-reversal symmetries and the fractional quantum hall effect,” [Phys. Rev. B 61, 10267 \(2000\)](#) (cited on pp. 8, 113, 114).
- [30] H.-H. Sun, K.-W. Zhang, L.-H. Hu, C. Li, G.-Y. Wang, H.-Y. Ma, Z.-A. Xu, C.-L. Gao, D.-D. Guan, Y.-Y. Li, C. Liu, D. Qian, Y. Zhou, L. Fu, S.-C. Li, F.-C. Zhang, and J.-F. Jia, “Majorana zero mode detected with spin selective andreev reflection in the vortex of a topological superconductor,” [Phys. Rev. Lett. 116, 257003 \(2016\)](#) (cited on pp. 8, 113, 114).
- [31] R. Tao, Y.-J. Yan, X. Liu, Z.-W. Wang, Y. Ando, Q.-H. Wang, T. Zhang, and D.-L. Feng, “Direct Visualization of the Nematic Superconductivity in  $\text{Cu}_x\text{Bi}_2\text{Se}_3$ ,” [Phys. Rev. X 8, 041024 \(2018\)](#) (cited on p. 8).
- [32] P. Zhang, K. Yaji, T. Hashimoto, Y. Ota, T. Kondo, K. Okazaki, Z. Wang, J. Wen, G. D. Gu, H. Ding, and S. Shin, “Observation of topological superconductivity on the surface of an iron-based superconductor,” [Science 360, 182 \(2018\)](#) (cited on p. 8).

- [33] H. J. Chaloupka, “Microwave applications of high temperature superconductors,” in *Applications of superconductivity*, edited by H. Weinstock (Springer Netherlands, Dordrecht, 2000), pp. 295–383 (cited on p. 9).
- [34] W. D. Wise, M. C. Boyer, K. Chatterjee, T. Kondo, T. Takeuchi, H. Ikuta, Y. Wang, and E. W. Hudson, “Charge-density-wave origin of cuprate checkerboard visualized by scanning tunnelling microscopy,” *Nat. Phys.* **4**, 696 (2008) (cited on p. 10).
- [35] H. Kim, M. A. Tanatar, and R. Prozorov, “Tunnel diode resonator for precision magnetic susceptibility measurements in a mK temperature range and large DC magnetic fields,” *Rev. Sci. Instrum.* **89**, 094704 (2018) (cited on p. 10).
- [36] J. C. Culbertson, H. S. Newman, and C. Wilker, “Optical probe of microwave current distributions in high temperature superconducting transmission lines,” *J. Appl. Phys.* **84**, 2768 (1998) (cited on pp. 12, 14, 16, 50, 51, 144).
- [37] A. P. Zhuravel, A. G. Sivakov, O. G. Turutanov, A. N. Omelyanchouk, S. M. Anlage, A. Lukashenko, A. V. Ustinov, and D. Abraimov, “Laser scanning microscopy of hts films and devices (review article),” *Low. Temp. Phys* **32**, 592 (2006) (cited on pp. 12, 16).
- [38] S. Bae, Y. Tan, A. P. Zhuravel, L. Zhang, S. Zeng, Y. Liu, T. A. Lograsso, Ariando, T. Venkatesan, and S. M. Anlage, “Dielectric resonator method for determining gap symmetry of superconductors through anisotropic nonlinear meissner effect,” *Rev. Sci. Instrum.* **90**, 043901 (2019) (cited on pp. 12, 23, 29, 59, 61).

- [39] C. Kurter, A. P. Zhuravel, A. V. Ustinov, and S. M. Anlage, “Microscopic examination of hot spots giving rise to nonlinearity in superconducting resonators,” [Phys. Rev. B \*\*84\*\*, 104515 \(2011\)](#) (cited on p. 12).
- [40] D. Abraimov, D. M. Feldmann, A. A. Polyanskii, A. Gurevich, G. Daniels, D. C. Larbalestier, A. P. Zhuravel, and A. V. Ustinov, “Scanning laser imaging of dissipation in YBa<sub>2</sub>Cu<sub>3</sub>O<sub>7</sub>-coated conductors,” [Appl. Phys. Lett. \*\*85\*\*, 2568 \(2004\)](#) (cited on p. 12).
- [41] M. Tsindlekht, M. Golosovsky, H. Chayet, D. Davidov, and S. Chocron, “Frequency modulation of the superconducting parallel-plate microwave resonator by laser irradiation,” [Appl. Phys. Lett. \*\*65\*\*, 2875 \(1994\)](#) (cited on p. 13).
- [42] A. P. Zhuravel, S. M. Anlage, and A. V. Ustinov, “Measurement of local reactive and resistive photoresponse of a superconducting microwave device,” [Appl. Phys. Lett. \*\*88\*\*, 212503 \(2006\)](#) (cited on pp. 14, 16).
- [43] D. Xu, S. K. Yip, and J. A. Sauls, “Nonlinear Meissner effect in unconventional superconductors,” [Phys. Rev. B \*\*51\*\*, 16233 \(1995\)](#) (cited on pp. 23, 25).
- [44] T. Dahm and D. J. Scalapino, “Theory of intermodulation in a superconducting microstrip resonator,” [J. Appl. Phys. \*\*81\*\*, 2002 \(1997\)](#) (cited on pp. 23, 25, 28, 55).
- [45] D. E. Oates, S.-H. Park, and G. Koren, “Observation of the Nonlinear Meissner Effect in YBCO Thin Films: Evidence for a *d*-Wave Order Parameter in the Bulk of the Cuprate Superconductors,” [Phys. Rev. Lett. \*\*93\*\*, 197001 \(2004\)](#) (cited on pp. 23, 26).

- [46] C. Kurter, J. Abrahams, and S. M. Anlage, “Miniaturized superconducting metamaterials for radio frequencies,” [Appl. Phys. Lett. \*\*96\*\*, 253504 \(2010\)](#) (cited on pp. [23](#), [32](#)).
- [47] A. P. Zhuravel, B. G. Ghamsari, C. Kurter, P. Jung, S. Remillard, J. Abrahams, A. V. Lukashenko, A. V. Ustinov, and S. M. Anlage, “Imaging the Anisotropic Nonlinear Meissner Effect in Nodal  $\text{YBa}_2\text{Cu}_3\text{O}_{7-\delta}$  Thin-Film Superconductors,” [Phys. Rev. Lett. \*\*110\*\*, 087002 \(2013\)](#) (cited on pp. [23](#), [25](#), [26](#), [28](#), [32–36](#), [53](#), [73](#)).
- [48] M. Sigrist and K. Ueda, “Phenomenological theory of unconventional superconductivity,” [Rev. Mod. Phys. \*\*63\*\*, 239 \(1991\)](#) (cited on p. [24](#)).
- [49] H. Aubin, K. Behnia, M. Ribault, R. Gagnon, and L. Taillefer, “Angular Position of Nodes in the Superconducting Gap of YBCO,” [Phys. Rev. Lett. \*\*78\*\*, 2624 \(1997\)](#) (cited on p. [24](#)).
- [50] B. Revaz, J.-Y. Genoud, A. Junod, K. Neumaier, A. Erb, and E. Walker, “ $d$ -Wave Scaling Relations in the Mixed-State Specific Heat of  $\text{YBa}_2\text{Cu}_3\text{O}_7$ ,” [Phys. Rev. Lett. \*\*80\*\*, 3364 \(1998\)](#) (cited on pp. [24](#), [26](#)).
- [51] Y. Matsuda, K. Izawa, and I. Vekhter, “Nodal structure of unconventional superconductors probed by angle resolved thermal transport measurements,” [J. Phys. Condens. Matter \*\*18\*\*, R705 \(2006\)](#) (cited on p. [24](#)).
- [52] S. K. Yip and J. A. Sauls, “Nonlinear Meissner effect in CuO superconductors,” [Phys. Rev. Lett. \*\*69\*\*, 2264 \(1992\)](#) (cited on pp. [25](#), [48](#)).

- [53] T. Dahm and D. J. Scalapino, “Theory of microwave intermodulation in a high- $T_c$  superconducting microstrip resonator,” *Appl. Phys. Lett.* **69**, 4248 (1996) (cited on pp. 25, 27, 53, 68, 72).
- [54] A. P. Zhuravel, S. Bae, S. N. Shevchenko, A. N. Omelyanchouk, A. V. Lukashenko, A. V. Ustinov, and S. M. Anlage, “Imaging the paramagnetic nonlinear Meissner effect in nodal gap superconductors,” *Phys. Rev. B* **97**, 054504 (2018) (cited on pp. 25, 26, 34, 35, 55, 56, 73).
- [55] G. Benz, S. Wünsch, T. Scherer, M. Neuhaus, and W. Jutzi, “Measured temperature dependence of the intermodulation product of coplanar waveguides with s- and d-wave superconductors,” *Physica C: Superconductivity* **356**, 122 (2001) (cited on p. 26).
- [56] C.-R. Hu, “Midgap surface states as a novel signature for  $d_{x_a^2-x_b^2}$ -wave superconductivity,” *Phys. Rev. Lett.* **72**, 1526 (1994) (cited on pp. 34, 35, 40, 71, 73).
- [57] M. Aprili, E. Badica, and L. H. Greene, “Doppler Shift of the Andreev Bound States at the YBCO Surface,” *Phys. Rev. Lett.* **83**, 4630 (1999) (cited on pp. 34, 40).
- [58] T Löfwander, V. S. Shumeiko, and G Wendin, “Andreev bound states in high- $T_c$  superconducting junctions,” *Supercond. Sci. Technol* **14**, R53 (2001) (cited on pp. 34, 38, 39).
- [59] A. Carrington, F. Manzano, R. Prozorov, R. W. Giannetta, N. Kameda, and T. Tamegai, “Evidence for Surface Andreev Bound States in Cuprate Super-

- conductors from Penetration Depth Measurements,” [Phys. Rev. Lett. \*\*86\*\*, 1074 \(2001\)](#) (cited on pp. [34](#), [35](#), [42](#), [71](#), [73](#)).
- [60] Y. A. Kolesnichenko, A. N. Omelyanchouk, and S. N. Shevchenko, “Josephson and spontaneous currents at the interface between two d-wave superconductors with transport current in the banks,” [Low Temp. Phys \*\*30\*\*, 213 \(2004\)](#) (cited on pp. [34](#), [45](#), [46](#)).
- [61] A. Zare, T. Dahm, and N. Schopohl, “Strong surface contribution to the nonlinear meissner effect in *d*-wave superconductors,” [Phys. Rev. Lett. \*\*104\*\*, 237001 \(2010\)](#) (cited on pp. [34](#), [53](#), [54](#)).
- [62] H. Walter, W. Prusseit, R. Semerad, H. Kinder, W. Assmann, H. Huber, H. Burkhardt, D. Rainer, and J. A. Sauls, “Low-Temperature Anomaly in the Penetration Depth of  $\text{YBa}_2\text{Cu}_3\text{O}_7$  Films: Evidence for Andreev Bound States at Surfaces,” [Phys. Rev. Lett. \*\*80\*\*, 3598 \(1998\)](#) (cited on pp. [35](#), [42](#), [43](#), [71](#), [73](#)).
- [63] Y. Nagato and K. Nagai, “Surface and size effect of a  $d_{xy}$ -state superconductor,” [Phys. Rev. B \*\*51\*\*, 16254 \(1995\)](#) (cited on p. [37](#)).
- [64] L. J. Buchholtz, M. Palumbo, D. Rainer, and J. A. Sauls, “Thermodynamics of a d-wave superconductor near a surface,” [J. Low. Temp. Phys. \*\*101\*\*, 1079 \(1995\)](#) (cited on p. [37](#)).
- [65] W. K. Park and L. H. Greene, “Andreev reflection and order parameter symmetry in heavy-fermion superconductors: the case of  $\text{CeCoIn}_5$ ,” [J. Phys. Condens. Matter \*\*21\*\*, 103203 \(2009\)](#) (cited on p. [38](#)).

- [66] Y. Wang, W. Wan, R. Wang, F. Li, and G. Che, “Atomic configurations of twin boundaries and twinning dislocation in superconductor  $Y_{0.6}Na_{0.4}Ba_2Cu_{2.7}Zn_{0.3}O_{7-\delta}$ ,” [Philos. Mag. Lett.](#) **88**, 481 (2008) (cited on p. 44).
- [67] G. Eilenberger, “Transformation of Gorkov’s equation for type II superconductors into transport-like equations,” [Z. Physik](#) **214**, 195 (1968) (cited on p. 45).
- [68] W. Belzig, F. K. Wilhelm, C. Bruder, G. Schön, and A. D. Zaikin, “Quasiclassical green’s function approach to mesoscopic superconductivity,” [Superlattices and Microstructures](#) **25**, 1251 (1999) (cited on p. 45).
- [69] Y. Agassi, D. Oates, and B. Moeckly, “Measurement and modeling of the low-temperature penetration-depth anomaly in high-quality MgB2 thin films,” [Physica C: Superconductivity](#) **480**, 79 (2012) (cited on p. 45).
- [70] H. Bruus and K. Flensberg, “Many-body quantum theory in condensed matter physics,” in (Oxford University Press, Oxford, 2004), Ch9. Equation of motion theory (cited on p. 45).
- [71] Y. A. Kolesnichenko, A. N. Omelyanchouk, and S. N. Shevchenko, “Nonlocal mixing of supercurrents in josephson ballistic point contacts,” [Phys. Rev. B](#) **67**, 172504 (2003) (cited on p. 45).
- [72] S. N. Shevchenko, “Impact of the transport supercurrent on the density of states in the weak link,” [Phys. Rev. B](#) **74**, 172502 (2006) (cited on p. 45).
- [73] E. H. Rhoderick and E. M. Wilson, “Current distribution in thin superconducting films,” [Nature](#) **194**, 1167 (1962) (cited on p. 51).

- [74] E. J. Nicol and J. P. Carbotte, "Effect of gap suppression by superfluid current on the nonlinear microwave response of *d*-wave superconductors," [Phys. Rev. B \*\*73\*\*, 174510 \(2006\)](#) (cited on p. 53).
- [75] J. L. Tallon, C. Bernhard, U. Binniger, A. Hofer, G. V. M. Williams, E. J. Ansaldo, J. I. Budnick, and C. Niedermayer, "In-Plane Anisotropy of the Penetration Depth Due to Superconductivity on the Cu-O Chains in  $\text{YBa}_2\text{Cu}_3\text{O}_{7-\delta}$ ,  $\text{Y}_2\text{Ba}_4\text{Cu}_7\text{O}_{15-\delta}$ , and  $\text{YBa}_2\text{Cu}_4\text{O}_8$ ," [Phys. Rev. Lett. \*\*74\*\*, 1008 \(1995\)](#) (cited on p. 55).
- [76] B. W. Hakki and P. D. Coleman, "A dielectric resonator method of measuring inductive capacities in the millimeter range," [IRE Trans. Microwave Theory Tech. \*\*8\*\*, 402 \(1960\)](#) (cited on pp. 59, 60, 98, 100).
- [77] J. Mazierska and R. Grabovickic, "Circulating power, RF magnetic field, and RF current density of shielded dielectric resonators for power handling analysis of high-temperature superconducting thin films of arbitrary thickness," [IEEE Trans. Appl. Supercond. \*\*8\*\*, 178 \(1998\)](#) (cited on pp. 59, 60).
- [78] M. E. Tobar, J. Krupka, E. N. Ivanov, and R. A. Woode, "Anisotropic complex permittivity measurements of mono-crystalline rutile between 10 and 300 K," [J. Appl. Phys. \*\*83\*\*, 1604 \(1998\)](#) (cited on pp. 59, 63, 98, 105).
- [79] R. Shelby, J. Fontanella, and C. Andeen, "The low temperature electrical properties of some anisotropic crystals," [J. Phys. Chem. Solids \*\*41\*\*, 69 \(1980\)](#) (cited on p. 63).
- [80] M. E. Tobar, J. Krupka, J. G. Hartnett, E. N. Ivanov, and R. A. Woode, "High-Q sapphire-rutile frequency-temperature compensated microwave dielectric

- resonators,” [IEEE Trans. Ultrasonics, Ferroelectrics, and Frequency Control](#) **45**, [830 \(1998\)](#) (cited on p. [63](#)).
- [81] W. A. Huttema, B. Morgan, P. J. Turner, W. N. Hardy, X. Zhou, D. A. Bonn, R. Liang, and D. M. Broun, “Apparatus for high-resolution microwave spectroscopy in strong magnetic fields,” [Rev. Sci. Instrum.](#) **77**, [023901 \(2006\)](#) (cited on pp. [63](#), [79](#), [93](#), [101](#), [112](#), [156](#)).
- [82] E. S. Sabisky and H. J. Gerritsen, “Measurements of Dielectric Constant of Rutile (TiO<sub>2</sub>) at Microwave Frequencies between 4.2° and 300°K,” [J. Appl. Phys.](#) **33**, [1450 \(1962\)](#) (cited on p. [63](#)).
- [83] D. Kajfez, A. W. Glisson, and J. James, “Computed modal field distributions for isolated dielectric resonators,” [IEEE Trans. Microwave Theory Tech.](#) **32**, [1609 \(1984\)](#) (cited on p. [63](#)).
- [84] M. Macvicar and R. Rose, “Anisotropy of the niobium energy gap by a single crystal tunneling technique,” [Phys. Lett. A](#) **25**, [681 \(1967\)](#) (cited on p. [67](#)).
- [85] E. Hecht, *Optics* (Addison Wesley, San Francisco, 2002), p. 406 (cited on p. [69](#)).
- [86] R Gross and D Koelle, “Low temperature scanning electron microscopy of superconducting thin films and josephson junctions,” [Rep. Prog. Phys.](#) **57**, [651 \(1994\)](#) (cited on p. [70](#)).
- [87] J. Hartmann, P Voigt, and M. Reichling, “Measuring local thermal conductivity in polycrystalline diamond with a high resolution photothermal microscope,” [J. Appl. Phys.](#) **81**, [2966 \(1997\)](#) (cited on p. [70](#)).

- [88] J. Gao, J. Zmuidzinas, B. Mazin, P. Day, and H. Leduc, “Experimental study of the kinetic inductance fraction of superconducting coplanar waveguide,” [Nucl. Instrum. Methods Phys. Res. A](#) **559**, 585 (2006) (cited on p. 74).
- [89] M. A. Hein, *High-temperature superconductor thin films at microwave frequencies* (Springer, Heidelberg, 1999), pp. 45–46 (cited on pp. 74, 95).
- [90] C. J. S. Truncik, W. A. Huttema, P. J. Turner, S. Özcan, N. C. Murphy, P. R. Carrière, E. Thewalt, K. J. Morse, A. J. Koenig, J. L. Sarrao, and D. M. Broun, “Nodal quasiparticle dynamics in the heavy fermion superconductor CeCoIn<sub>5</sub> revealed by precision microwave spectroscopy,” [Nat. Commun.](#) **4**, 2477 (2013) (cited on pp. 75, 79, 101, 145–147).
- [91] H. Fukazawa, Y. Yamada, K. Kondo, T. Saito, Y. Kohori, K. Kuga, Y. Matsumoto, S. Nakatsuji, H. Kito, P. M. Shirage, K. Kihou, N. Takeshita, C.-H. Lee, A. Iyo, and H. Eisaki, “Possible Multiple Gap Superconductivity with Line Nodes in Heavily Hole-Doped Superconductor KFe<sub>2</sub>As<sub>2</sub> Studied by <sup>75</sup>As Nuclear Quadrupole Resonance and Specific Heat,” [J. Phys. Soc. Jpn](#) **78**, 083712 (2009) (cited on p. 75).
- [92] J.-P. Reid *et al.*, “From d-wave to s-wave pairing in the iron-pnictide superconductor (Ba,K)Fe<sub>2</sub>As<sub>2</sub>,” [Supercond. Sci. Technol.](#) **25**, 084013 (2012) (cited on p. 75).
- [93] H. Kim, M. A. Tanatar, Y. Liu, Z. C. Sims, C. Zhang, P. Dai, T. A. Lograsso, and R. Prozorov, “Evolution of London penetration depth with scattering in single crystals of K<sub>1-x</sub>Na<sub>x</sub>Fe<sub>2</sub>As<sub>2</sub>,” [Phys. Rev. B](#) **89**, 174519 (2014) (cited on p. 75).

- [94] Z. Frait, V. Kamberský, Z. M $\acute{A}$ lek, and M. Ondris, “Local variations of uniaxial anisotropy in thin films,” *Czechoslovakij fiziceskij zurnal B* **10**, 616 (1960) (cited on p. 77).
- [95] R. F. Soohoo, “A microwave magnetic microscope,” *J. Appl. Phys.* **33**, 1276 (1962) (cited on p. 77).
- [96] P. J. Petersan and S. M. Anlage, “Measurement of resonant frequency and quality factor of microwave resonators: comparison of methods,” *J. Appl. Phys.* **84**, 3392 (1998) (cited on pp. 79, 91).
- [97] R. J. Ormeno, M. A. Hein, T. L. Barraclough, A. Sibley, C. E. Gough, Z. Q. Mao, S. Nishizaki, and Y. Maeno, “Electrodynamic response of Sr<sub>2</sub>RuO<sub>4</sub>,” *Phys. Rev. B* **74**, 092504 (2006) (cited on pp. 79, 101).
- [98] D. A. Bonn and W. N. Hardy, “Microwave electrostatics of high temperature superconductors,” in *Handbook of high-temperature superconductivity: theory and experiment* (Springer New York, New York, NY, 2007), p. 147 (cited on pp. 79, 83).
- [99] X. Zhang, “Microwave flux-flow impedance measurements of type-II superconductors,” PhD dissertation (2008) (cited on pp. 79, 101, 103, 105).
- [100] J. Bardeen, “Two-Fluid Model of Superconductivity,” *Phys. Rev. Lett.* **1**, 399 (1958) (cited on p. 82).
- [101] D. J. Griffiths, *Introduction to Electrodynamics, 3rd Edition* (Pearson Benjamin Cummings, San Francisco, 2008), p. 394 (cited on p. 83).

- [102] J. C. Booth, D. H. Wu, and S. M. Anlage, “A broadband method for the measurement of the surface impedance of thin films at microwave frequencies,” [Rev. Sci. Instrum. 65, 2082 \(1994\)](#) (cited on p. 87).
- [103] K. Lai, M. B. Ji, N. Leindecker, M. A. Kelly, and Z. X. Shen, “Atomic-force-microscope-compatible near-field scanning microwave microscope with separated excitation and sensing probes,” [Rev. Sci. Instrum. 78, 063702 \(2007\)](#) (cited on p. 87).
- [104] G. L. Matthaei and G. L. Hey-Shipton, “Concerning the use of high-temperature superconductivity in planar microwave filters,” [IEEE Trans. Microw. Theory Tech 42, 1287 \(1994\)](#) (cited on p. 93).
- [105] G. Ghigo, D. Torsello, R. Gerbaldo, L. Gozzelino, F. Laviano, and T. Tamegai, “Effects of heavy-ion irradiation on the microwave surface impedance of  $(\text{Ba}_{1-x}\text{K}_x)\text{Fe}_2\text{As}_2$  single crystals,” [Supercond. Sci. Technol. 31, 34006 \(2018\)](#) (cited on p. 93).
- [106] M. A. Hein, R. J. Ormeno, and C. E. Gough, “High-frequency electrodynamic response of strongly anisotropic clean normal and superconducting metals,” [Phys. Rev. B 64, 024529 \(2001\)](#) (cited on p. 97).
- [107] P. Kneisel, G. R. Myneni, G. Ciovati, J. Sekutowicz, and T. Carneiro, “Preliminary Results From Single Crystal and Very Large Crystal Niobium Cavities,” in [Proceedings of the 2005 Particle Accelerator Conference](#) (2005), pp. 3991–3993 (cited on pp. 98, 99).
- [108] W. E. Nelson and A. R. Hoffman, “Measurements of the Temperatures and Magnetic Field Dependence of Electrical Resistivity and Thermal Conductivity

- in OFHC Copper,” in *Thermal conductivity 14*, edited by P. G. Klemens and T. K. Chu (Springer US, Boston, MA, 1976), pp. 73–80 (cited on p. 102).
- [109] A. N. Luiten, M. E. Tobar, J. Krupka, R. Woode, E. N. Ivanov, and A. G. Mann, “Microwave properties of a rutile resonator between 2 and 10 K,” *J. Phys. D.* **31**, 1383 (1998) (cited on p. 105).
- [110] D. L. Rubin, K. Green, J. Gruschus, J. Kirchgessner, D. Moffat, H. Padamsee, J. Sears, Q. S. Shu, L. F. Schneemeyer, and J. V. Waszczak, “Observation of a narrow superconducting transition at 6 GHz in crystals of  $\text{YBa}_2\text{Cu}_3\text{O}_7$ ,” *Phys. Rev. B* **38**, 6538 (1988) (cited on pp. 108, 157).
- [111] A. L. Woodcraft and A. Gray, “A low temperature thermal conductivity database,” *AIP Conference Proceedings* **1185**, 681 (2009) (cited on p. 108).
- [112] N. Murphy, “Microwave frequency vortex dynamics of the heavy fermion superconductor  $\text{CeCoIn}_5$ ,” MA thesis (2010) (cited on p. 110).
- [113] S. Bae, S. Lee, X. Zhang, I. Takeuchi, and S. M. Anlage, “Microwave meissner screening properties of proximity-coupled topological-insulator / superconductor bilayers,” *Phys. Rev. Materials* **3**, 124803 (2019) (cited on p. 113).
- [114] G. Deutscher and P. G. de Gennes, *Superconductivity*, Vol. 2 (Marcel Dekker, 1969), p. 1006 (cited on pp. 113, 115, 125).
- [115] M. S. Pambianchi, J. Mao, and S. M. Anlage, “Magnetic screening in proximity-coupled superconductor/normal-metal bilayers,” *Phys. Rev. B* **50**, 13659 (1994) (cited on pp. 113, 115, 121, 161, 162).

- [116] M. S. Pambianchi, L. Chen, and S. M. Anlage, “Complex conductivity of proximity-superconducting Nb/Cu bilayers,” *Phys. Rev. B* **54**, 3508 (1996) (cited on pp. 113, 115, 119, 121, 125).
- [117] P. G. de Gennes, *Superconductivity of Metals and Alloys* (Westview, 1999), p. 232 (cited on pp. 113, 115, 124).
- [118] S. Lee, V. Stanev, X. Zhang, J. Stasak Drewand Flowers, J. S. Higgins, S. Dai, T. Blum, X. Pan, V. M. Yakovenko, J. Paglione, R. L. Greene, V. Galitski, and I. Takeuchi, “Perfect Andreev reflection due to the Klein paradox in a topological superconducting state,” *Nature* **570**, 344 (2019) (cited on pp. 113, 117, 118, 127, 129).
- [119] J. Alicea, “New directions in the pursuit of majorana fermions in solid state systems,” *Rep. Prog. Phys.* **75**, 076501 (2012) (cited on p. 114).
- [120] C. Beenakker, “Search for majorana fermions in superconductors,” *Annu. Rev. Condens. Matter Phys* **4**, 113 (2013) (cited on p. 114).
- [121] A. Kitaev, “Anyons in an exactly solved model and beyond,” *Annals of Physics* **321**, 2 (2006) (cited on p. 114).
- [122] D. A. Ivanov, “Non-Abelian Statistics of Half-Quantum Vortices in  $p$ -Wave Superconductors,” *Phys. Rev. Lett.* **86**, 268 (2001) (cited on p. 114).
- [123] A. Stern, F. von Oppen, and E. Mariani, “Geometric phases and quantum entanglement as building blocks for non-abelian quasiparticle statistics,” *Phys. Rev. B* **70**, 205338 (2004) (cited on p. 114).

- [124] M. Stone and S.-B. Chung, “Fusion rules and vortices in  $p_x + ip_y$  superconductors,” *Phys. Rev. B* **73**, 014505 (2006) (cited on p. 114).
- [125] W. Dai, A. Richardella, R. Du, W. Zhao, X. Liu, C. X. Liu, S.-H. Huang, R. Sankar, F. Chou, N. Samarth, and Q. Li, “Proximity-effect-induced Superconducting Gap in Topological Surface States - A Point Contact Spectroscopy Study of NbSe<sub>2</sub>/Bi<sub>2</sub>Se<sub>3</sub> Superconductor - Topological Insulator Heterostructures,” *Sci. Rep.* **7**, 7631 (2017) (cited on p. 114).
- [126] M.-X. Wang, C. Liu, J.-P. Xu, F. Yang, L. Miao, M.-Y. Yao, C. L. Gao, C. Shen, X. Ma, X. Chen, Z.-A. Xu, Y. Liu, S.-C. Zhang, D. Qian, J.-F. Jia, and Q.-K. Xue, “The Coexistence of Superconductivity and Topological Order in the Bi<sub>2</sub>Se<sub>3</sub> Thin Films,” *Science* **336**, 52 (2012) (cited on p. 114).
- [127] J.-P. Xu, C. Liu, M.-X. Wang, J. Ge, Z.-L. Liu, X. Yang, Y. Chen, Y. Liu, Z.-A. Xu, C.-L. Gao, D. Qian, F.-C. Zhang, and J.-F. Jia, “Artificial Topological Superconductor by the Proximity Effect,” *Phys. Rev. Lett.* **112**, 217001 (2014) (cited on p. 114).
- [128] J.-P. Xu, M.-X. Wang, Z. L. Liu, J.-F. Ge, X. Yang, C. Liu, Z. A. Xu, D. Guan, C. L. Gao, D. Qian, Y. Liu, Q.-H. Wang, F.-C. Zhang, Q.-K. Xue, and J.-F. Jia, “Experimental Detection of a Majorana Mode in the core of a Magnetic Vortex inside a Topological Insulator-Superconductor Bi<sub>2</sub>Te<sub>3</sub>/NbSe<sub>2</sub> Heterostructure,” *Phys. Rev. Lett.* **114**, 017001 (2015) (cited on p. 114).
- [129] W. Belzig, C. Bruder, and G. Schön, “Diamagnetic response of normal-metal-superconductor double layers,” *Phys. Rev. B* **53**, 5727 (1996) (cited on p. 115).

- [130] J. Kim, Y.-J. Doh, K. Char, H. Doh, and H.-Y. Choi, “Proximity effect in NbAu/CoFe trilayers,” *Phys. Rev. B* **71**, 214519 (2005) (cited on p. 115).
- [131] J. R. Hook, “A method for calculating the microwave surface impedance of superconducting films,” *J. Low Temp. Phys.* **23**, 645 (1976) (cited on p. 115).
- [132] R. W. Simon and P. M. Chaikin, “Penetration depth in proximity-effect superconductors,” *Phys. Rev. B* **30**, 3750 (1984) (cited on p. 115).
- [133] K. Kanoda, H. Mazaki, N. Hosoi, and T. Shinjo, “Magnetic-field penetration depth and material parameters of V-Ag multilayered superconductors,” *Phys. Rev. B* **35**, 8413 (1987) (cited on p. 115).
- [134] A. C. Mota, P. Visani, and A. Pollini, “Magnetic properties of proximity-induced superconducting copper and silver,” *J. Low. Temp. Phys.* **76**, 465 (1989) (cited on pp. 115, 125).
- [135] J. H. Claassen, J. E. Evetts, R. E. Somekh, and Z. H. Barber, “Observation of the superconducting proximity effect from kinetic-inductance measurements,” *Phys. Rev. B* **44**, 9605 (1991) (cited on p. 115).
- [136] M. S. Pambianchi, S. N. Mao, and S. M. Anlage, “Microwave surface impedance of proximity-coupled Nb/Al bilayer films,” *Phys. Rev. B* **52**, 4477 (1995) (cited on pp. 115, 121, 125).
- [137] H. Onoe, A. Sumiyama, M. Nakagawa, and Y. Oda, “Superconducting Proximity Effect in Au of Au-Clad Nb Wire in the Clean Limit,” *J. Phys. Soc. Jpn.* **64**, 2138 (1995) (cited on pp. 115, 125).

- [138] M. S. Pambianchi, C. Kwon, T. Venkatesan, and S. M. Anlage, “Surface impedance of  $\text{YBa}_2\text{Cu}_3\text{O}_7/\text{Y}_{0.6}\text{Pr}_{0.4}\text{Ba}_2\text{Cu}_3\text{O}_7$  bilayers: Possible evidence for the proximity effect,” *Phys. Rev. B* **54**, 15513 (1996) (cited on pp. 115, 121, 125).
- [139] M. Cheng, R. M. Lutchyn, V. Galitski, and S. Das Sarma, “Tunneling of anyonic majorana excitations in topological superconductors,” *Phys. Rev. B* **82**, 094504 (2010) (cited on pp. 115, 133).
- [140] C. Kittel, *Introduction to Solid State Physics, 5th edition* (John Wiley and Sons, 2005), p. 268 (cited on p. 116).
- [141] B. Clayman and R. Frindt, “The superconducting energy gap of  $\text{NbSe}_2$ ,” *Solid State Commun.* **9**, 1881 (1971) (cited on p. 116).
- [142] R. Kadono, S. Kuroiwa, J. Akimitsu, A. Koda, K. Ohishi, W. Higemoto, and S. Otani, “Microscopic properties of vortex states in  $\text{YB}_6$  probed by muon spin rotation,” *Phys. Rev. B* **76**, 094501 (2007) (cited on pp. 116, 120, 124, 126, 163).
- [143] A. Menth, E. Buehler, and T. H. Geballe, “Magnetic and Semiconducting Properties of  $\text{SmB}_6$ ,” *Phys. Rev. Lett.* **22**, 295 (1969) (cited on p. 117).
- [144] P. Syers, D. Kim, M. S. Fuhrer, and J. Paglione, “Tuning Bulk and Surface Conduction in the Proposed Topological Kondo Insulator  $\text{SmB}_6$ ,” *Phys. Rev. Lett.* **114**, 096601 (2015) (cited on p. 117).
- [145] B. S. Tan, Y.-T. Hsu, B. Zeng, M. C. Hatnean, N. Harrison, Z. Zhu, M. Hartstein, M. Kiourlappou, A. Srivastava, M. D. Johannes, T. P. Murphy, J.-H. Park, L. Balicas, G. G. Lonzarich, G. Balakrishnan, and S. E. Sebastian, “Unconven-

- tional Fermi surface in an insulating state,” [Science](#) **349**, 287 (2015) (cited on p. 117).
- [146] N. J. Laurita, C. M. Morris, S. M. Koohpayeh, P. F. S. Rosa, W. A. Phelan, Z. Fisk, T. M. McQueen, and N. P. Armitage, “Anomalous three-dimensional bulk ac conduction within the Kondo gap of  $\text{SmB}_6$  single crystals,” [Phys. Rev. B](#) **94**, 165154 (2016) (cited on p. 117).
- [147] Y. Xu, S. Cui, J. K. Dong, D. Zhao, T. Wu, X. H. Chen, K. Sun, H. Yao, and S. Y. Li, “Bulk Fermi Surface of Charge-Neutral Excitations in  $\text{SmB}_6$  or Not: A Heat-Transport Study,” [Phys. Rev. Lett.](#) **116**, 246403 (2016) (cited on p. 117).
- [148] J. Zhang, J. Yong, I. Takeuchi, R. L. Greene, and R. D. Averitt, “Ultrafast terahertz spectroscopy study of a Kondo insulating thin-film  $\text{SmB}_6$ : Evidence for an emergent surface state,” [Phys. Rev. B](#) **97**, 155119 (2018) (cited on p. 117).
- [149] S. Lee, X. Zhang, Y. Liang, S. W. Fackler, J. Yong, X. Wang, J. Paglione, R. L. Greene, and I. Takeuchi, “Observation of the Superconducting Proximity Effect in the Surface State of  $\text{SmB}_6$  Thin Films,” [Phys. Rev. X](#) **6**, 031031 (2016) (cited on pp. 117, 118, 129, 130).
- [150] J. Yong, Y. Jiang, D. Usanmaz, S. Curtarolo, X. Zhang, L. Li, X. Pan, J. Shin, I. Takeuchi, and R. L. Greene, “Robust topological surface state in Kondo insulator  $\text{SmB}_6$  thin films,” [Appl. Phys. Lett.](#) **105**, 222403 (2014) (cited on p. 118).
- [151] N. Klein, U. Dähne, U. Poppe, N. Tellmann, K. Urban, S. Orbach, S. Hensen, G. Müller, and H. Piel, “Microwave surface resistance of epitaxial  $\text{YBa}_2\text{Cu}_3\text{O}_7$

- thin films at 18.7 GHz measured by a dielectric resonator technique,” [J. Super. 5, 195 \(1992\)](#) (cited on p. 120).
- [152] B. B. Jin, N. Klein, W. N. Kang, H.-J. Kim, E.-M. Choi, S.-I. Lee, T. Dahm, and K. Maki, “Energy gap, penetration depth, and surface resistance of MgB<sub>2</sub> thin films determined by microwave resonator measurements,” [Phys. Rev. B 66, 104521 \(2002\)](#) (cited on p. 120).
- [153] A. A. Abrikosov, *Fundamentals of the Theory of Metals* (Amsterdam: Elsevier, 1988), p. 364 (cited on pp. 120, 124).
- [154] M. I. Tsindlekht, V. M. Genkin, G. I. Leviev, I. Felner, O. Yuli, I. Asulin, O. Millo, M. A. Belogolovskii, and N. Y. Shitsevalova, “Linear and nonlinear low-frequency electrodynamics of surface superconducting states in an yttrium hexaboride single crystal,” [Phys. Rev. B 78, 024522 \(2008\)](#) (cited on pp. 120, 124).
- [155] N. E. Sluchanko, V. V. Glushkov, B. P. Gorshunov, S. V. Demishev, M. V. Kondrin, A. A. Pronin, A. A. Volkov, A. K. Savchenko, G. Grüner, Y. Bruynseraede, V. V. Moshchalkov, and S. Kunii, “Intragap states in SmB<sub>6</sub>,” [Phys. Rev. B 61, 9906 \(2000\)](#) (cited on p. 124).
- [156] G. Deutscher, J. Hurault, and P. van Dalen, “Electrodynamical properties of superconducting contacts,” [J. Phys. Chem. Solids. 30, 509 \(1969\)](#) (cited on p. 124).

- [157] R. W. Simon and P. M. Chaikin, “Josephson tunneling studies of magnetic screening in proximity-superconducting silver,” *Phys. Rev. B* **23**, 4463 (1981) (cited on p. 124).
- [158] D. S. Falk, “Superconductors with Plane Boundaries,” *Phys. Rev.* **132**, 1576 (1963) (cited on p. 125).
- [159] N. Sluchanko, V. Glushkov, S. Demishev, A. Azarevich, M. Anisimov, A. Bogach, V. Voronov, S. Gavrilkin, K. Mitsen, A. Kuznetsov, I. Sannikov, N. Shitsevalova, V. Filipov, M. Kondrin, S. Gabáni, and K. Flachbart, “Lattice instability and enhancement of superconductivity in  $\text{YB}_6$ ,” *Phys. Rev. B* **96**, 144501 (2017) (cited on p. 126).
- [160] M. Tinkham, *Introduction to Superconductivity, 2nd edition* (Dover publications, Inc., 1996), p. 97 (cited on pp. 126, 133).
- [161] H. Pirie, Y. Liu, A. Soumyanarayanan, P. Chen, Y. He, M. M. Yee, P. F. S. Rosa, J. D. Thompson, D.-J. Kim, Z. Fisk, X. Wang, J. Paglione, D. K. Morr, M. H. Hamidian, and J. E. Hoffman, “Imaging emergent heavy Dirac fermions of a topological Kondo insulator,” *Nat. Phys.* **16**, 52 (2020) (cited on pp. 129, 130).
- [162] C. E. Matt, H. Pirie, A. Soumyanarayanan, Y. He, M. M. Yee, P. Chen, Y. Liu, D. T. Larson, W. S. Paz, J. J. Palacios, M. H. Hamidian, and J. E. Hoffman, “Consistency between ARPES and STM measurements on  $\text{SmB}_6$ ,” *Phys. Rev. B* **101**, 085142 (2020) (cited on p. 129).
- [163] V. Alexandrov, P. Coleman, and O. Erten, “Kondo Breakdown in Topological Kondo Insulators,” *Phys. Rev. Lett.* **114**, 177202 (2015) (cited on p. 129).

- [164] M. Neupane, N. Alidoust, S.-Y. Xu, T. Kondo, Y. Ishida, D. J. Kim, C. Liu, I. Belopolski, Y. J. Jo, T.-R. Chang, H.-T. Jeng, T. Durakiewicz, L. Balicas, H. Lin, A. Bansil, S. Shin, Z. Fisk, and M. Z. Hasan, “Surface electronic structure of the topological Kondo-insulator candidate correlated electron system  $\text{SmB}_6$ ,” [Nat. Commun. 4, 2991 \(2013\)](#) (cited on p. 130).
- [165] J. Jiang, S. Li, T. Zhang, Z. Sun, F. Chen, Z. R. Ye, M. Xu, Q. Q. Ge, S. Y. Tan, X. H. Niu, M. Xia, B. P. Xie, Y. F. Li, X. H. Chen, H. H. Wen, and D. L. Feng, “Observation of possible topological in-gap surface states in the Kondo insulator  $\text{SmB}_6$  by photoemission,” [Nat. Commun. 4, 3010 \(2013\)](#) (cited on p. 130).
- [166] B. Roy, J. D. Sau, M. Dzero, and V. Galitski, “Surface theory of a family of topological Kondo insulators,” [Phys. Rev. B 90, 155314 \(2014\)](#) (cited on p. 130).
- [167] T. Liu, Y. Li, L. Gu, J. Ding, H. Chang, P. A. P. Janantha, B. Kalinikos, V. Novosad, A. Hoffmann, R. Wu, C. L. Chien, and M. Wu, “Nontrivial Nature and Penetration Depth of Topological Surface States in  $\text{SmB}_6$  Thin Films,” [Phys. Rev. Lett. 120, 207206 \(2018\)](#) (cited on p. 130).
- [168] C. Kallin and J. Berlinsky, “Chiral superconductors,” [Rep. Prog. Phys. 79, 054502 \(2016\)](#) (cited on pp. 136, 137, 150).
- [169] V. Kozii, J. W. F. Venderbos, and L. Fu, “Three-dimensional majorana fermions in chiral superconductors,” [Sci. Adv. 2, e1601835 \(2016\)](#) (cited on pp. 136–138, 154).
- [170] S. Ran, C. Eckberg, Q.-P. Ding, Y. Furukawa, T. Metz, S. R. Saha, I.-L. Liu, M. Zic, H. Kim, J. Paglione, and N. P. Butch, “Nearly ferromagnetic spin-triplet

- superconductivity,” [Science](#) **365**, 684 (2019) (cited on pp. [136](#), [138](#), [141](#), [148](#), [150](#)).
- [171] S. Ran, I. L. Liu, Y. S. Eo, D. J. Campbell, P. M. Neves, W. T. Fuhrman, S. R. Saha, C. Eckberg, H. Kim, D. Graf, F. Balakirev, J. Singleton, J. Paglione, and N. P. Butch, “Extreme magnetic field-boosted superconductivity,” [Nat. Phys.](#) **15**, 1250 (2019) (cited on pp. [136](#), [160](#)).
- [172] T. Metz, S. Bae, S. Ran, I.-L. Liu, Y. S. Eo, W. T. Fuhrman, D. F. Agterberg, S. M. Anlage, N. P. Butch, and J. Paglione, “Point-node gap structure of the spin-triplet superconductor  $UTe_2$ ,” [Phys. Rev. B](#) **100**, 220504 (2019) (cited on pp. [136](#), [147](#), [148](#), [154](#), [158](#)).
- [173] L. Jiao, S. Howard, S. Ran, Z. Wang, J. O. Rodriguez, M. Sgrist, Z. Wang, N. P. Butch, and V. Madhavan, “Chiral superconductivity in heavy-fermion metal  $UTe_2$ ,” [Nature](#) **579**, 523 (2020) (cited on pp. [136](#), [151](#), [155](#)).
- [174] S. Kashiwaya, H. Kashiwaya, H. Kambara, T. Furuta, H. Yaguchi, Y. Tanaka, and Y. Maeno, “Edge States of  $Sr_2RuO_4$  Detected by In-Plane Tunneling Spectroscopy,” [Phys. Rev. Lett.](#) **107**, 077003 (2011) (cited on p. [137](#)).
- [175] S. Sasaki, Z. Ren, A. A. Taskin, K. Segawa, L. Fu, and Y. Ando, “Odd-parity pairing and topological superconductivity in a strongly spin-orbit coupled semiconductor,” [Phys. Rev. Lett.](#) **109**, 217004 (2012) (cited on p. [137](#)).
- [176] A. Kapitulnik, J. Xia, E. Schemm, and A. Palevski, “Polar Kerr effect as probe for time-reversal symmetry breaking in unconventional superconductors,” [New J. Phys.](#) **11**, 055060 (2009) (cited on p. [138](#)).

- [177] K. Machida and T. Ohmi, “Phenomenological theory of ferromagnetic superconductivity,” *Phys. Rev. Lett.* **86**, 850 (2001) (cited on p. 139).
- [178] M. Thiemann, M. Dressel, and M. Scheffler, “Complete electrodynamics of a BCS superconductor with  $\mu\text{eV}$  energy scales: Microwave spectroscopy on titanium at mK temperatures,” *Phys. Rev. B* **97**, 214516 (2018) (cited on pp. 145–147).
- [179] O. Klein, E. J. Nicol, K. Holczer, and G. Grüner, “Conductivity coherence factors in the conventional superconductors Nb and Pb,” *Phys. Rev. B* **50**, 6307 (1994) (cited on p. 146).
- [180] P. J. Hirschfeld, W. O. Putikka, and D. J. Scalapino, “Microwave conductivity of  $d$ -wave superconductors,” *Phys. Rev. Lett.* **71**, 3705 (1993) (cited on p. 146).
- [181] K. Zhang, D. A. Bonn, S. Kamal, R. Liang, D. J. Baar, W. N. Hardy, D. Basov, and T. Timusk, “Measurement of the  $ab$  Plane Anisotropy of Microwave Surface Impedance of Untwinned  $\text{YBa}_2\text{Cu}_3\text{O}_{6.95}$  Single Crystals,” *Phys. Rev. Lett.* **73**, 2484 (1994) (cited on p. 146).
- [182] N. T. Huy, “Ferromagnetism, Superconductivity and Quantum Criticality in Uranium Intermetallics,” PhD dissertation (2008) (cited on p. 148).
- [183] D. Aoki, A. Huxley, E. Ressouche, D. Braithwaite, J. Flouquet, J.-P. Brison, E. Lhotel, and C. Paulsen, “Coexistence of superconductivity and ferromagnetism in URhGe,” *Nature* **413**, 613 (2001) (cited on p. 148).
- [184] S. Sundar, S. Gheidi, K. Akintola, A. M. Côté, S. R. Dunsiger, S. Ran, N. P. Butch, S. R. Saha, J. Paglione, and J. E. Sonier, “Coexistence of ferromagnetic

- fluctuations and superconductivity in the actinide superconductor  $\text{UTe}_2$ ,” [Phys. Rev. B \*\*100\*\*, 140502 \(2019\)](#) (cited on p. 148).
- [185] P. J. Hirschfeld and N. Goldenfeld, “Effect of strong scattering on the low-temperature penetration depth of a d-wave superconductor,” [Phys. Rev. B \*\*48\*\*, 4219 \(1993\)](#) (cited on p. 149).
- [186] E. E. M. Chia, D. J. Van Harlingen, M. B. Salamon, B. D. Yanoff, I. Bonalde, and J. L. Sarrao, “Nonlocality and strong coupling in the heavy fermion superconductor  $\text{CeCoIn}_5$  : A penetration depth study,” [Phys. Rev. B \*\*67\*\*, 014527 \(2003\)](#) (cited on p. 149).
- [187] P. J. Hirschfeld, P. Wölfle, J. A. Sauls, D. Einzel, and W. O. Putikka, “Electromagnetic absorption in anisotropic superconductors,” [Phys. Rev. B \*\*40\*\*, 6695 \(1989\)](#) (cited on p. 153).
- [188] H. Kim, K. Wang, Y. Nakajima, R. Hu, S. Ziemak, P. Syers, L. Wang, H. Hodovanets, J. D. Denlinger, P. M. R. Brydon, D. F. Agterberg, M. A. Tanatar, R. Prozorov, and J. Paglione, “Beyond triplet: Unconventional superconductivity in a spin-3/2 topological semimetal,” [Sci. Adv. \*\*4\*\* \(2018\)](#) (cited on p. 160).
- [189] J. A. Mydosh, P. M. Oppeneer, and P. S. Riseborough, “Hidden order and beyond: an experimental—theoretical overview of the multifaceted behavior of  $\text{URu}_2\text{Si}_2$ ,” [J. Phys. Condens. Matter \*\*32\*\*, 143002 \(2020\)](#) (cited on p. 160).
- [190] S. Ran, H. Kim, I.-L. Liu, S. R. Saha, I. Hayes, T. Metz, Y. S. Eo, J. Paglione, and N. P. Butch, “Enhancement and reentrance of spin triplet superconductivity in  $\text{UTe}_2$  under pressure,” [Phys. Rev. B \*\*101\*\*, 140503 \(2020\)](#) (cited on p. 160).

# Seokjin Bae

Maryland Quantum Materials Center, University of Maryland - College Park  
4150 Campus Drive, College Park, MD, 20742, USA  
sjbae@umd.edu, +1 (240) 547-7415

## EDUCATION

Ph. D., Physics

University of Maryland, College Park, MD, USA

August 2013 – August 2020

Thesis Advisor - Steven M. Anlage

B.S., Physics

Korea Advanced Institute of Science and Technology (KAIST), Daejeon, Republic of Korea

Feb 2013

## EXPERIENCE AND SKILLS

- **Low temperature cryogenics**

Lab manager of a dilution fridge system ( $\sim 10$  mK, dry system) / Designed and manufactured a cryogenic sample stage and 50 mT superconducting magnet

- **Microwave spectroscopy**

Surface impedance / Magnetic penetration depth / Time domain reflectometry measurement / Microwave resonator design and simulation (HFSS)

- **Laser scanning microscopy**

Built optical scanning microscope for microwave photo-response measurement

- **Lithography**

Designed photomasks and patterned micron width spirals on YBCO thin-films (wet/dry etch)

## PUBLICATIONS

- S. Bae, H. Kim, S. Ran, Y. S. Eo, I. Liu, W. T. Fuhrman, J. Paglione, N. P. Butch, S. M. Anlage, “**Anomalous normal fluid response in a chiral superconductor**”, arXiv:1909.09032 (2019)
- T. Metz, S. Bae, S. Ran, I. Liu, Y. S. Eo, W. T. Fuhrman, D. F. Agterberg, S. M. Anlage, N. P. Butch, and J. Paglione, “**Point Node Gap Structure of Spin-Triplet Superconductor  $UTe_2$** ”, *Phys. Rev. B* (R) 100, 220504 (2019)
- S. Bae, S. Lee, X. Zhang, I. Takeuchi, and S. M. Anlage, “**Microwave Meissner Screening of Proximity coupled Topological Insulator / Superconductor Bilayers**”, *Phys. Rev. Materials* 3, 124803 (2019)
- S. Bae, Y. Tan, A. P. Zhuravel, L. Zhang, S. Zeng, Y. Liu, T. A. Lograsso, R. Prozorov, Ariando, T. Venkatesan, and S. M. Anlage, “**Dielectric Resonator Method For Determining Gap Symmetry Of Superconductors Through Anisotropic Nonlinear Meissner Effect**”, *Rev. Sci. Instrum.* 90, 043901 (2019)
- A. P. Zhuravel, S. Bae, A. V. Lukashenko, A. N. Averkin, A. V. Ustinov, and S. M. Anlage, “**Imaging collective behavior in an rf-SQUID metamaterial tuned by DC and RF magnetic field**”, *Appl. Phys. Lett.* 114, 082601 (2019)
- A. P. Zhuravel, S. Bae, S. N. Shevchenko, A. N. Omelyanchouk, A. V. Lukashenko, A. V. Ustinov, and S. M. Anlage, “**Imaging the paramagnetic nonlinear Meissner effect in nodal gap superconductors**”, *Phys. Rev. B* 97, 054504 (2018)